

TiO₂-Based Nanomaterials for Advanced Environmental and Energy-Related Applications

Guest Editors: Xujie Lü, Baoyu Xia, Cunming Liu, Yefeng Yang,
and Hao Tang





TiO₂-Based Nanomaterials for Advanced Environmental and Energy-Related Applications

TiO₂-Based Nanomaterials for Advanced Environmental and Energy-Related Applications

Guest Editors: Xujie Lü, Baoyu Xia, Cunming Liu,
Yefeng Yang, and Hao Tang



Copyright © 2016 Hindawi Publishing Corporation. All rights reserved.

This is a special issue published in "Journal of Nanomaterials." All articles are open access articles distributed under the Creative Commons Attribution License, which permits unrestricted use, distribution, and reproduction in any medium, provided the original work is properly cited.

Editorial Board

Domenico Acierno, Italy
Katerina Aifantis, USA
Nageh K. Allam, USA
Margarida Amaral, Portugal
Martin Andersson, Sweden
Raul Arenal, Spain
Ilaria Armentano, Italy
Vincenzo Baglio, Italy
Lavinia Balan, France
Thierry Baron, France
Andrew R. Barron, USA
Reza Bayati, USA
Hongbin Bei, USA
Daniel Bellet, France
Stefano Bellucci, Italy
Enrico Bergamaschi, Italy
Samuel Bernard, France
Debes Bhattacharyya, New Zealand
Sergio Bietti, Italy
Giovanni Bongiovanni, Italy
Theodorian Borca-Tasciuc, USA
Mohamed Bououdina, Bahrain
Torsten Brezesinski, Germany
C. Jeffrey Brinker, USA
Christian Brosseau, France
Philippe Caroff, Australia
Victor M. Castaño, Mexico
Albano Cavaleiro, Portugal
Bhanu P. S. Chauhan, USA
Shafiul Chowdhury, USA
Jin-Ho Choy, Republic of Korea
Kwang-Leong Choy, UK
Yu-Lun Chueh, Taiwan
Elisabetta Comini, Italy
Giuseppe Compagnini, Italy
David Cornu, France
Miguel A. Correa-Duarte, Spain
P. Davide Cozzoli, Italy
Shadi A. Dayeh, USA
Luca Deseri, USA
Yong Ding, USA
Philippe Dubois, Belgium
Zehra Durmus, Turkey
Joydeep Dutta, Oman
Ali Eftekhari, USA
Jeffrey Elam, USA
Samy El-Shall, USA
Ovidiu Ersen, France
Claude Estournès, France
Andrea Falqui, KSA
Matteo Ferroni, Italy
Elena J. Foster, USA
Ilaria Fratoddi, Italy
Alan Fuchs, USA
Miguel A. Garcia, Spain
Siddhartha Ghosh, Singapore
P. K. Giri, India
Russell E. Gorga, USA
Jihua Gou, USA
Jean M. Greneche, France
Smrati Gupta, Germany
Kimberly Hamad-Schifferli, USA
Simo-Pekka Hannula, Finland
Michael Harris, USA
Yasuhiko Hayashi, Japan
F. Hernandez-Ramirez, Spain
Michael Z. Hu, USA
Nay Ming Huang, Malaysia
Shaoming Huang, China
David Hui, USA
Zafar Iqbal, USA
Balachandran Jeyadevan, Japan
Xin Jiang, Germany
Rakesh Joshi, Australia
Jeong-won Kang, Republic of Korea
Hassan Karimi-Maleh, Iran
Antonios Kelarakis, UK
Alireza Khataee, Iran
Ali Khorsand Zak, Iran
Philippe Knauth, France
Ralph Krupke, Germany
Christian Kübel, Germany
Prashant Kumar, UK
Michele Laus, Italy
Eric Le Bourhis, France
Jun Li, Singapore
Meiyong Liao, Japan
Shijun Liao, China
Silvia Licoccia, Italy
Wei Lin, USA
Nathan C. Lindquist, USA
Zainovia Lockman, Malaysia
Nico Lovergine, Italy
Jim Low, Australia
Jue Lu, USA
Ed Ma, USA
Laura M. Maestro, Spain
Gaurav Mago, USA
Muhamamd A. Malik, UK
Devanesan Mangalaraj, India
Sanjay R. Mathur, Germany
Tony McNally, UK
Yogendra Mishra, Germany
Paulo Cesar Morais, Brazil
Paul Munroe, Australia
Jae-Min Myoung, Republic of Korea
Rajesh R. Naik, USA
Albert Nasibulin, Russia
Toshiaki Natsuki, Japan
Koichi Niihara, Japan
Natalia Noginova, USA
Sherine Obare, USA
Won-Chun Oh, Republic of Korea
Atsuto Okamoto, Japan
Abdelwahab Omri, Canada
Ungyu Paik, Republic of Korea
Piersandro Pallavicini, Italy
Edward A. Payzant, USA
Alessandro Pegoretti, Italy
Ton Peijs, UK
Oscar Perales-Pérez, Puerto Rico
Jorge Pérez-Juste, Spain
Alexey P. Popov, Finland
Philip D. Rack, USA
Peter Reiss, France
Orlando Rojas, USA
Marco Rossi, Italy
Ilker S. Bayer, Italy
Cengiz S. Ozkan, USA
Sudipta Seal, USA
Shu Seki, Japan
Vladimir Šepelák, Germany
Huaiyu Shao, Japan
Prashant Sharma, USA
Donglu Shi, USA



Bhanu P. Singh, India
Surinder Singh, USA
Vladimir Sivakov, Germany
Ashok Sood, USA
Adolfo Speghini, Italy
Marinella Striccoli, Italy
Xuping Sun, KSA
Ashok K. Sundramoorthy, USA
Angelo Taglietti, Italy
Bo Tan, Canada
Leander Tapfer, Italy
Valeri P. Tolstoy, Russia

Muhammet S. Toprak, Sweden
R. Torrecillas, Spain
Achim Trampert, Germany
Takuya Tsuzuki, Australia
Tamer Uyar, Turkey
Bala Vaidhyanathan, UK
Luca Valentini, Italy
Rajender S. Varma, USA
Ester Vazquez, Spain
Antonio Villaverde, Spain
Ajayan Vinu, Australia
Ruibing Wang, Macau

Shiren Wang, USA
Yong Wang, USA
Magnus Willander, Sweden
Ping Xiao, UK
Zhi Li Xiao, USA
Yangchuan Xing, USA
Doron Yadlovker, Israel
Yoke K. Yap, USA
Kui Yu, Canada
William Yu, USA
Michele Zappalorto, Italy
Renyun Zhang, Sweden

Contents

TiO₂-Based Nanomaterials for Advanced Environmental and Energy-Related Applications

Xujie Lü, Baoyu Xia, Cunming Liu, Yefeng Yang, and Hao Tang

Volume 2016, Article ID 8735620, 3 pages

Preparation of TiO₂/Activated Carbon Composites for Photocatalytic Degradation of RhB under UV Light Irradiation

Baolin Xing, Changliang Shi, Chuanxiang Zhang, Guiyun Yi, Lunjian Chen, Hui Guo, Guangxu Huang, and Jianliang Cao

Volume 2016, Article ID 8393648, 10 pages

Recent Progress of TiO₂-Based Anodes for Li Ion Batteries

Yu Liu and Yefeng Yang

Volume 2016, Article ID 8123652, 15 pages

Modified Sol-Gel Synthesis of Carbon Nanotubes Supported Titania Composites with Enhanced Visible Light Induced Photocatalytic Activity

Quanjie Wang, Yanqing Wang, Baorong Duan, and Mengmeng Zhang

Volume 2016, Article ID 3967156, 6 pages

Enhanced Adsorption and Removal of Ciprofloxacin on Regenerable Long TiO₂ Nanotube/Graphene Oxide Hydrogel Adsorbents

Yuan Zhuang, Fei Yu, and Jie Ma

Volume 2015, Article ID 675862, 8 pages

Preparation of Stellerite Loading Titanium Dioxide Photocatalyst and Its Catalytic Performance on Methyl Orange

Hua Chen, Jianhua Wang, Huajun Wang, Fei Yang, Jia-nan Zhou, Jiajun Fu, Jie Yang, Zheng Yuan, and Bingbing Zheng

Volume 2015, Article ID 701589, 6 pages

New Insights into Benzene Hydrocarbon Decomposition from Fuel Exhaust Using Self-Support Ray Polarization Plasma with Nano-TiO₂

Tao Zhu, Wenjuan Zhao, Wenjing Zhang, Ni Xia, and Xiaoyang Li

Volume 2015, Article ID 527194, 8 pages

Experimental Study on the Deactivating Effect of KNO₃, KCl, and K₂SO₄ on Nanosized Ceria/Titania SCR Catalyst

Xiongbo Chen, Ping Fang, Wenhao Zeng, Kunyuan Liu, Zhixiong Tang, and Chaoping Cen

Volume 2015, Article ID 513814, 10 pages

Influence of Anodic Oxidation Parameters of TiO₂ Nanotube Arrays on Morphology and Photocatalytic Performance

Xiaoyu Zhao, Yuxiang Zhu, Yanfei Wang, Liang Zhu, Libin Yang, and Zuoliang Sha

Volume 2015, Article ID 104193, 10 pages

Editorial

TiO₂-Based Nanomaterials for Advanced Environmental and Energy-Related Applications

Xujie Lü,¹ Baoyu Xia,² Cunming Liu,³ Yefeng Yang,⁴ and Hao Tang⁵

¹Center for Integrated Nanotechnologies, Los Alamos National Laboratory, Los Alamos, NM 87545, USA

²School of Chemical and Biomedical Engineering, Nanyang Technological University, Singapore 637459

³Department of Physics, University of South Florida, 4202 East Fowler Avenue, Tampa, FL 33620, USA

⁴Department of Materials Engineering, College of Materials and Textile, Zhejiang Sci-Tech University, Hangzhou 310018, China

⁵Chemistry Department, Rutgers University, 73 Warren Street, Newark, NJ 07102, USA

Correspondence should be addressed to Xujie Lü; xujie@lanl.gov

Received 15 February 2016; Accepted 17 February 2016

Copyright © 2016 Xujie Lü et al. This is an open access article distributed under the Creative Commons Attribution License, which permits unrestricted use, distribution, and reproduction in any medium, provided the original work is properly cited.

Titanium dioxide (TiO₂) is one of the most attractive transition-metal oxides because of its superior physical and chemical properties, which has been widely applied in environmental clean-up (photocatalytic pollution removal), energy conversion (hydrogen production and solar cells), energy storage (lithium batteries and supercapacitors), security (sensors), panel display (transparent conducting films), biomedical devices, and so forth [1–18]. The performance of TiO₂ in these applications highly depends on its structural, electronic, optical, and morphological as well as the surface properties (exposed facets). Great effort has been devoted to adjust these properties and apparent progress has been made on the synthesis of the 0-, 1-, 2-, and 3-dimensional nanostructured TiO₂ materials. Nevertheless, further investigations are required on the development of new synthetic methods and the understanding of its relationship between the intrinsic properties and performance, to facilitate the commercialization of TiO₂-based materials in advanced environmental and energy-related areas.

This issue includes original research articles and a review that cover the synthesis of TiO₂-based nanomaterials and their environmental and energy-related applications. We summarize the published articles as below.

In “Influence of Anodic Oxidation Parameters of TiO₂ Nanotube Arrays on Morphology and Photocatalytic Performance,” X. Zhao et al. present the influence of electrolyte, applied potential, and duration of oxidation process on

nanomorphology and photocatalytic property of titanium dioxide nanotube arrays (TNTAs). Compared to the glycol electrolyte, the TNTAs grown by using the DMSO electrolyte exhibit much better photocatalytic activity, but their nanomorphology is much worse. Longer time and higher oxidation voltage benefit the growth of TNTAs.

TiO₂-based catalysts for the selective catalytic reduction of NO are hotspots in environmental catalysis. X. Chen et al. in their paper entitled “Experimental Study on the Deactivating Effect of KNO₃, KCl, and K₂SO₄ on Nanosized Ceria/Titania SCR Catalyst” investigated the deactivating effect of potassium compounds on nanosized CeO₂/TiO₂ selective catalytic reduction catalyst. This study would provide useful insights for the application and life management of CeO₂/TiO₂ in potassium-rich environments such as biofuel-fired boilers.

Development of supported titanium dioxide- (TiO₂-) based nanomaterials would promote their performance. In “Preparation of Stellerite Loading Titanium Dioxide Photocatalyst and Its Catalytic Performance on Methyl Orange,” H. Chen et al. reported the photocatalytic decomposition of methyl orange (MO) over a stellerite modified-TiO₂ photocatalyst. This work would provide a promising strategy to explore highly efficient photocatalyst and thus promote their further application in environmental fields.

Volatile organic compounds have been identified as indoor and outdoor pollutants and the treatment of them

has been studied for decades. In “New Insights into Benzene Hydrocarbon Decomposition from Fuel Exhaust Using Self-support Ray Polarization Plasma with Nano-TiO₂,” T. Zhu et al. developed a new strategy of using nano-TiO₂ as the catalyst in the self-support ray polarization of nonthermal plasma. This strategy showed improved performance to remove benzene. Indeed, at electric field strength of 12 kV/cm, 99% of benzene was removed. Moreover, the final products are environmentally friendly with decreased residence of ozone. This study with advances in potential industrial application should be of interest to the community.

Carbon materials have been extensively investigated and have been well incorporated with TiO₂ materials to improve the performance of their composites. In “Modified Sol-Gel Synthesis of Carbon Nanotubes Supported Titania Composites with Enhanced Visible Light Induced Photocatalytic Activity,” Q. Wang et al. report a multiwalled carbon nanotube enhanced TiO₂ nanocomposites for photocatalytic degradations. The nanocomposites possess good absorption properties not only in the ultraviolet but also in the visible light region. Under irradiation of ultraviolet lamp, the prepared composites have the highest photodegradation efficiency of 83% within 4 hours towards the degradation of methyl orange (MO) aqueous solution. The results indicate that the carbon nanotubes supported TiO₂ nanomaterials exhibit high photocatalytic activity and stability, showing great potentials in the treatment of wastewater.

In a paper entitled “Enhanced Adsorption and Removal of Ciprofloxacin on Regenerable Long TiO₂ Nanotube/Graphene Hydrogel Adsorbents,” J. Ma et al. reported the investigation of regenerable long TiO₂ nanotube/graphene oxide hydrogel adsorbent for antibiotic pollutants, which would attract the attention of environmental science, materials, and nanotechnology community to development a safe and sustainable society.

In “Preparation of TiO₂/Activated Carbon Composites for Photocatalytic Degradation of RhB under UV Light Irradiation,” J. Cao et al. used a sol-gel method to prepare TiO₂/activated carbon (AC) composites and they have found that the loading cycles of TiO₂ precursor play an important role in controlling the morphological structure and photocatalytic activity of TiO₂/AC composites. The porosity parameters of these composite photocatalysts such as specific surface area and total pore volume decrease whereas the loading amount of TiO₂ increases. The TiO₂/AC composite synthesized at two loading cycles exhibits the highest photocatalytic activity.

TiO₂ is a kind of promising anode material because of its low cost, excellent structural stability, small volume expansion, and good safety performance due to its high discharge plateau potential (about 1.5–1.8 V versus lithium) that would not decompose the organic electrolyte, large exposed surface offering more lithium-insertion channels. However, the poor electronic conductivity and low lithium ion diffusivity of TiO₂ result in poor cycling stability and lithium ion depletion at high current rates. A review entitled “Recent Progress of TiO₂-Based Anodes for Li Ion Batteries” by Y. Liu and Y. Yang is specifically focused on the recent progress in enhancing the lithium ion batteries (LIBs) performance of TiO₂ with

various synthetic strategies and architectures control, such as designing hollow structure to form more open channels and active sites for Li ion transport, coating or combining TiO₂ with metal to improve its electronic conductivity, or incorporating carbonaceous materials such as active carbon, CNTs, and graphene to enhance its capacity and cycling stability.

The guest editors hope that this special issue will inspire further research in the field of TiO₂ nanomaterials and their applications in advanced environmental and energy-related areas.

Acknowledgments

The editors gratefully thank the authors for their contributions to this special issue and the reviewers for their constructive comments.

Xujie Lü
Baoyu Xia
Cunming Liu
Yefeng Yang
Hao Tang

References

- [1] B. O'Regan and M. Graetzel, “Low-cost, high-efficiency solar cell based on dye-sensitized colloidal TiO₂ films,” *Nature*, vol. 353, no. 6346, pp. 737–740, 1991.
- [2] R. Asahi, T. Morikawa, T. Ohwaki, K. Aoki, and Y. Taga, “Visible-light photocatalysis in nitrogen-doped titanium oxides,” *Science*, vol. 293, no. 5528, pp. 269–271, 2001.
- [3] J. Wang, D. N. Tafen, J. P. Lewis et al., “Origin of photocatalytic activity of nitrogen-doped TiO₂ nanobelts,” *Journal of the American Chemical Society*, vol. 131, no. 34, pp. 12290–12297, 2009.
- [4] J. Zhang, Q. Xu, Z. Feng, M. Li, and C. Li, “Importance of the relationship between surface phases and photocatalytic activity of TiO₂,” *Angewandte Chemie*, vol. 120, no. 31, pp. 1790–1793, 2008.
- [5] X. Lü, X. Mou, J. Wu et al., “Improved-performance dye-sensitized solar cells using Nb-Doped TiO₂ electrodes: efficient electron injection and transfer,” *Advanced Functional Materials*, vol. 20, no. 3, pp. 509–515, 2010.
- [6] M. Sathish, B. Viswanathan, R. P. Viswanath, and C. S. Gopinath, “Synthesis, characterization, electronic structure, and photocatalytic activity of nitrogen-doped TiO₂ nanocatalyst,” *Chemistry of Materials*, vol. 17, no. 25, pp. 6349–6353, 2005.
- [7] B. Naik, S. M. Kim, C. H. Jung, S. Y. Moon, S. H. Kim, and J. Y. Park, “Enhanced H₂ generation of Au-loaded, nitrogen-doped TiO₂ hierarchical nanostructures under visible light,” *Advanced Materials Interfaces*, vol. 1, no. 1, Article ID 1300018, 2014.
- [8] X. Lü, F. Huang, X. Mou, Y. Wang, and F. Xu, “A general preparation strategy for hybrid TiO₂ hierarchical spheres and their enhanced solar energy utilization efficiency,” *Advanced Materials*, vol. 22, no. 33, pp. 3719–3722, 2010.
- [9] H. Ren, R. Yu, J. Wang et al., “Multishelled TiO₂ hollow microspheres as anodes with superior reversible capacity for lithium ion batteries,” *Nano Letters*, vol. 14, no. 11, pp. 6679–6684, 2014.

- [10] W. Li, F. Wang, Y. Liu et al., "General strategy to synthesize uniform mesoporous TiO₂/graphene/mesoporous TiO₂ sandwich-like nanosheets for highly reversible lithium storage," *Nano Letters*, vol. 15, no. 3, pp. 2186–2193, 2015.
- [11] X. Lü, J. Li, X. Mou et al., "Room-temperature ferromagnetism in Ti_{1-x}V_xO₂ nanocrystals synthesized from an organic-free and water-soluble precursor," *Journal of Alloys and Compounds*, vol. 499, no. 2, pp. 160–165, 2010.
- [12] C. Sotelo-Vazquez, N. Noor, A. Kafizas et al., "Multifunctional P-doped TiO₂ films: a new approach to self-cleaning, transparent conducting oxide materials," *Chemistry of Materials*, vol. 27, no. 9, pp. 3234–3242, 2015.
- [13] X. Lü, S. Ding, Y. Xie, and F. Huang, "Non-aqueous preparation of high-crystallinity hierarchical TiO₂ hollow spheres with excellent photocatalytic efficiency," *European Journal of Inorganic Chemistry*, vol. 2011, no. 18, pp. 2879–2883, 2011.
- [14] B. Liu, H. M. Chen, C. Liu, S. C. Andrews, C. Hahn, and P. Yang, "Large-scale synthesis of transition-metal-doped TiO₂ nanowires with controllable overpotential," *Journal of the American Chemical Society*, vol. 135, no. 27, pp. 9995–9998, 2013.
- [15] X. Lü, F. Huang, J. Wu, S. Ding, and F. Xu, "Intelligent hydrated-sulfate template assisted preparation of nanoporous TiO₂ spheres and their visible-light application," *ACS Applied Materials & Interfaces*, vol. 3, no. 2, pp. 566–572, 2011.
- [16] T. Leijtens, G. E. Eperon, S. Pathak, A. Abate, M. M. Lee, and H. J. Snaith, "Overcoming ultraviolet light instability of sensitized TiO₂ with meso-superstructured organometal trihalide perovskite solar cells," *Nature Communication*, vol. 4, article 2885, 2013.
- [17] X. Lü, W. Yang, Z. Quan et al., "Enhanced electron transport in Nb-doped TiO₂ nanoparticles via pressure-induced phase transitions," *Journal of the American Chemical Society*, vol. 136, no. 1, pp. 419–426, 2014.
- [18] J. T.-W. Wang, J. M. Ball, E. M. Barea et al., "Low-temperature processed electron collection layers of graphene/TiO₂ nanocomposites in thin film perovskite solar cells," *Nano Letters*, vol. 14, no. 2, pp. 724–730, 2014.

Research Article

Preparation of TiO₂/Activated Carbon Composites for Photocatalytic Degradation of RhB under UV Light Irradiation

Baolin Xing,^{1,2} Changliang Shi,¹ Chuanxiang Zhang,¹ Guiyun Yi,^{1,2} Lunjian Chen,¹ Hui Guo,¹ Guangxu Huang,¹ and Jianliang Cao¹

¹School of Materials Science and Engineering, Henan Polytechnic University, Jiaozuo 454003, China

²Department of Chemical Engineering, University of Newcastle, Callaghan, NSW 2308, Australia

Correspondence should be addressed to Guiyun Yi; guiyunyi@163.com and Jianliang Cao; caojianliang@hpu.edu.cn

Received 30 October 2015; Revised 23 December 2015; Accepted 26 January 2016

Academic Editor: Cunming Liu

Copyright © 2016 Baolin Xing et al. This is an open access article distributed under the Creative Commons Attribution License, which permits unrestricted use, distribution, and reproduction in any medium, provided the original work is properly cited.

Photocatalysts comprising nanosized TiO₂ particles on activated carbon (AC) were prepared by a sol-gel method. The TiO₂/AC composites were characterized by X-ray diffraction (XRD), thermogravimetric (TG) analysis, nitrogen adsorption, scanning electron microscope (SEM), transmission electron microscope (TEM), and energy dispersive X-ray (EDX). Their photocatalytic activities were studied through the degradation of Rhodamine B (RhB) in photocatalytic reactor at room temperature under ultraviolet (UV) light irradiation and the effect of loading cycles of TiO₂ on the structural properties and photocatalytic activity of TiO₂/AC composites was also investigated. The results indicate that the anatase TiO₂ particles with a crystal size of 10–20 nm can be deposited homogeneously on the AC surface under calcination at 500°C. The loading cycle plays an important role in controlling the loading amount of TiO₂ and morphological structure and photocatalytic activity of TiO₂/AC composites. The porosity parameters of these composite photocatalysts such as specific surface area and total pore volume decrease whereas the loading amount of TiO₂ increases. The TiO₂/AC composite synthesized at 2 loading cycles exhibits a high photocatalytic activity in terms of the loading amount of TiO₂ and as high as 93.2% removal rate for RhB from the 400 mL solution at initial concentration of 2×10^{-5} mol/L under UV light irradiation.

1. Introduction

Dyes, generated by various manufacture industries such as dyestuffs, textile, paper, food, cosmetics, leather, and plastics, are the most common contaminants in wastewater [1–3]. These dyes appearing in wastewater, even at very low concentrations, are highly noticeable and can potentially hurt human health. However, presently, there is still no unique treatment that is capable of effectively eliminating all types of dyes in wastewater because of their complex structure and stable chemical property and diversity [4, 5]. Therefore, it is highly important to find out an effective method for treating industrial effluent such as dyes.

Currently, a number of techniques and processes including physical, chemical, and biological methods have been studied to treat the dyes from wastewater [6–10]. For instance, adsorption and photocatalysis have been considered as effective approaches for dye removal. The adsorption is

a nondestructive process, by which the contaminants can be transferred from wastewater to adsorbent such as activated carbon (AC). However, the adsorption efficiency of the adsorbents after regeneration is greatly reduced [11, 12]. In comparison, the photocatalysis is a promising advanced oxidation process, which usually uses heterogeneous titanium dioxide (TiO₂) as a photocatalyst to degrade the contaminants by the decomposition and oxidation processes on its surface [13–15]. However, there are some disadvantages of TiO₂ used in advanced oxidation process as TiO₂ powder is easy to agglomerate, with poor adsorption capacity, and is difficult to be separated and recycled from the solution [5, 16, 17]. For the purpose of overcoming the drawbacks of these two approaches, the combination of adsorption and photocatalytic processes was previously proved to be a very promising technology for the treatment of wastewater. For instance, some different types of composites including ordered mesoporous TiO₂/silica nanocomposites [18], TiO₂/

alumina composites [19], TiO₂/diatomite composites [20], TiO₂/zeolite nanocomposites [21], TiO₂/clay composites [22], TiO₂/bentonite composites [23], TiO₂/reduced graphene oxide nanocomposites (TiO₂/RGO) [24], TiO₂/activated carbon fiber (TiO₂/ACF) [25], TiO₂/carbon nanotube (TiO₂/CNT) [26], TiO₂/graphene (TiO₂/GR) [27], and TiO₂/activated carbon (TiO₂/AC) [5] have been extensively studied. As AC possesses a large specific surface area, high adsorption capacity, and suitable pore structure [8, 13, 28], TiO₂/AC composites are receiving considerable attention for the degradation of dye-containing wastewater. Wang et al. [29] successfully prepared TiO₂/AC composites by dip-hydrothermal method using peroxotitanate as the TiO₂ precursor for degradation of methyl orange. Slimen et al. [28] investigated the TiO₂/AC composites which were directly obtained by sol-gel method for the degradation of methylene blue in an aqueous solution. Jamil et al. [30] synthesized photocatalyst by AC impregnated with TiO₂ for the removal of methyl orange from water, and the synergistic effects of adsorption and photocatalytic activity in TiO₂/AC for the degradation of the methyl orange have been found. Eliyas et al. [17] prepared a TiO₂/AC composite by an original method combining impregnation and physicochemical pyrolysis, and the photocatalytic decomposition of an azo dye pollutant under visible light illumination and ultraviolet (UV) light irradiation was studied. Zhang et al. and He et al. [6, 31] investigated the degradation of methyl orange and Rhodamine B (RhB) by microwave-induced photocatalytic technology using TiO₂/AC composites.

Among the reported processes for the treatment of the dye-containing wastewater, it has been shown that all kinds of TiO₂/AC composites are able to exhibit enhanced photocatalytic performance and increased removal efficiency compared to pure TiO₂. However, one of critical problems still hindering further large scale application of the TiO₂/AC composites in wastewater treatment is the lack of reproducibility due to the variation in the preparation and treatment processes [32]. Hence, it is necessary to develop a simple and low-cost method to prepare TiO₂/AC composites. Due to the simple synthesis routes and properly controlled morphology of TiO₂ on AC, the sol-gel technique is the most commonly used chemical method for the preparation of TiO₂/AC [15]. However, to the best of our knowledge, many researches focused on the photocatalytic activity, degradation mechanism and kinetics, the synergistic effects, and the role of the chemical and textural properties of AC during photocatalytic degradation of organic contaminants in wastewater [13, 17, 33], but there is little information available concerning the effect of loading cycle on the structural properties and photocatalytic activity of the final TiO₂/AC composites.

In this work, the coal-based AC (prepared by KOH activation) was adopted as a support to synthesize the TiO₂/AC composites under different loading cycles by sol-gel method. The adsorption properties and photocatalytic activity were investigated in aqueous solution using Rhodamine B (RhB) dye as a model contaminant for the photodegradation experiments. Such molecule is usually present in the wastewater from several industries.

2. Experimental

2.1. Materials. Activated carbon (AC) was prepared from lignite by potassium hydroxide (KOH) activation as described in our previous work [34]. In this procedure, activation was performed at 800°C for 2 h at 2:1 weight ratio of KOH to lignite. The specific surface area and total pore volume of the as-obtained AC are 1576 m²/g and 0.967 cm³/g, while its ash content is only 0.3%. Tetrabutyl titanate (Ti(OC₄H₉)₄), ethanol, acetic acid, nitric acid, potassium hydroxide, and RhB were of analytical grade and used without further purification. All the reagents were supplied by Tianjin Kemiou Chemical Reagent Co., Ltd., China.

2.2. Preparation of TiO₂/AC Composites. TiO₂/AC composites were synthesized using Ti(OC₄H₉)₄ as a precursor by sol-gel route as follows: First, solution A was prepared by diluting 10 mL Ti(OC₄H₉)₄ with 34 mL anhydrous ethanol and 2.5 mL acetic acid. Second, solution B was prepared by mixing 17 mL anhydrous ethanol with 3 mL deionized water and the pH value of the solution was adjusted to 2-3 by slowly adding dilute nitric acid. Third, solution B was transferred into solution A drop by drop with vigorous stirring to produce the TiO₂ sol. The sol was mixed with the as-prepared AC under continuous magnetic stirring and the mixture was aged for 20 h in dark area at ambient temperature to form the sol-coated AC. The mixture was washed sequentially with ethanol and deionized water to remove untreated product and the solid was collected by centrifugation during each wash. The aging and washing procedures were repeated 3 times; each loading cycle of the final sol-coated AC was dried for 4 h at 110°C and then was calcined at 500°C for 3 h in a nitrogen atmosphere with a heating rate of 10°C/min. Simultaneously, the aged gel was also calcined at 500°C for 3 h to synthesize the pure nanosized TiO₂ for comparison. The TiO₂/AC composites were synthesized at 1, 2, and 3 loading cycles, which were named TiO₂/AC-1, TiO₂/AC-2, and TiO₂/AC-3, respectively.

2.3. Characterization of TiO₂/AC Composites. X-ray diffraction (XRD) experiments of the samples were performed on a Bruker-AXS D8 advance diffractometer with Cu K α radiation, and the crystal size was calculated by X-ray line broadening analysis using Scherrer formula [13, 28, 35]: $D = 0.89\lambda/\beta \cos\theta$, where D is the crystalline size in nm, λ (0.15418 nm) is the wavelength of X-ray radiation, and β is the line width at half maximum height for the anatase (101) peak ($2\theta = 25.3^\circ$) in radians. The morphology and elemental analysis of the TiO₂/AC composites were examined by a scanning electron microscope (JSM-6390LV, Japan), a transmission electron microscope (JEM-2100, Japan), and an energy dispersive X-ray spectroscopy detector (JSM-5200, Japan). The TiO₂/AC composites were analyzed by a thermogravimetric (TG) analyzer (STA409 PC, Germany) in a range of 20–800°C with a heating rate of 10°C/min in an air flow, and the TiO₂ loading amount was calculated by ash weight (minus the ash weight of AC). Brunauer-Emmett-Teller (BET) specific surface area

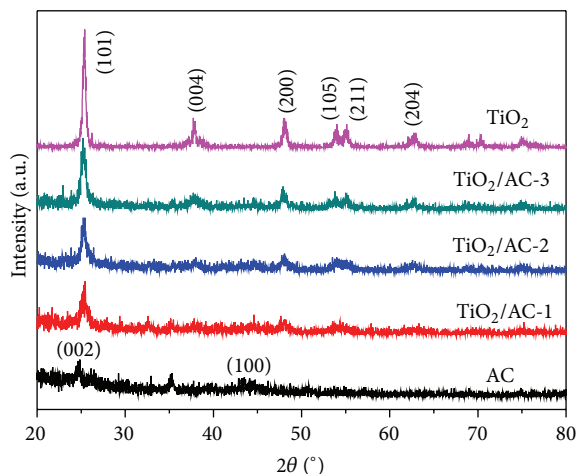


FIGURE 1: XRD patterns of AC and pure TiO_2 and TiO_2/AC composites.

of the AC and photocatalyst samples was measured from the nitrogen adsorption-desorption isotherms at 77 K on an automatic adsorption instrument (Quantachrome, Autosorb-iQ-MP, USA), and the pore size distribution was determined by a density functional theory (DFT) model. All samples were degassed under vacuum at 200 °C for 12 h prior to the nitrogen adsorption analysis.

2.4. Photocatalytic Degradation Experiments. The photocatalytic activity experiment of the TiO_2/AC composites was studied by the degradation of RhB under UV light irradiation in a photocatalytic reactor at room temperature. The light source was from 450 W high pressure mercury lamp (Foshan Electrical and Lighting Co., Ltd.). In each experiment, 0.02 g photocatalyst was added into 400 mL of 2×10^{-5} mol/L RhB solution under magnetic stirring and maintained in the dark for 90 min in order to allow for adsorption equilibrium, and then the suspension was irradiated under UV light. After that, about 10 mL of the suspension sample was collected at 10 min intervals during the irradiation period, which was centrifuged to remove the photocatalyst. The remaining RhB in the solution was measured at 554 nm using a spectrophotometer (TU-1810, Beijing Purkinje General Instrument Co., Ltd.). The absorbance measured was then converted to concentration, and the removal rate of RhB (R%) was calculated according to the following equation, $R\% = 100(C_0 - C)/C_0$, where C_0 and C are the concentrations of RhB before and after adsorption-degradation process, respectively. The total removal rate of RhB obtained by TiO_2/AC composites contributes to the adsorptive and photocatalytic processes.

3. Results and Discussion

3.1. Crystalline Phase Characterization. The XRD patterns of AC, pure TiO_2 , and TiO_2/AC composites are shown in Figure 1. As can be seen, the XRD of AC shows two weak broad peaks at about 24.6° and 43.9°, corresponding to reflection in the (002) plane and the (100) plane of aromatic layers

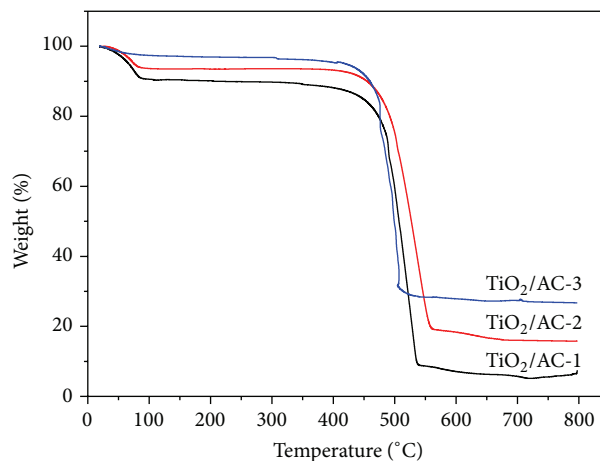


FIGURE 2: TG curves of TiO_2/AC composites.

in carbon [36], which indicates a predominantly amorphous structure present in the AC substrate, whereas the XRD pattern of pure TiO_2 shows six main diffraction peaks at about 25.3°, 37.8°, 48.0°, 53.8°, 55.1°, and 62.8°, which can be, respectively, indexed as (101), (004), (200), (105), (211), and (204) planes of an anatase TiO_2 [14, 32, 37]. It suggests that the anatase TiO_2 is predominantly formed in the pure nanosized TiO_2 when the gel was calcined at 500 °C. The result is in good agreement with Xue et al.'s research [13]. For the TiO_2/AC composites, it is obvious that the diffraction peak intensity improves with increasing the loading cycle. When the AC is loaded by TiO_2 1 time, the XRD pattern of $\text{TiO}_2/\text{AC-1}$ presents only one apparent diffraction peak at about 25.3°, whereas the six diffraction peaks mentioned above are observed obviously in the XRD pattern for $\text{TiO}_2/\text{AC-3}$ when the AC is loaded by TiO_2 3 times, which indicates that more TiO_2 can be loaded on the substrate AC surface with multiloading. The results demonstrate that the loading amount of TiO_2 in the composite photocatalyst is strongly affected by the loading cycle in the sol-gel process. A similar effect has also been reported by other authors [13]. Notably, in these TiO_2/AC composites, there is no obvious peak at the position of 24.6°, which is the characteristic peak for the (002) plane of AC. The reason could be attributed to the fact that the main peak of AC at 24.6° might be shielded by the peak of anatase TiO_2 at 25.3°. Additionally, the crystal size of TiO_2 in the composite photocatalysts is calculated using Scherrer's equation for the diffraction peak at 25.3° (101 plane) as 12–14 nm.

3.2. TG Analysis. In order to investigate the loading amount of TiO_2 in the TiO_2/AC composites synthesized at different loading cycles, thermogravimetric (TG) tests were carried out in a range of 20–800 °C with an air flow. As shown in the TG curves (Figure 2), the gentle weight loss of TiO_2/AC composite at temperatures ranging from 20 to 90 °C is generally attributed to the escape of adsorbed water while the obvious weight loss at temperatures from 450 to 550 °C is mainly due to the carbons burning off in air. The mass which almost

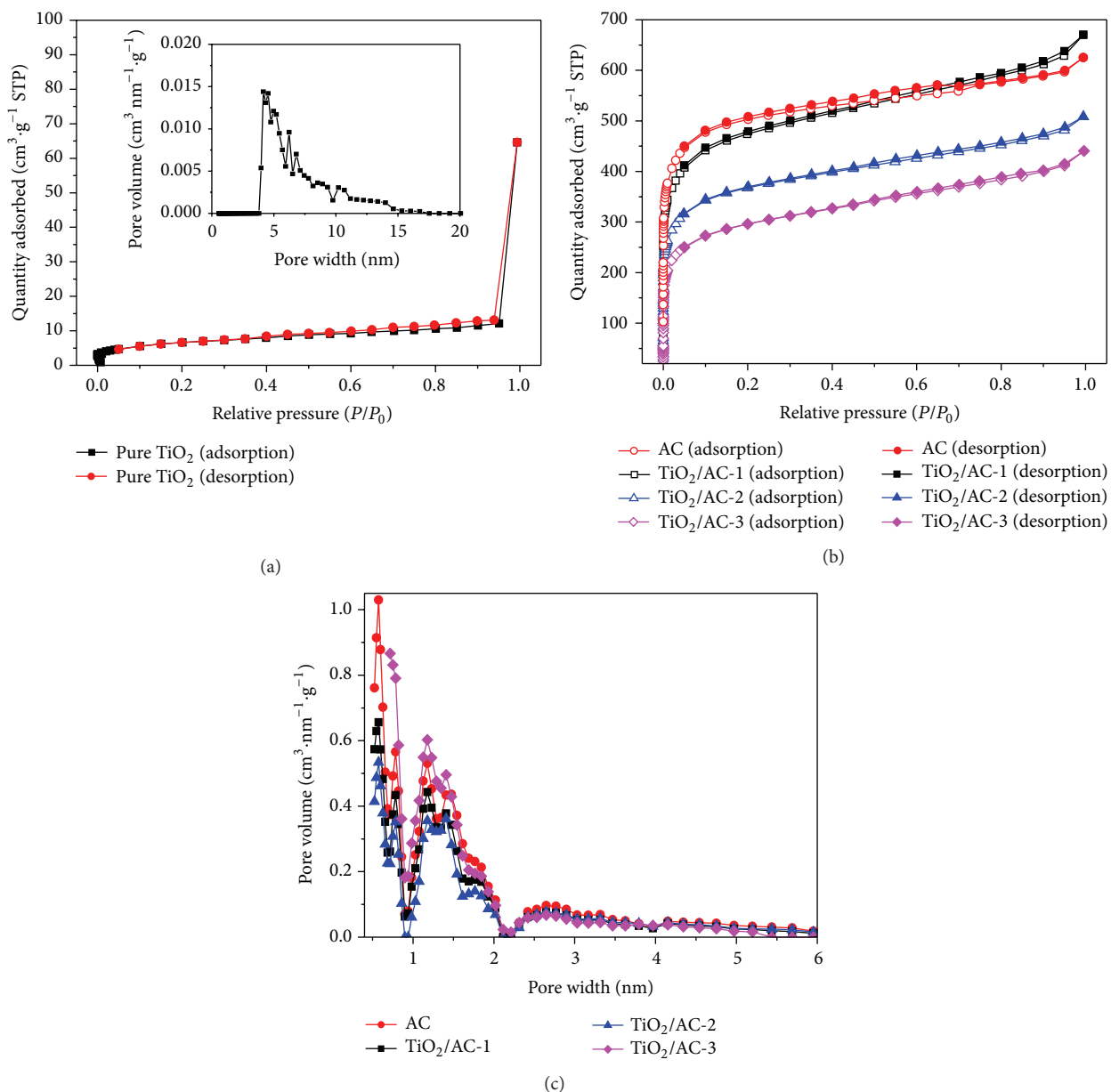


FIGURE 3: Nitrogen adsorption-desorption isotherms and pore size distributions of pure TiO_2 , AC, and TiO_2/AC composites: (a) nitrogen adsorption-desorption isotherm and pore size distribution (inset) of pure TiO_2 , (b) nitrogen adsorption-desorption isotherms of AC and TiO_2/AC composites, and (c) pore size distributions of AC and TiO_2/AC composites.

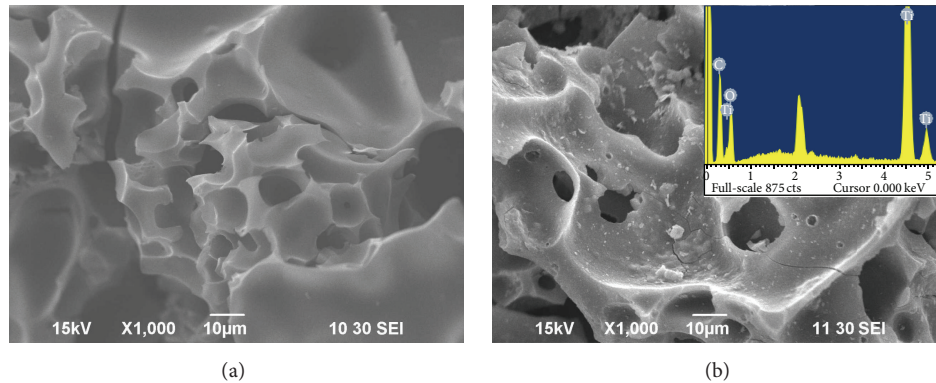
keeps constant in the TG curves after 600°C contains the loaded TiO_2 and ash in AC. According to the TG curves, the weight loss of the three composite photocatalysts decreases with the loading cycle increasing, and the final ash content is about 5.6% for $\text{TiO}_2/\text{AC-1}$, 15.8% for $\text{TiO}_2/\text{AC-2}$, and 26.9% for $\text{TiO}_2/\text{AC-3}$. Hence, the loading amount of TiO_2 in the composite photocatalysts synthesized at 1, 2, and 3 loading cycles subtracting the ash content of substrate AC (0.3%) is about 5.3%, 15.5%, and 26.7%, respectively. This result further indicates that the loading cycle has an important influence on the loading amount of TiO_2 in the composite photocatalysts, since more loading cycles lead to more TiO_2 being deposited on the substrate AC surface.

3.3. Pore Structure of TiO_2/AC Composites. The nitrogen adsorption-desorption isotherms and pore size distributions of pure TiO_2 , original AC, and the TiO_2/AC composites are presented in Figure 3. For pure TiO_2 , a typical type II isotherm (Figure 3(a)) with a small hysteresis phenomenon attributed to aggregation of nanoparticles can be noticed, and this isotherm corresponds to a relatively low porosity material in agreement with the low specific surface area ($10 \text{ m}^2/\text{g}$) and the negligible micropore volume listed in Table 1. However, the isotherms of AC and TiO_2/AC composites (Figure 3(b)) exhibit a marked increment at the relative pressure of P/P_0 less than 0.1, followed by approximate plateaus at the relative pressure of P/P_0 more than 0.2, indicating that the AC and

TABLE 1: The specific surface area and pore structure parameters of TiO₂, AC, and TiO₂/AC composites.

Sample	$S_{\text{BET}}/(\text{m}^2 \cdot \text{g}^{-1})$	$S_{\text{mic}}/(\text{m}^2 \cdot \text{g}^{-1})$	$S_{\text{mes}}/(\text{m}^2 \cdot \text{g}^{-1})$	$V_t/(\text{cm}^3 \cdot \text{g}^{-1})$	$V_{\text{mic}}/(\text{cm}^3 \cdot \text{g}^{-1})$	$V_{\text{mes}}/(\text{cm}^3 \cdot \text{g}^{-1})$
Pure TiO ₂	10	0	10	0.057	0	0.057
AC	1576	1298	278	0.967	0.662	0.305
TiO ₂ /AC-1	1507	1061	446	1.037	0.542	0.495
TiO ₂ /AC-2	1167	836	331	0.786	0.427	0.359
TiO ₂ /AC-3	949	616	333	0.682	0.315	0.367

S_{BET} , BET specific surface area; S_{mic} , micropore specific surface; S_{mes} , mesopore specific surface; V_t , total pore volume; V_{mic} , micropore volume; and V_{mes} , mesopore volume.

FIGURE 4: SEM images of AC and TiO₂/AC-2: (a) AC, (b) TiO₂/AC-2 (inset: EDX spectrum).

the TiO₂/AC composites are essentially microporous materials. Also, the desorption hysteresis loops at a relative pressure of around 0.5 are observed in the isotherms of AC and the TiO₂/AC composites, suggesting the presence of a certain amount of mesopores. From the curves of the DFT pore size distributions of AC and TiO₂/AC composites (Figure 3(c)), it can be seen that the pores of AC and TiO₂/AC composites are distributed in the range of 0.5–6 nm, and the mesopores are mainly distributed between 2.2 nm and 5.0 nm. Furthermore, compared to the original AC, the micropores of TiO₂/AC composites decrease gradually with the increasing of loading cycle, especially for the pore distributed in the range of 0.5–1 nm. The reason can be attributed to the fact that more loading cycles lead to more TiO₂ particles being deposited, blocking some micropores of the AC substrate. The specific surface area (S_{BET}), micropore specific surface (S_{mic}), mesopore specific surface (S_{mes}), total pore volume (V_t), micropore volume (V_{mic}), and mesopore specific surface (V_{mes}) of AC are 1576 m²/g, 1298 m²/g, 278 m²/g, 0.967 cm³/g, 0.662 cm³/g, and 0.305 cm³/g (Table 1), respectively. For the TiO₂/AC composites, S_{BET} , S_{mic} , V_t , and V_{mic} decrease gradually with increasing the loading cycles, except that the V_t of TiO₂/AC-1 increases slightly. The increment of V_t of TiO₂/AC-1 is mainly caused by the covering of TiO₂ on the AC surface and forms a small number of mesopores in the composite photocatalyst to increase the pore volume. In addition, it is worthy of noting that S_{mic} and V_{mic} of composite photocatalyst decrease from 1298 m²/g and 0.662 cm³/g to 616 m²/g and 0.315 cm³/g when the original AC was loaded by TiO₂ 3 times, whereas its S_{mes} and V_{mes} present a slight increment. The results further

confirm that some micropores are blocked or covered by the TiO₂ particles.

3.4. SEM and TEM Analysis. The morphologies of the original AC and the TiO₂/AC-2 composite photocatalyst were investigated by SEM micrographs. As shown in Figure 4, the original AC displays a uniform morphology with irregular and highly porous surface, indicating well-developed porosity (Figure 4(a)). The surface of the TiO₂/AC-2 is homogeneously covered with TiO₂ particles without apparent agglomeration in local area (Figure 4(b)). Also, the TiO₂ particles deposit not only on the surface but also on the mesopores and macropores of AC, which will increase the probability of receiving light and exhibiting higher photocatalytic activity [13]. In addition, the energy dispersive X-ray (EDX) spectrum of TiO₂/AC-2 (Figure 4(b), inset) shows that the presence of C, Ti, and O is the main element for the composite, suggesting that the TiO₂/AC composites with high purity have been successfully synthesized in this study.

Further evidence was provided by the TEM micrographs shown in Figure 5. It is clearly indicated that the TiO₂ particle (black region) with nanosized dimension is uniformly deposited on the surface as well as in the bulk of the AC (gray region), and the large scale agglomerate is not detected in the TiO₂/AC composites synthesized at 1 and 2 loading cycles (Figures 5(a) and 5(b)). However, when the TiO₂/AC-3 photocatalyst was synthesized at 3 loading cycles, the as-formed TiO₂ particles are inclined to agglomerate (Figure 5(c)). It suggests that the TiO₂ particles are easier to agglomerate on the surface of the TiO₂/AC composites with increasing

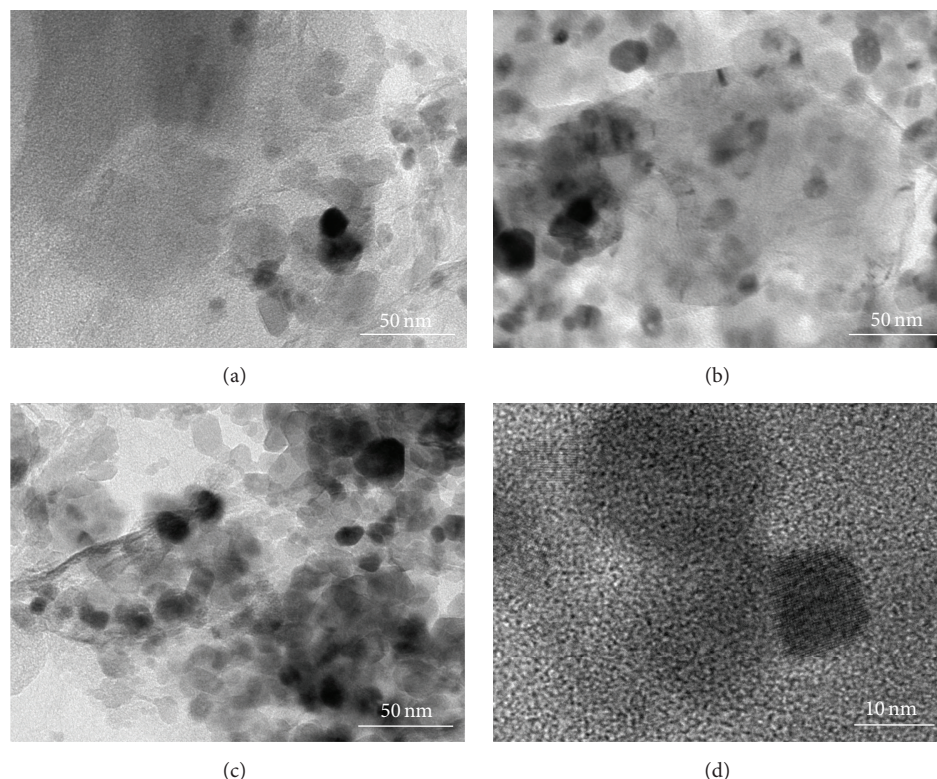


FIGURE 5: TEM micrographs of TiO_2/AC composites: (a) TiO_2/AC -1, (b) TiO_2/AC -2, (c) TiO_2/AC -3, and (d) HRTEM image of TiO_2/AC -2.

the loading cycle. It is well known that the photocatalytic activity of TiO_2 composite functional materials strongly depends on their morphological structure [14, 38]. Compared with the TiO_2 particles deposited homogeneously on the surface of TiO_2/AC -1 and TiO_2/AC -2, the agglomerated TiO_2 particles in the TiO_2/AC -3 composites may hamper the light incidence on these photoreactive sites and consequently reduce its photocatalytic degradation efficiency. Furthermore, the TiO_2 particle size in composite photocatalyst can be estimated to about 10–20 nm in the high resolution TEM image (Figure 5(d)), which is good in accordance with the crystal size obtained by means of XRD pattern.

3.5. Photocatalytic Degradation of RhB. Photocatalytic activity for the obtained pure TiO_2 as well as TiO_2/AC composites was estimated by measuring the decomposition rate of RhB in aqueous solution in the presence of UV light irradiation, and the results are shown in Figure 6. For the original AC (Figure 6(a)), the removal of RhB increases gradually with the increasing adsorption time, and about 71.0% of the initial RhB is removed until reaching the adsorption equilibrium at the end of 90 min in the dark. The removal rate of RhB is almost unchanged with increasing the adsorption time in the UV light irradiation. Nevertheless, the RhB removal rate of pure TiO_2 is negligible when the solution is kept in the dark for 90 min but increases noticeably with prolonging the time of UV light irradiation, and the final removal rate of RhB reaches only 55.8%, which is mainly attributed to

the photocatalytic degradation process. However, for the TiO_2/AC composites (Figure 6(b)), the RhB removal process in aqueous solution can be divided into two stages: the removal process of 90 min in the dark, which is mainly attributed to the adsorption effect of TiO_2/AC composites. The other stage is the 120 min in the UV light irradiation, which is mainly caused by the photocatalytic degradation. In this paper, the concentration of RhB maintained in the aqueous solution at the end of adsorption stage in the dark is taken as the starting concentration of RhB in the photocatalytic degradation stage, and the degradation percentages of TiO_2/AC composites were calculated according to this reference. As shown in Figure 6, the initial removal rate of TiO_2/AC composites was similar to AC, but, after 90 min in the dark, the TiO_2/AC composites are still able to remove the RhB by the photocatalytic degradation effect on the UV light irradiation; as a result, the percentages of RhB removal continue to increase. The final percentages of RhB removed by TiO_2/AC -1, TiO_2/AC -2, and TiO_2/AC -3 reach 82.0%, 93.2%, and 86.3%, respectively. The RhB removal rate of TiO_2/AC composites is far superior for pure TiO_2 synthesized in this study or macroporous TiO_2 photocatalyst reported in our previous work [39].

Based on the results that the percentages of RhB removal are 66.1%, 46.7%, and 38.9% after 90 min in the dark by adsorption, the photocatalytic degradation percentage of RhB is 15.9% for TiO_2/AC -1, 46.5% for TiO_2/AC -2, and 47.4% for TiO_2/AC -3, respectively. Clearly, the photocatalytic degradation percentage of RhB for TiO_2/AC -2 is almost

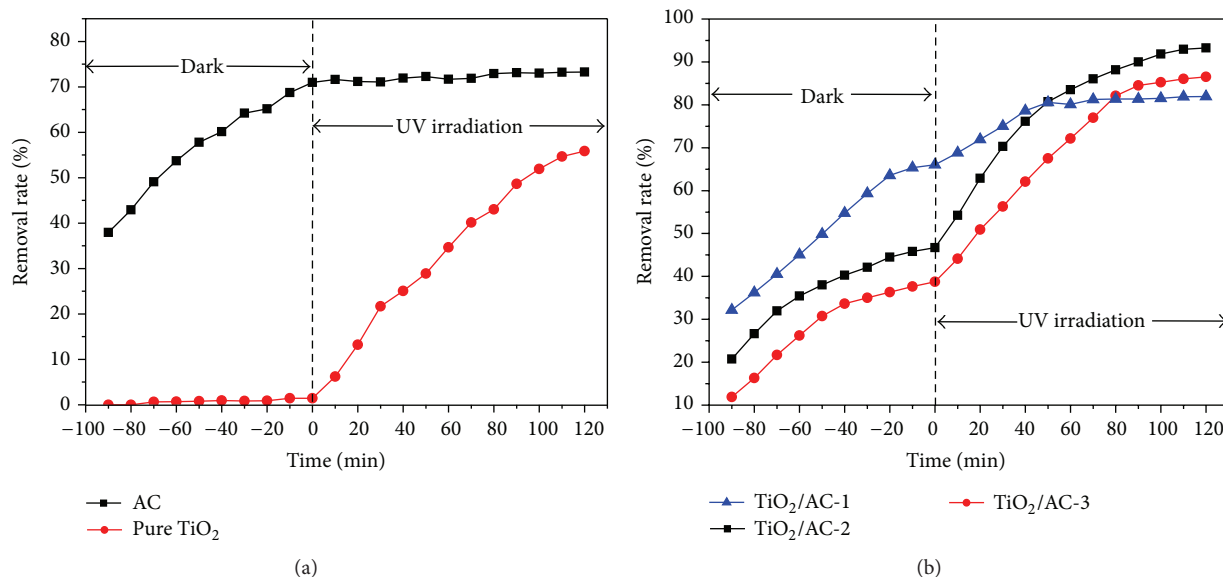


FIGURE 6: RhB removal rate of pure TiO₂, AC, and composite photocatalysts: (a) pure TiO₂ and AC, (b) TiO₂/AC composite photocatalysts.

equivalent to that for TiO₂/AC-3, but the loading amount of TiO₂ in TiO₂/AC-2 for 15.5% is lower than that in TiO₂/AC-3 for 26.7%, indicating that the photocatalytic activity of nanosized TiO₂ in TiO₂/AC-2 is higher than that in TiO₂/AC-3. The fundamental mechanism for this can be clarified as follows: the TiO₂/AC composites exhibit the dual functions such as adsorption and photocatalytic degradation to remove the RhB in the aqueous solution [13, 38, 40]; the proposed schematic illustration is shown in Figure 7, which is also similar to the case on the photocatalyst of TiO₂/ACF nanocomposites [41]. Under dark condition, the removal process depends strongly on the adsorption performance of substrate AC. However, under UV light irradiation, the RhB removal process requires the pollutant to be adsorbed on the TiO₂/AC composites surface prior to immediate photocatalytic degradation [15, 42]. Therefore, the efficiency of photocatalytic reaction can be affected by the adsorption performance of substrate AC and the photocatalytic activity nanosized TiO₂ particles.

For the TiO₂/AC-1, the RhB removed by adsorption is predominant because of its well-developed porosity, and the final RhB removal rate reaches 82.0%, while the photocatalytic degradation percentage of RhB is only 15.9%, which may be ascribed to the limited TiO₂ particles that deposited on the composite photocatalyst. With the increasing loading cycle during the preparation of TiO₂/AC composites, more TiO₂ will be exposed on the surface of AC. As a result, photoreactive sites available on the AC surface increase, which contributes to the high photocatalytic activity of TiO₂/AC composites. Therefore, the photocatalytic degradation percentage of RhB for TiO₂/AC-2 can reach 46.5%, and the final RhB removal rate can reach 93.2% even if the adsorption effect is weakened due to the reduced porosity of composite photocatalyst. However, for the TiO₂/AC-3, the photocatalytic degradation percentage of RhB is not enhanced as expected in terms of the loading amount

of TiO₂ in composite photocatalyst. The reason may be attributed to the fact that a certain amount of nanosized TiO₂ particles aggregates on the surface of TiO₂/AC-3, which can reduce the efficient UV light absorption and decrease the photoreactive sites for degradation. On the other hand, the reduction of the porosity results in the fact that the RhB adsorbed on the TiO₂/AC composites surface is very limited, and the efficiency of photocatalytic degradation is also restricted consequently. The results indicate clearly that the morphological structure of TiO₂/AC composites such as porosity and the dispersibility of TiO₂ particles on the surface of composite photocatalyst are crucial for obtaining high photocatalytic activity. Therefore, the loading cycle is considered a significant factor in preparation of TiO₂/AC composites by sol-gel method.

4. Conclusions

It is found that TiO₂/AC composites can be synthesized simply by sol-gel method under calcination at 500°C. The TiO₂ particles deposited on the AC surface display mainly anatase crystal structure with a crystallite size of 10–20 nm. The morphological structure and photocatalytic activity of composite photocatalyst are strongly dependent on the loading cycle. The porosity of TiO₂/AC composites may decrease gradually and the dispersibility of TiO₂ particles on the AC surface becomes less uniform after multiloading cycles due to more TiO₂ particles deposited on the AC surface, which leads to blocking or covering of part of the micropores. The photocatalytic degradation of RhB experiments indicates that the optimized composite photocatalyst of TiO₂/AC-2 synthesized at 2 loading cycles demonstrates the highest photocatalytic activity, which can lead to 93.2% RhB being rapidly removed from aqueous solution under UV light irradiation. The high removal rate of RhB of TiO₂/AC composite is attributed to the excellent adsorption effect in the dark and

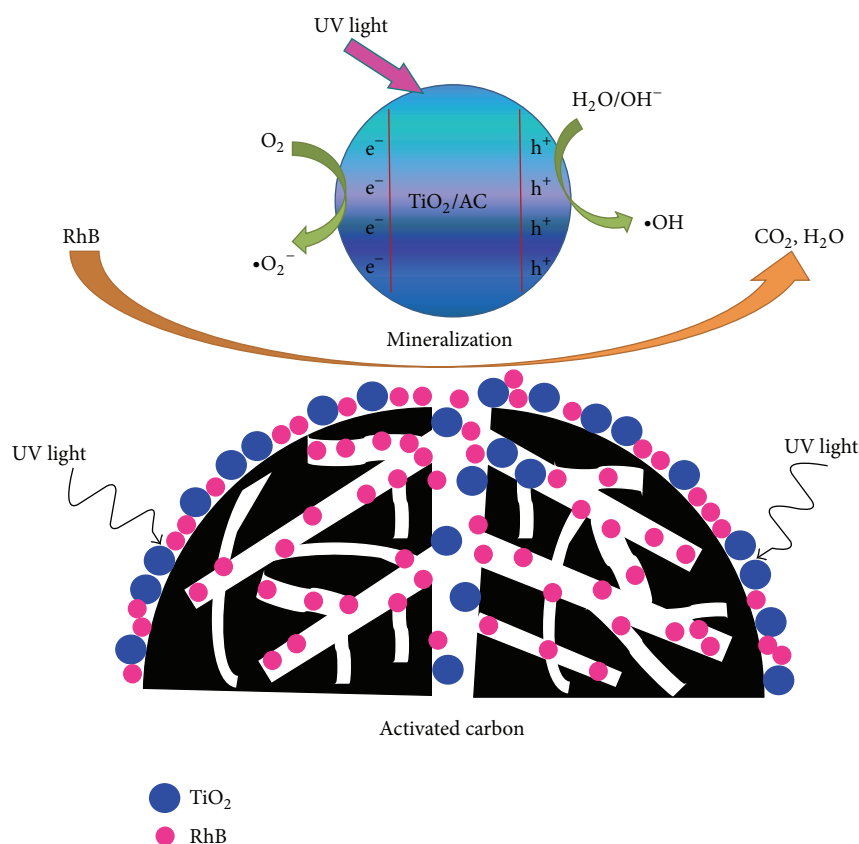


FIGURE 7: Proposed schematic illustration for the adsorption and photocatalytic degradation of RhB on the TiO_2/AC composites under UV light irradiation.

high efficiency photocatalytic degradation in the presence of UV light irradiation.

Conflict of Interests

The authors declare that there is no conflict of interests regarding the publication of this paper.

Acknowledgments

The authors gratefully acknowledge the financial support of the National Natural Science Foundation of China (51404098, 51174077, 51404097, and U1361119), International Science and Technology Cooperation Project of Henan province (152102410047), Education Department Science Foundation of Henan province (13A430336), and Opening Project of Henan Key Discipline Open Laboratory of Mining Engineering Materials (MEM13-7, MEM13-12, and MEM14-5).

References

- [1] M. Rafatullah, O. Sulaiman, R. Hashim, and A. Ahmad, "Adsorption of methylene blue on low-cost adsorbents: a review," *Journal of Hazardous Materials*, vol. 177, no. 1–3, pp. 70–80, 2010.
- [2] V. K. Gupta, R. Kumar, A. Nayak, T. A. Saleh, and M. A. Barakat, "Adsorptive removal of dyes from aqueous solution onto carbon nanotubes: a review," *Advances in Colloid and Interface Science*, vol. 193–194, pp. 24–34, 2013.
- [3] N. M. Mahmoodi, R. Salehi, M. Arami, and H. Bahrami, "Dye removal from colored textile wastewater using chitosan in binary systems," *Desalination*, vol. 267, no. 1, pp. 64–72, 2011.
- [4] N. F. Cardoso, E. C. Lima, B. Royer et al., "Comparison of *Spirulina platensis* microalgae and commercial activated carbon as adsorbents for the removal of Reactive Red 120 dye from aqueous effluents," *Journal of Hazardous Materials*, vol. 241–242, pp. 146–153, 2012.
- [5] M. Asiltürk and Ş. Şener, "TiO₂-activated carbon photocatalysts: preparation, characterization and photocatalytic activities," *Chemical Engineering Journal*, vol. 180, pp. 354–363, 2012.
- [6] Z. H. Zhang, Y. Xua, X. P. Ma et al., "Microwave degradation of methyl orange dye in aqueous solution in the presence of nano-TiO₂-supported activated carbon (supported-TiO₂/AC/MW)," *Journal of Hazardous Materials*, vol. 209–210, pp. 271–277, 2012.
- [7] V. K. Gupta and Suhas, "Application of low-cost adsorbents for dye removal—a review," *Journal of Environmental Management*, vol. 90, no. 8, pp. 2313–2342, 2009.
- [8] Y. J. Li, X. M. Zhou, W. Chen et al., "Photodecolorization of Rhodamine B on tungsten-doped TiO₂/activated carbon under visible-light irradiation," *Journal of Hazardous Materials*, vol. 227–228, pp. 25–33, 2012.
- [9] P. Jiang, D. Ren, D. He, W. Fu, J. Wang, and M. Gu, "An easily sedimentable and effective TiO₂ photocatalyst for removal of

- dyes in water," *Separation and Purification Technology*, vol. 122, pp. 128–132, 2014.
- [10] E. Forgacs, T. Cserháti, and G. Oros, "Removal of synthetic dyes from wastewaters: a review," *Environment International*, vol. 30, no. 7, pp. 953–971, 2004.
- [11] M. H. Do, N. H. Phan, T. D. Nguyen et al., "Activated carbon/Fe₃O₄ nanoparticle composite: fabrication, methyl orange removal and regeneration by hydrogen peroxide," *Chemosphere*, vol. 85, no. 8, pp. 1269–1276, 2011.
- [12] P.-J. Lu, H.-C. Lin, W.-T. Yu, and J.-M. Chern, "Chemical regeneration of activated carbon used for dye adsorption," *Journal of the Taiwan Institute of Chemical Engineers*, vol. 42, no. 2, pp. 305–311, 2011.
- [13] G. Xue, H. H. Liu, Q. Y. Chen, C. Hills, M. Tyrer, and F. Innocent, "Synergy between surface adsorption and photocatalysis during degradation of humic acid on TiO₂/activated carbon composites," *Journal of Hazardous Materials*, vol. 186, no. 1, pp. 765–772, 2011.
- [14] Y.-J. Xu, Y. B. Zhuang, and X. Z. Fu, "New insight for enhanced photocatalytic activity of TiO₂ by doping carbon nanotubes: a case study on degradation of benzene and methyl orange," *Journal of Physical Chemistry C*, vol. 114, no. 6, pp. 2669–2676, 2010.
- [15] T.-T. Lim, P.-S. Yap, M. Srinivasan, and A. G. Fane, "TiO₂/AC composites for synergistic adsorption-photocatalysis processes: present challenges and further developments for water treatment and reclamation," *Critical Reviews in Environmental Science and Technology*, vol. 41, no. 13, pp. 1173–1230, 2011.
- [16] C. Andriantsiferana, E. F. Mohamed, and H. Delmas, "Photocatalytic degradation of an azo-dye on TiO₂/activated carbon composite material," *Environmental Technology*, vol. 35, no. 3, pp. 355–363, 2014.
- [17] A. E. Eliyas, L. Ljutzkanov, I. D. Stambolova et al., "Visible light photocatalytic activity of TiO₂ deposited on activated carbon," *Central European Journal of Chemistry*, vol. 11, no. 3, pp. 464–470, 2013.
- [18] W. Y. Dong, C. W. Lee, X. C. Lu et al., "Synchronous role of coupled adsorption and photocatalytic oxidation on ordered mesoporous anatase TiO₂-SiO₂ nanocomposites generating excellent degradation activity of RhB dye," *Applied Catalysis B: Environmental*, vol. 95, no. 3-4, pp. 197–207, 2010.
- [19] X. D. Wang, F. Shi, W. Huang, and C. M. Fan, "Synthesis of high quality TiO₂ membranes on alumina supports and their photocatalytic activity," *Thin Solid Films*, vol. 520, no. 7, pp. 2488–2492, 2012.
- [20] S. K. Padmanabhan, S. Pal, E. Ul Haq, and A. Licciulli, "Nanocrystalline TiO₂-diatomite composite catalysts: effect of crystallization on the photocatalytic degradation of rhodamine B," *Applied Catalysis A: General*, vol. 485, pp. 157–162, 2014.
- [21] M. N. Chong, Z. Y. Tneu, P. E. Poh, B. Jin, and R. Aryal, "Synthesis, characterisation and application of TiO₂-zeolite nanocomposites for the advanced treatment of industrial dye wastewater," *Journal of the Taiwan Institute of Chemical Engineers*, vol. 50, pp. 288–296, 2015.
- [22] V. Belessi, D. Lambropoulou, I. Konstantinou et al., "Structure and photocatalytic performance of TiO₂/clay nanocomposites for the degradation of dimethachlor," *Applied Catalysis B: Environmental*, vol. 73, no. 3, pp. 292–299, 2007.
- [23] E. Rossetto, D. I. Petkowicz, J. H. Z. dos Santos, S. B. C. Pergher, and F. G. Penha, "Bentonites impregnated with TiO₂ for photodegradation of methylene blue," *Applied Clay Science*, vol. 48, no. 4, pp. 602–606, 2010.
- [24] M. S. A. S. Shah, A. R. Park, K. Zhang, J. H. Park, and P. J. Yoo, "Green synthesis of biphasic TiO₂-reduced graphene oxide nanocomposites with highly enhanced photocatalytic activity," *ACS Applied Materials and Interfaces*, vol. 4, no. 8, pp. 3893–3901, 2012.
- [25] L. Zhu, S. B. Jo, J. H. Jo, S. Ye, K. Ullah, and W. C. Oh, "Characterization of a novel MnS-ACF/TiO₂ composite and photocatalytic mechanism derived from organic dye decomposition," *Journal of the Korean Ceramic Society*, vol. 51, no. 3, pp. 139–144, 2014.
- [26] W. J. Lee, J. M. Lee, S. T. Kochuveedu et al., "Biomaterialized N-doped CNT/TiO₂ core/shell nanowires for visible light photocatalysis," *ACS Nano*, vol. 6, no. 1, pp. 935–943, 2012.
- [27] P. Muthirulan, C. K. Nirmala Devi, and M. Meenakshi Sundaram, "Fabrication and characterization of efficient hybrid photocatalysts based on titania and graphene for acid orange seven dye degradation under UV irradiation," *Advanced Materials Letters*, vol. 5, no. 4, pp. 163–171, 2014.
- [28] H. Slimen, A. Houas, and J. P. Nogier, "Elaboration of stable anatase TiO₂ through activated carbon addition with high photocatalytic activity under visible light," *Journal of Photochemistry and Photobiology A: Chemistry*, vol. 221, no. 1, pp. 13–21, 2011.
- [29] X. J. Wang, Y. F. Liu, Z. H. Hu, Y. J. Chen, W. Liu, and G. H. Zhao, "Degradation of methyl orange by composite photocatalysts nano-TiO₂ immobilized on activated carbons of different porosities," *Journal of Hazardous Materials*, vol. 169, no. 1–3, pp. 1061–1067, 2009.
- [30] T. S. Jamil, M. Y. Ghaly, N. A. Fathy, T. A. Abd El-Halim, and L. Österlund, "Enhancement of TiO₂ behavior on photocatalytic oxidation of MO dye using TiO₂/AC under visible irradiation and sunlight radiation," *Separation and Purification Technology*, vol. 98, pp. 270–279, 2012.
- [31] Z. He, S. Yang, Y. Ju, and C. Sun, "Microwave photocatalytic degradation of Rhodamine B using TiO₂ supported on activated carbon: mechanism implication," *Journal of Environmental Sciences*, vol. 21, no. 2, pp. 268–272, 2009.
- [32] Y. H. Zhang, Z. R. Tang, X. Z. Fu, and Y. J. Xu, "TiO₂-graphene nanocomposites for gas-phase photocatalytic degradation of volatile aromatic pollutant: is TiO₂-graphene truly different from other TiO₂-carbon composite materials?" *ACS Nano*, vol. 4, no. 12, pp. 7303–7314, 2010.
- [33] J. R. Utrilla, M. S. Polo, M. M. Abdeldaiem, and R. O. Pérez, "Role of activated carbon in the photocatalytic degradation of 2,4-dichlorophenoxyacetic acid by the UV/TiO₂/activated carbon system," *Applied Catalysis B: Environmental*, vol. 126, pp. 100–107, 2012.
- [34] C. Zhang, D. Long, B. Xing et al., "The superior electrochemical performance of oxygen-rich activated carbons prepared from bituminous coal," *Electrochemistry Communications*, vol. 10, no. 11, pp. 1809–1811, 2008.
- [35] H. P. Klug and L. E. Alexander, *X-Ray Diffraction Procedures for Polycrystalline and Amorphous Materials*, John Wiley & Sons, New York, NY, USA, 2nd edition, 1974.
- [36] Z. L. Zhu, A. M. Li, S. Zhong, F. Q. Liu, and Q. X. Zhang, "Preparation and characterization of polymer-based spherical activated carbons with tailored pore structure," *Journal of Applied Polymer Science*, vol. 109, no. 3, pp. 1692–1698, 2008.
- [37] D. Huang, Y. Miyamoto, T. Matsumoto et al., "Preparation and characterization of high-surface-area TiO₂/activated carbon by low-temperature impregnation," *Separation and Purification Technology*, vol. 78, no. 1, pp. 9–15, 2011.

- [38] S. G. Kumar and L. G. Devi, "Review on modified TiO₂ photocatalysis under UV/visible light: selected results and related mechanisms on interfacial charge carrier transfer dynamics," *Journal of Physical Chemistry A*, vol. 115, no. 46, pp. 13211–13241, 2011.
- [39] G. Yi, B. Xing, J. Jia et al., "Fabrication and characteristics of macroporous TiO₂ photocatalyst," *International Journal of Photoenergy*, vol. 2014, Article ID 783531, 7 pages, 2014.
- [40] C. K. Gu and C. Shannon, "Investigation of the photocatalytic activity of TiO₂-polyoxometalate systems for the oxidation of methanol," *Journal of Molecular Catalysis A: Chemical*, vol. 262, no. 1-2, pp. 185–189, 2007.
- [41] X. D. Wang, K. Zhang, X. L. Guo, G. D. Shen, and J. Y. Xiang, "Synthesis and characterization of N-doped TiO₂ loaded onto activated carbon fiber with enhanced visible-light photocatalytic activity," *New Journal of Chemistry*, vol. 38, no. 12, pp. 6139–6146, 2014.
- [42] A. Omri and M. Benzina, "Almond shell activated carbon: adsorbent and catalytic support in the phenol degradation," *Environmental Monitoring and Assessment*, vol. 186, no. 6, pp. 3875–3890, 2014.

Review Article

Recent Progress of TiO₂-Based Anodes for Li Ion Batteries

Yu Liu¹ and Yefeng Yang²

¹School of Chemistry and Chemical Engineering, Jiangsu University, Zhenjiang 212013, China

²Department of Materials Engineering, College of Materials and Textile, Zhejiang Sci-Tech University, Hangzhou 310018, China

Correspondence should be addressed to Yu Liu; liuyu@ujs.edu.cn and Yefeng Yang; yangyf@zstu.edu.cn

Received 9 November 2015; Accepted 3 January 2016

Academic Editor: Donglu Shi

Copyright © 2016 Y. Liu and Y. Yang. This is an open access article distributed under the Creative Commons Attribution License, which permits unrestricted use, distribution, and reproduction in any medium, provided the original work is properly cited.

TiO₂-based materials have been widely studied in the field of photocatalysis, sensors, and solar cells. Besides that, TiO₂-based materials are of great interest for energy storage and conversion devices, in particular rechargeable lithium ion batteries (LIBs). TiO₂ has significant advantage due to its low volume change (<4%) during Li ion insertion/desertions process, short paths for fast lithium ion diffusion, and large exposed surface offering more lithium insertion channels. However, the relatively low theoretical capacity and electrical conductivity of TiO₂ greatly hampered its practical application. Various strategies have been developed to solve these problems, such as designing different nanostructured TiO₂ to improve electronic conductivity, coating or combining TiO₂ with carbonaceous materials, incorporating metal oxides to enhance its capacity, and doping with cationic or anionic dopants to form more open channels and active sites for Li ion transport. This review is devoted to the recent progress in enhancing the LIBs performance of TiO₂ with various synthetic strategies and architectures control. Based on the lithium storage mechanism, we will also bring forward the existing challenges for future exploitation and development of TiO₂-based anodes in energy storage, which would guide the development for rationally and efficiently designing more efficient TiO₂-based LIBs anodes.

1. Introduction

Lithium ion batteries (LIBs) are becoming the best choice in portable electronics, implantable devices, power tools, and hybrid/full electric vehicles (EVs) for their high working voltage, low self-discharge rate, long cycle life, high energy, and power density [1, 2]. Using electric vehicles instead of traditional gasoline powered transportation can significantly reduce pollution of combustion gas and increase energy security. More importantly, the high energy efficiency of LIBs also has potential application in various large electric grid applications, including improving the energy efficiency of wind, solar, tidal, and other clean energy; thus LIBs are expected to have a very favorable impact on building an energy-sustainable economy [3, 4]. Figure 1 shows the forecasted evolution of the LIBs demand in the future years [5]; we think we will see economical battery-driven electric vehicles sooner than most people expect.

Up to now, the vast majority of commercial LIBs rely, at the cathode side, on transition metals oxides or phosphates active material (LiCoO₂ [6], LiNiO₂ [7], LiMnO₂ [8], LiFePO₄ [9], LiMnPO₄ [10], etc.), while graphite is

commonly used as anode active material. Figure 2 is the principle of a typical lithium ion battery; both anodes and cathodes could shuttle lithium ion back and forth between them. The electrolyte is usually made of polypropylene/polyethylene which contains lithium salts (i.e., LiPF₆) in alkyl organic carbonates. The separator between anode and cathode can allow the diffusion of Li ions from cathode to anode during the charging and the reverse discharging process.

The anode is a crucial part in LIBs; therefore, the research and the development on the current situation of anode materials are one of the most important factors to determine the performance of this device. An ideal anode material shall meet the following requirements [11, 12]: (1) high specific surface area and large exposed surface offering more lithium insertion channels, (2) low volume change during Li ion insertion/desertions process, which is important for good cycling stability, (3) large pore size and short paths for fast lithium ion diffusion with high speed, which is crucial for good rate capability, (4) low internal resistance which leads to fast charging and discharging, (5) low intercalation potential for Li, (6) low price, (7) environment friendly. Based on the

TABLE 1: Comparison of advantages and limitations of TiO_2 and other anode materials [11–15].

Materials	Theoretical capacity (mA h g^{-1})	Advantages	Common issues
TiO_2	330	Fast lithium ion diffusion; low cost; environmentally friendly; good safety	Low capacity; low electrical conductivity; poor rate capability
Metal oxides (CuO , NiO , Fe_3O_4 , etc.)	500–1200	High capacity; high energy; low cost	Low coulombic efficiency; unstable SEI formation; low electrical conductivity; poor capacity retention
Carbon	372	Good working potential; low cost; good safety	Low coulombic efficiency; high irreversible capacity
Si	4200	High specific capacities	Large irreversible capacity; poor cycling
Sn	990	Good safety; low cost; good electrical conductivity	Poor cycling

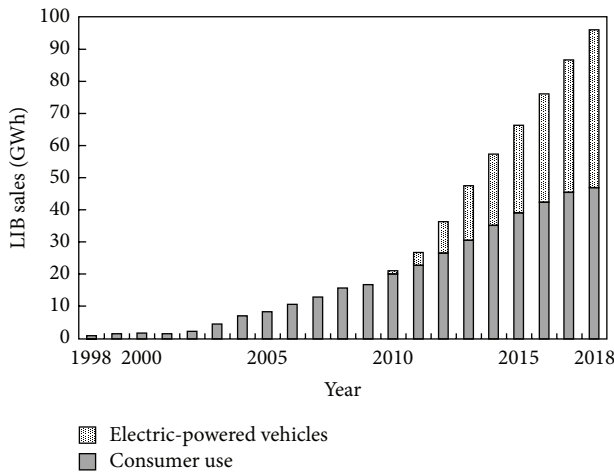
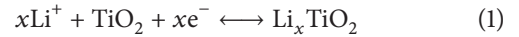


FIGURE 1: Forecasted expansion in demand for lithium ion batteries. Reprinted from [5].

Li ion storage mechanisms, anode materials can be classified into the following categories: carbon based materials, such as graphite, amorphous carbon, carbon nanotubes, and graphene; alloy/dealloy materials, such as Si, Sn, Ge, Al, and Bi; transition metal oxides (M_xO_y , $\text{M} = \text{Cu}$, Mn , Fe , Co , Ni , etc.); metal sulphides; metal phosphides and metal nitrides [13–15]. Figure 3 shows the potential versus Li/Li^+ and the corresponding capacity density of some potential active anode materials. In the whole, transition metal oxides always have relatively higher potential and capacity.

Among these transition metal oxides, TiO_2 is one of the most promising anode candidates for LIBs, which exhibits excellent structural stability, high discharge voltage plateau (more than 1.7 V versus Li^+/Li), excellent cycling stability, environmentally friendly, high safety, and low cost [16, 17]. However, some limitations of TiO_2 exist as well, such as low capacity, low electrical conductivity, and poor rate capability. Table 1 compares advantages and limitations of TiO_2 and other anode materials. The reversible lithium ion insertion

and extraction from TiO_2 occur according to the following reaction [18]:



where x can range between 0 and 1, depending strongly on the TiO_2 polymorph, particle size, and morphology. Therefore, the electrochemical performance of TiO_2 highly depends on their structural parameters such as crystallinity, size, morphology, polymorphs, and specific surface area. Table 2 summarizes the structural and electrochemical profiles of various TiO_2 polymorphs [19]. Amongst these, the anatase, rutile, brookite, and bronze phases of TiO_2 have been reported for LIBs applications. However, there are some problems which exist in practical application, that is, low electrical conductivity (10^{-12} – $10^{-7} \text{ s cm}^{-1}$) and diffusion coefficient of lithium ions (10^{-15} – $10^{-9} \text{ cm}^2 \text{ s}^{-1}$), always leading to the poor rate capability of TiO_2 anodes, which result from their low electric conductivity with the lack of open channels [20–22].

Based on the analysis of shortcomings of TiO_2 anodes, several different strategies have been developed to address these issues of TiO_2 -based anodes and summarized in this review, such as designing different nanostructured TiO_2 , coating or combining TiO_2 with carbonaceous materials and metal oxides to change the physical and chemical surface, and selective doping with heteroatoms to form more open channels and active sites for Li ion transport, as well as increasing the intrinsic conductivity. Indeed, these methods lead to many advantages in improving the capacity, cycling stability, and rate capability of TiO_2 .

2. Research on the LIBs Property of TiO_2 -Based Anodes

2.1. Different Structures. Different structures usually exhibit unique performance based on their surface and structural properties. Thus, various morphologies of TiO_2 have been synthesized to obtain superior electrochemical properties.

2.1.1. One-Dimensional Nanostructures. One-dimensional (1D) nanostructures including nanorods, nanoneedles,

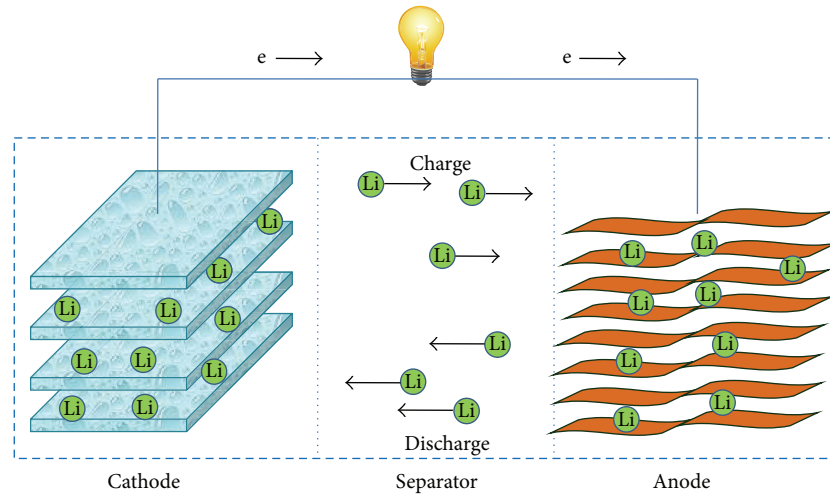


FIGURE 2: Schematic representation of lithium insertion/deinsertion mechanism for current rechargeable lithium battery.

TABLE 2: Structural and electrochemical properties of various TiO_2 polymorphs [19].

Structure	Space group	Density (g cm^{-3})	Lattice parameter values	Lithiation quantity (mole)	
				Bulk	Nano
Rutile	Tetragonal $P4_2/mnm$	4.13	$a = 4.59,$ $c = 2.96$	0.1	0.85
Anatase	Tetragonal $I4_1/amd$	3.79	$a = 3.79,$ $c = 9.51$	0.5	1.0
Brookite	Orthorhombic $Pbcv$	3.99	$a = 9.17,$ $b = 5.46,$ $c = 5.14$	0.1	1.0
TiO_2 -B (bronze)	Monoclinic $C2/m$	3.64	$a = 12.17,$ $b = 3.74,$ $c = 6.51,$ $\beta = 107.298$	0.71	1.0
TiO_2 -II (Columbite)	Orthorhombic $Pbcn$	4.33	$a = 4.52,$ $b = 5.5,$ $c = 4.94$		
TiO_2 -H (hollandite)	Tetragonal $I4/m$	3.46	$a = 10.18,$ $c = 2.97$		
TiO_2 -III (baddeleyite)	Monoclinic $P2_1/c$		$a = 4.64,$ $b = 4.76,$ $c = 4.81,$ $\beta = 99.28$		
TiO_2 -R (ramsdellite)	Orthorhombic $Pbmn$	3.87	$a = 4.9,$ $b = 9.46,$ $c = 2.96$		
TiO_1 -O I	Orthorhombic				
TiO_2 -O II	Orthorhombic				

nanotubes, nanofibers, and nanowires could serve as an electron express way along the axial direction for electron collection due to a shorter collection time for the efficient electron transportation [31, 32]. For example, single-crystalline TiO_2 nanowires have an electron mobility of $\sim 1 \text{ cm}^2 \text{ V}^{-1} \text{ s}^{-1}$, nearly 1-2 orders higher than that of polycrystalline nanoparticles [33, 34]. Thus, 1D nanostructure is conducive to shorten the diffusion length for electrons and lithium, increase the electrode/electrolyte interfacial

area, and accommodate volume changes arising from the lithium ion insertion/extraction process [35]. Moreover, due to the unique structural flexibility, 1D material with good mechanical properties has potential in various binder-free and flexible electronics and photonics [36–38].

1D TiO_2 with different nanostructure (Figure 4) including nanotubes, nanofibers, and nanorods has been designed for high performance anodes in LIBs. The significance of 1D TiO_2 on battery performance was demonstrated by several

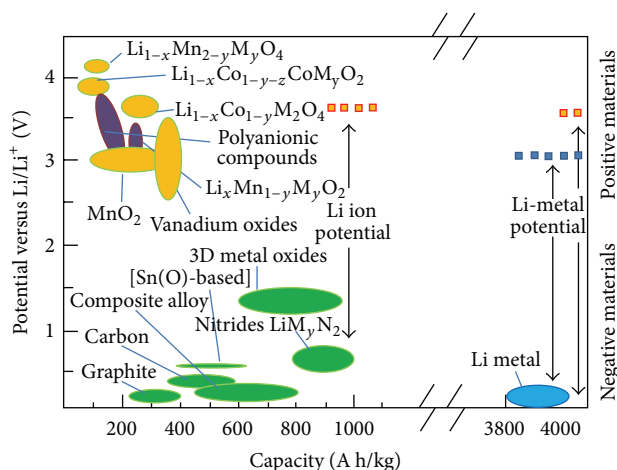


FIGURE 3: Comparing of some potential anode materials for lithium ion batteries.

groups. Tammawat and Meethong reported that anatase TiO_2 nanofiber anodes were directly used as an anode active material in LIBs without an additive or a binder. The nanofibers exhibited a high lithium storage capacity, a stable cycle life, and good rate capability [39]. The enhanced reversible capacity and cycling performance of the anatase TiO_2 nanofibers are attributed to the large surface area of the nanofibers, small nanocrystalline size, large Li nonstoichiometric parameters, and the increased electronic conductivity. Armstrong et al. prepared TiO_2 nanowires; these unique structures gave a higher capacity of 305 mA h g^{-1} compared to 240 mA h g^{-1} of bulk TiO_2 [40–42]. The enhanced capacity closely related to the good electronic conductivity and large surface area. Wei et al. reported a highly ordered anodic TiO_2 nanotube arrays with a tube length of 9 μm . These nanofibers exhibited significantly better microbattery performance (i.e., areal capacities, rate capability, and cycling stability) than both previously TiO_2 -based electrodes and other 3D microbattery electrodes. They suggested that the enhanced performance depends strongly on the long range ordering and crystallinity of the nanotube structures [18]. Wang et al. prepared a hybrid Li ion capacitor based on TiO_2 nanobelt array and graphene hydrogels cathode. It is found that the densities of the capacitor can reach an energy density of 21 Wh kg^{-1} and a high power density of 19 kW kg^{-1} [43]. The above studies also show that self-ordered 1D nanoarchitectures grown directly on a current collector are helpful to have a regularly oriented property and good contact with the current collector, enhancing the lithium ionic and electrical conductivities. Designing 1D structure is an effective way to improve the Li storage properties of TiO_2 .

2.1.2. Two-Dimensional Structure. Two-dimensional (2D) nanomaterials often have large exposed surfaces and specific facets, which is very effective in high energy storage applications such as LIBs and supercapacitors. More importantly, 2D nanostructures can offer short ion diffusion length and open charge transport channel for electrolyte penetration

and buffer the volume variations during the Li ion intercalation/deintercalation process [45–48]. Lithium insertion in this kind of material is just like surface lithium storage; both sides of 2D structure can store lithium ion, which can meet the requirement of fast and more lithium storage. A large number of 2D nanomaterials have been explored as anodes for LIBs, including graphene [49, 50], transition metal dichalcogenides (MoS_2 , WS_2) [51, 52], ternary transition metal carbides (Ti_3C_2 , Ti_2C) [53–55], and metal oxides (V_2O_5 , MoO_3) [56, 57].

For TiO_2 , 2D structures could provide stable framework, effective grain boundaries, and short path for lithium ion diffusion and storage compared with 0D nanoparticles and 1D nanostructures. Significant efforts have been made on the fabrication of 2D TiO_2 materials. Li et al. synthesized mesoporous TiO_2 nanoflakes with size of 10–20 nm via hydrothermal methods using $\text{Ti}(\text{SO}_4)_2$ as titanium source and NaOH solution as alkaline medium. The result of electrochemical performance test shows that the prepared TiO_2 nanoflakes with shorter calcining time have high discharge specific capacity ($261.5 \text{ mA h g}^{-1}$) and good cycling performance [25]. In the process of heat treatment, longer calcining time results in uneven nanometer size and obvious reunion phenomenon. Shorter calcining time usually leads to more stable structure and higher specific surface area. Thus, both the lithium storage specific capacity of TiO_2 and the cycling stability of the battery can be improved [25]. Zhu et al. first synthesized the mesoporous single-grain layer anatase TiO_2 nanosheets using a simple and easily reproducible method. The obtained TiO_2 nanosheets exhibited a discharge capacity of 73 mA h g^{-1} with obvious voltage plateaus over 4000 cycles, highlighting them as promising anode material for long-term LIBs [58]. Wu et al. demonstrated a simple and green approach for the synthesis of anatase petal-like TiO_2 nanosheets; the unique structure showed high capacity and good cycling stability. This is because obtained petal-like TiO_2 nanosheets showed a comparative surface area of $28.4 \text{ m}^2 \text{ g}^{-1}$, which should provide shorter diffusion distance for Li ions and should be beneficial for electrochemical performance of the electrode [29]. Some typical TiO_2 nanosheets used in the lithium storage were listed in Table 3. It can be seen that 2D TiO_2 nanosheets exhibit the superior capacities, improved cycling stability and rate capabilities, owing to unique exposed facets, shortened path, and reserved porous structures.

2.1.3. Three-Dimensional Porous Structure. Recently, three-dimensional (3D) porous structure materials exhibiting interesting electrochemical performance in LIBs have attracted more attention, due to their special nature including highly exposed skeleton, tunable pore size, high porosity, high specific surface area, and low bulk density [59, 60]. As described, first, the unique structure is conducive to enhance the diffusion kinetics for its short diffusion paths for Li ions. Second, the pores are beneficial to enable easy infiltration of electrolyte and fast liquid-phase Li ion diffusion, reducing the concentration polarization and increasing rate performance and capacity of the cell. Third, the continuous network of 3D porous structure can provide better electrical conductivity

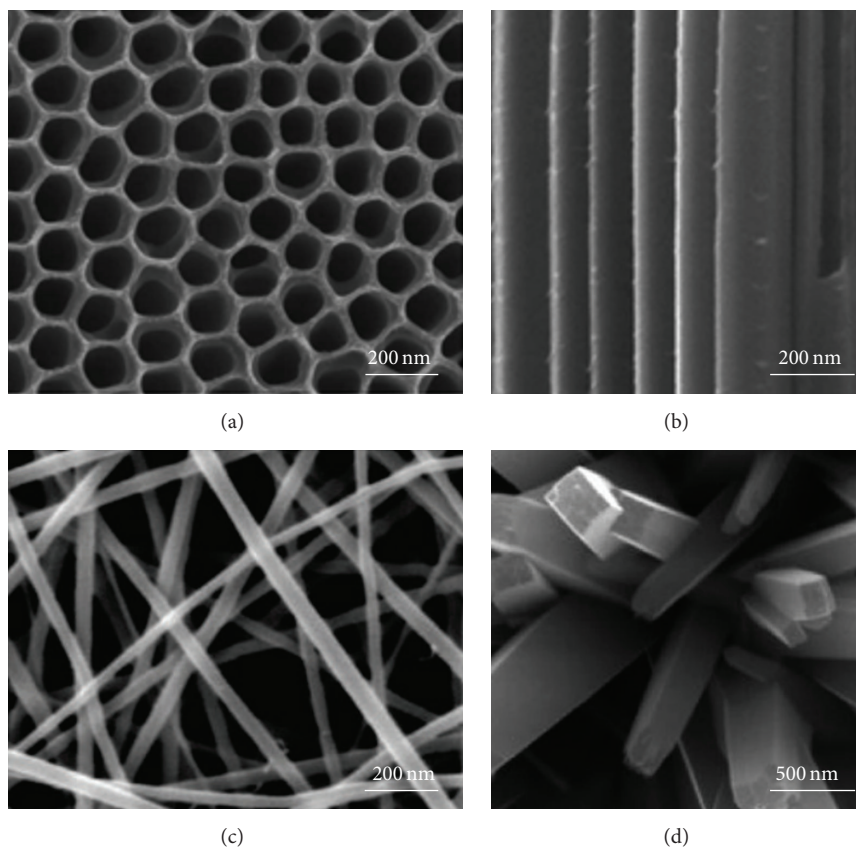


FIGURE 4: SEM images of different kinds of 1D TiO_2 nanostructures. Thin wall TiO_2 nanotubes ((a) and (b)), nanofibers (c), and nanorods (d). Reprinted from [18, 38, 44].

TABLE 3: The capacity of reported 2D TiO_2 materials for lithium storage.

Number	Structures	Performance		Ref.
		Reversible capacity	Charge/discharge rates	
1	Carbon-supported ultrathin anatase TiO_2 nanosheets	$\sim 150 \text{ mA h g}^{-1}$	850 mA g^{-1}	[23]
2	Anatase TiO_2 nanosheets	$\sim 150 \text{ mA h g}^{-1}$	1675 mA g^{-1}	[24]
3	TiO_2 nanoflakes	$\sim 261 \text{ mA h g}^{-1}$	33 mA g^{-1}	[25]
4	2D rutile TiO_2 - MoO_3 hybrid structure	$\sim 240 \text{ mA h g}^{-1}$	600 mA g^{-1}	[26]
5	Mesoporous TiO_2 nanobelts and graphene sheets	$\sim 430 \text{ mA h g}^{-1}$	1500 mA g^{-1}	[27]
6	TiO_2 hollow spheres	$\sim 148 \text{ mA h g}^{-1}$	850 mA g^{-1}	[28]
7	Mesoporous anatase TiO_2 sheets/rGO	$\sim 161 \text{ mA h g}^{-1}$	335 mA g^{-1}	[12]
8	petal-like TiO_2 nanosheets	$\sim 180 \text{ mA h g}^{-1}$	400 mA g^{-1}	[29]
9	Sandwich-like, stacked ultrathin titanate nanosheets	$\sim 170 \text{ mA h g}^{-1}$	850 mA g^{-1}	[30]
		$\sim 155 \text{ mA h g}^{-1}$	1700 mA g^{-1}	
		$\sim 135 \text{ mA h g}^{-1}$	3400 mA g^{-1}	

compared to loosely connected particles. Forth, the porosity in 3D structure should help in accommodating volume change during charging/discharging process and maintaining the structural integrity of the electrode [61, 62]. Up to now, different hollow structures such as hollow spheres, nanoboxes, and nanotubes are explored to be used as high

performance LIBs anodes [63–66]. And the same happens for TiO_2 ; the introduction of porosity into TiO_2 nanomaterials also can improve the cycling stability and increase the capacity at high charge-discharge rates due to the increased contact surface area and shortened path length for diffusion of Li ions [67–70]. Highly crystalline, nonordered mesoporous

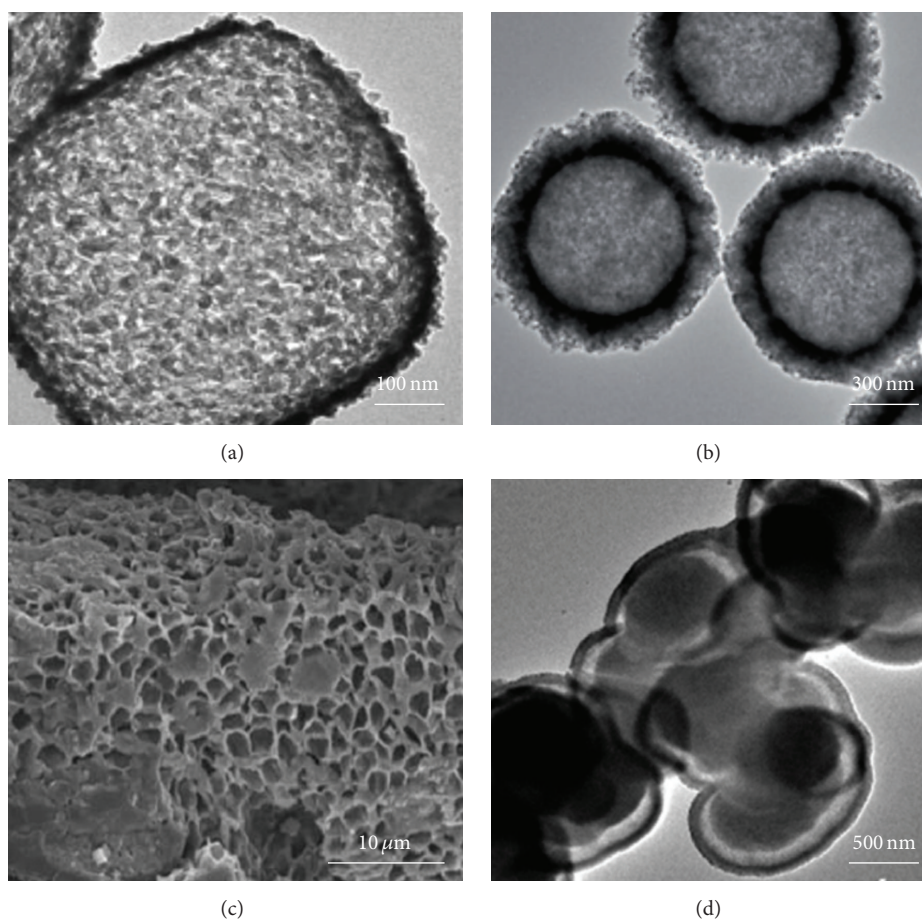


FIGURE 5: The morphology of different hollow TiO_2 structures. Reprinted from [67, 68, 73, 74].

TiO_2 nanocrystalline with high specific surface area and having anatase as the dominant phase have been reported by Gerbaldi and other researchers, which showed very high rate capability and excellent stability upon very prolonged cycling [71, 72]. Besides, the storage characteristics of the mesoporous samples in lithium test cells were reported, and a close correspondence between the structural properties of materials and the electrochemical performance was studied. The presence of mesopores is thought to be important for high rate performances and favorable for electrolyte ions transport. Lou's group recently reported the TiO_2 hollow spheres and submicroboxes, owing to the high surface area, porous shells, and small primary nanoparticles; these TiO_2 hollow structures possess significantly improved lithium storage properties with superior lithium storage properties in terms of high specific capacity, long-term cycling stability, and excellent rate capability [73, 74]. Figure 5 shows the typical morphology of different hollow TiO_2 structures, all of which exhibit outstanding electrochemical performance.

2.2. Coating or Combining TiO_2 with Carbonaceous Materials. Carbon materials such as active carbon, carbon nanotubes, and graphene have been extensively used for sorption, sensing, photocatalyst, electrocatalyst, and energy storage applications, owing to their abundance, accessibility, low health

risk, suitable surface areas, and extreme chemical and thermal stabilities [75–80]. Especially in LIBs and supercapacitors, carbon materials are very popular for their superior conductivity, good chemical stability, and mechanical property [81–84].

2.2.1. Carbon Coating. Carbon coating is an effective and common approach to improve the electrochemical performance of the anode materials. The role of carbon has also been studied, such as reducing the charge transfer resistance and improving the Li ions diffusion, enhancing electron transport, buffering the large volume changes during the charge/discharge process, and acting as a passivation layer to prevent the aggregation of active materials [66, 85, 86]. Some research has proved that the SEI (solid electrolyte interphase) film for carbon coated materials was found to be much thinner than the SEI film on uncoated active materials; thus, initial charge-discharge efficiency can be greatly enhanced [87, 88]. For example, Xia et al. investigated the effect of carbon coating on TiO_2 ; these TiO_2 /carbon hybrids could enhance electronic conductivity and provide flexible space for suppressing the large volume expansion during cycling [89]. E. Portenkirchner reports that the anatase TiO_{2-x} -C nanotubes demonstrate a superior Li storage capacity as high as $320 (\pm 68) \text{ mA h g}^{-1}$, nearly twice as high as pure TiO_{2-x} .

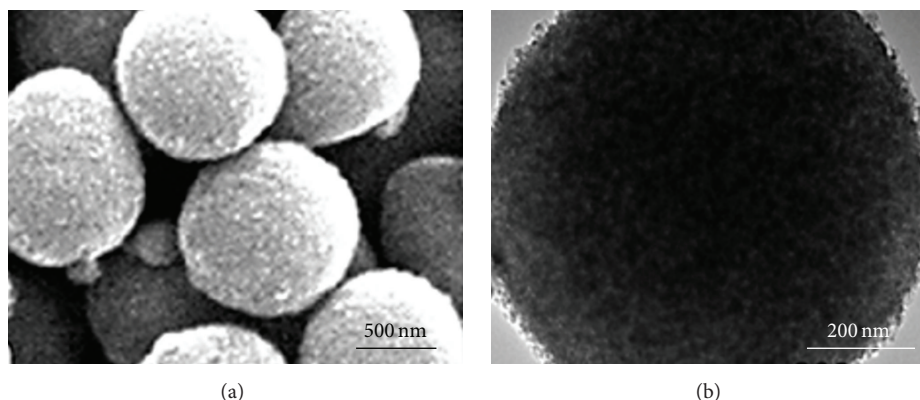


FIGURE 6: The morphology of carbon coated TiO_2 spheres and their cycling performance. Reprinted from [91].

Electrochemical impedance spectroscopy reveals smaller charge transfer resistances for $\text{TiO}_{2-x}\text{-C}$ nanotubes at the solid/liquid interface which improves the transfer of lithium ions from the electrolyte into the electrode [90]. Besides, the composites also showed higher initial charge-discharge efficiency compared to pure TiO_2 ; the reason can be ascribed to the formation of thinner SEI films. Zheng and coworkers prepared nitrogen-containing carbon modified porous TiO_2 composites. The as-prepared composites also exhibited enhanced rate performance and superior cyclability for LIBs compared to pure TiO_2 (Figure 6). The study indicates that N doping is favorable to improve the electronic conductivity and the composites possessed much lower charge transfer resistance than that of TiO_2 [91].

2.2.2. Combining TiO_2 with Carbon Nanotubes (CNTs). In recent years, CNTs have been approved to be a good anode material for lithium batteries due to their unique 1D structure, high conductivity (10^6 S m^{-1} for single-walled carbon nanotubes and $>10^5 \text{ S m}^{-1}$ for multiwalled carbon nanotubes), low gravity ($0.8\text{--}1.8 \text{ g cm}^{-3}$), high mechanical properties (Young's modulus of the order of 1.2 TPa), and high surface area ($>100 \text{ m}^2 \text{ g}^{-1}$) [92–96]. Some studies showed that CNTs could exhibit reversible capacities anywhere from 300 to 1000 mA h g^{-1} after chemical treatment; the value is significantly higher than the theoretical capacity of graphite (320 mA h g^{-1}) [97–100]. Numerous CNTs conjugated with a variety of nanostructured materials and metal oxides have been synthesized to obtain good electrochemical performance [101–103]. For example, CNTs@ TiO_2 composites have been synthesized by controlled hydrolysis of titanium isopropoxide over CNTs (as shown in Figures 7(a) and 7(b)). When CNTs are used as lithium ion battery electrodes, their inclusion is beneficial for an extreme enhancement of the rate capability of lithium ion uptake and release in TiO_2 ; it also favors the interfacial lithium ion intake from the solution by reducing the inherent charge transfer resistance. CNTs efficiently provide electrons to the nanostructure through the formation of Ti-C bonds, then effectively assisting lithium ion incorporation [104]. Zhao's group synthesized TiO_2 /CNTs composite through chemical vapor deposition method. The in situ synthesized composite showed better electrochemical

performance (high specific capacity and long-term cycling stability) than the pristine TiO_2 . This is because CNTs in the composites not only supply an efficient conductive network but also keep the structural stability of the TiO_2 particles, ultimately resulting in the improved electrochemical performance [105].

2.2.3. Combining TiO_2 with Graphene. Graphene is a single atomic plane of graphite and consists in a honey comb network of sp^2 carbons bonded into two-dimensional sheets with nanometer thickness, due to its unique properties, including high intrinsic carrier mobility ($200\,000 \text{ cm}^2 \text{ V}^{-1} \text{ s}^{-1}$), relevant mechanical strength, excellent conductivity ($5000 \text{ W m}^{-1} \text{ K}^{-1}$), high optical transmittance ($\sim 97.7\%$), large theoretical specific surface area ($2630 \text{ m}^2 \text{ g}^{-1}$), and superior mechanical strength which make graphene a suitable anode material for LIBs [105–111]. Besides, the rich functional groups on the surface of graphene make it an appealing 2D substrate for the anisotropic growth of different kinds of active materials [112, 113]. For example, Fang et al.'s group prepared novel mesoporous graphene nanosheets with an excellent reversible capacity of 833 mA h g^{-1} after 60 cycles [114]; this capacity is much higher than the theoretical lithium storage of graphite. This can be ascribed to the high contact surface area for lithium ion adsorption and intercalation, as well as edges and other defects. Thus, many synthetic strategies have been reported for TiO_2 /rGO hybrid nanostructures; Ti-C bond in the hybrids is crucial for rapid interfacial charge transferring. Etacheri et al. chemically bonded mesoporous TiO_2 nanosheets to rGO sheets through a photocatalytic reduction method, resulting in the formation of $\text{Ti}^{3+}\text{-C}$ bonds between TiO_2 and rGO. These TiO_2 /rGO hybrid nanostructures demonstrate superior specific capacity, excellent rate capability, and capacity retention compared to a physical mixture of TiO_2 and rGO [115]. The reason can be attributed to the higher electrochemical performance of TiO_2 /rGO hybrid nanostructures to efficient interfacial charge transfer between TiO_2 nanosheets and rGO, which is fostered by $\text{Ti}^{3+}\text{-C}$ bonds. Figure 8 shows the SEM and digital images of TiO_2 /rGO hybrid films; insets in Figure 8(b) display the flexibility of the corresponding films upon bending. The high flexibility of graphene could be an

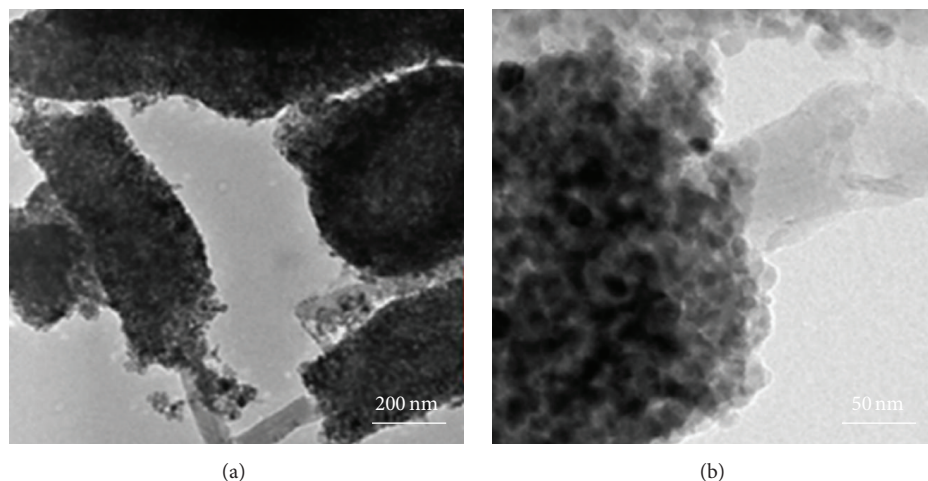


FIGURE 7: (a) and (b) are the TEM images of CNTs@TiO₂ nanocomposite material. Reprinted from [105].

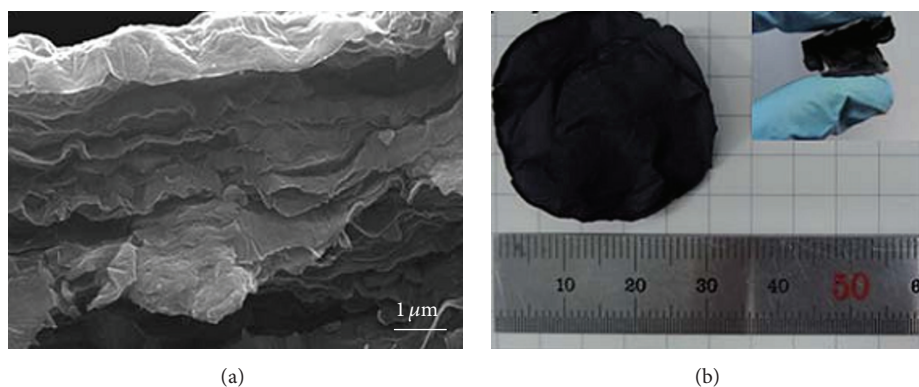


FIGURE 8: (a) and (b) are the SEM and digital images of TiO₂/rGO hybrid films, respectively. Insets display the flexibility of the corresponding films upon bending. Reprinted from [116].

excellent supporting matrix or coating layer to accommodate the volume change during the charge/discharge process. This is crucial for maintaining the good cycling stability [116].

2.3. Combining Metal Oxides with TiO₂. Combining different physical and electrochemical properties of components with TiO₂ and utilizing the respective advantage to increase the capacitance are a feasible method, such as using high conductive materials (conducting polymers) [117, 118], increasing the surface area (carbon nanotubes) [104, 105], and using high performance redox-active transition metal oxides (MnO₂) [119]. Among the above materials, metal oxide coatings can efficiently improve the capacitive performance of the materials through intruding synergistic effects into an electrode system, such as in SnO_x@TiO₂ core-shell composites, due to the nearly zero volume change of TiO₂ in insertion of Li⁺ ions process, making it suitable as a backbone or protective layer for SnO_x to restrain the pulverization and achieve an excellent high rate cycling ability and good cycling stability [120–123]. Recently, synergistic TiO₂-MoO₃ core-shell nanowire arrays were prepared via a facile hydrothermal growth of ordered TiO₂ nanowires followed by a subsequent controllable electrodeposition of nano-MoO₃. The composites exhibited high

gravimetric capacity, good rate performance, and cycling stability. Figure 9 is the SEM images of the pristine TiO₂ nanowire array and optimized TiO₂-MoO₃ hybrid array anode with different magnifications. The strong synergistic effect existing in this design can be summarized as follows: (1) nearly negligible lattice changes during Li ion insertion/extraction, which is crucial to maintain excellent cycling stability. (2) The electrodeposited MoO₃ shell provides both reversible large capacity and good electrical conductivity for its nanosize effect and intrinsic characteristics. (3) The TiO₂ nanowire array can provide direct electron transport pathway between active material and current collector; Li ions can easily intercalate into the composites, manifesting an excellent rate capability and a significantly improved cycling performance [124]. Other transition metal oxides coating TiO₂ composites were also deeply investigated, such as TiO₂-V₂O₅, TiO₂-CoO, and TiO₂-SnO₂ [125–128].

2.4. Doping with Ion or Atom Dopants. For the low electrical conductivity and ion diffusivity of TiO₂, doping with appropriate ions or atoms is advantageous since this method can improve the intrinsic nature of TiO₂ by adjusting its electronic structure, increase the internal surface area and

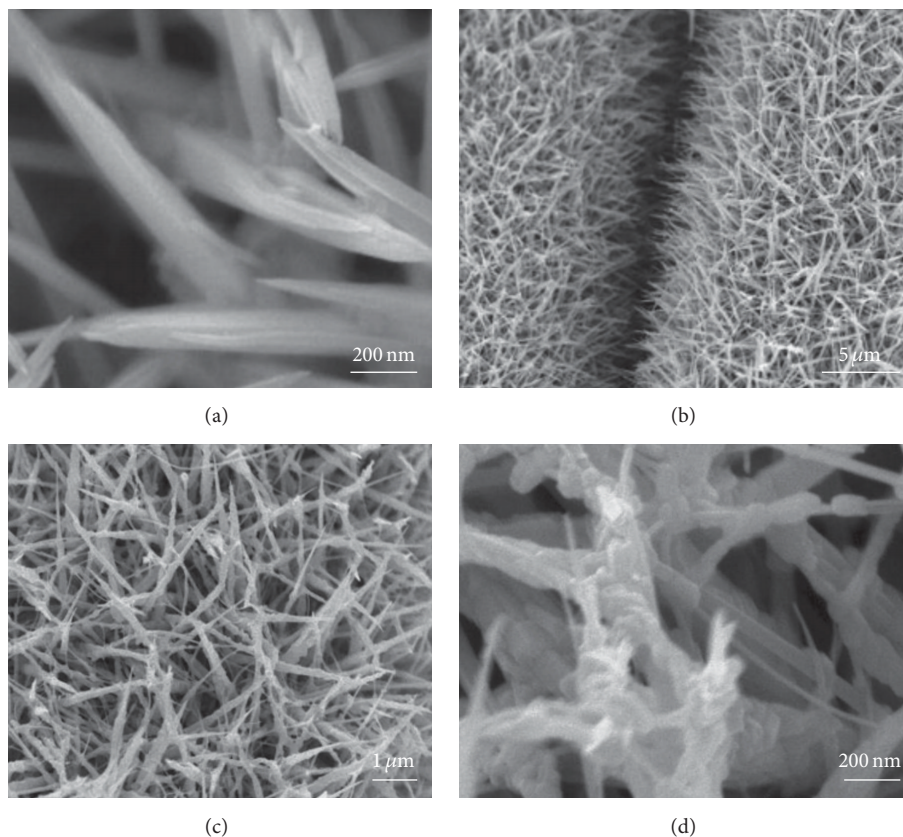


FIGURE 9: (a) SEM images of the pristine TiO_2 nanowire array. (b)–(d) SEM images of the optimized TiO_2 - MoO_3 hybrid array anode with different magnification. Reprinted from [124].

electrical conductivity, and form more open channels and active sites for Li ion transport via the expanding interplanar spacing of TiO_2 lattices [129, 130]. The reported dopants include Fe^{3+} [131], Ti^{3+} [132], Sn^{4+} [133], B [134, 135], and N [136], all of which show beneficial effect on increasing the electrical conductivity more or less.

2.4.1. Ion Dopants. Doping Ti^{3+} in the TiO_2 structure can provide conduction band electrons and undoubtedly improves its conductivity, which also helps to increase the reversible capacity. Ren et al. presented a simple and controllable method to prepare the Ti^{3+} doped TiO_2 by a solvothermal process at lower temperature. The doped TiO_2 nanoparticles showed much enhanced electrochemical performance in reversible capacity, rate performance, and stability comparing with the pure TiO_2 [132]. This is because Ti^{3+} doping can increase the electrical conductivity of TiO_2 . Liu et al. synthesized Ti^{3+} doped TiO_2 nanotube arrays which also exhibited excellent lithium ion intercalation performance with an initial discharge capacity of 101 mA h g^{-1} at a high current density of 10 A g^{-1} [137]. The much improved lithium ion intercalation properties were attributed to the easy phase transition promoted by the surface defects, that is, Ti-C, Ti^{3+} , and O^{2-} vacancies, which could serve as nucleation centers. In addition, the rate performance was also improved due to the enhanced electrical conductivity. Sn^{4+} , Fe^{3+} , and

other metal ions were also investigated as dopants to improve the electrochemical performance [133, 138]. Kyeremateng and coworkers reported that the Sn doped TiO_2 nanotubes delivered much higher capacity values compared to simple TiO_2 nanotubes. The outstanding electrochemical behaviour is proposed to be related to the enhanced lithium diffusivity evidenced with Cottrell plots (Figure 10) and the rutile-type structure imparted with the Sn doping. The results showed that lithium ion insertion into Sn doped TiO_2 is about 40 times faster than into undoped TiO_2 [133].

2.4.2. Atom Dopants. Atoms doping is also a useful technique to increase the internal surface area and electrical conductivity of anode materials. For example, boron (B) and nitrogen (N) doping had been proven to be an effective strategy for improving the electrochemical performance of carbon materials [139–143]. For example, B doped graphite has a larger lattice constant value, a_0 , and a smaller d_{002} distance than ideal graphite, due to replacement of the carbon atoms with boron [144], leading to increases in both the crystallinity and electronic property of carbon as a Li-host material. Jeong et al. synthesized B doped TiO_2 materials through a simple one-pot process. The doped sample containing a relatively large amount of B possesses cylindrical pores that are favorable for lithium ion transfer, leading to the highest diffusion coefficient. Consequently, the doped anodes exhibit significantly improved cyclic capacities compared to the

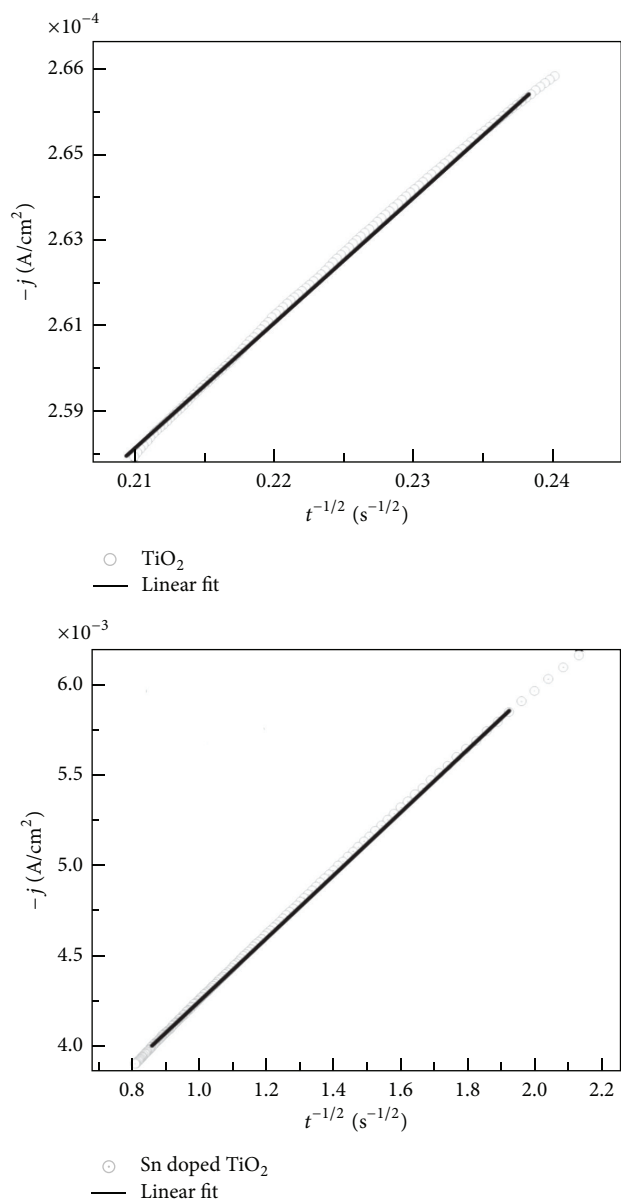


FIGURE 10: Cottrell plots for the determination of Li^+ diffusion coefficients in TiO_2 and Sn doped TiO_2 . Reprinted from [133].

nondoped TiO_2 sample [134]. Furthermore, nitrogen doping has been proven to be an effective strategy for improving the capacity of TiO_2 . This is because nitrogen doping can improve the electric conductivity as well as the ionic conductivity; after introducing the N atoms, the distortion of Ti-O lattice can affect the electrochemical reactions on the interfaces between electrodes and the electrolyte, as well as lithium ion diffusion in the Ti-O lattice [68, 145–147].

3. Conclusions and Outlook

In summary, this review showed the amount of research efforts towards the development and improvement of TiO_2 -based anode materials for LIBs. Several elegant strategies

aiming to boost the electrochemical performance and promote the practical application of TiO_2 have offered, including fabrication of nanostructures with different morphologies and sizes, modification by various coating materials (carbon materials and metal oxides), elements doping. The unique design allows achieving high lithium storage and good cycling stability based on the high lithium ion flux at the electrode/electrolyte interface, low internal resistance, short paths for fast lithium ion diffusion, and low volume change during Li ion insertion/desertions process. When combining these exquisite features together, it is possible for maximizing their electrochemical advantages to meet the present energy demands.

Firstly, the performance of TiO_2 depends strongly on its particle size and morphology. Therefore, different structures of TiO_2 are explored to improve the electrochemical performance of TiO_2 . In a second category, combining TiO_2 with carbonaceous materials such as active carbon, CNTs, and graphene, the composite anode materials can obtain moderate conductivity, large surface area, good chemical stability and mechanical property. In the third, metal oxides such as Fe_2O_3 , SnO_2 , and MnO_2 can provide larger capacities and high energy density compared to pure TiO_2 , which had been combined to improve the overall anode performance. Fourthly, for the low electrical conductivity and ion diffusivity of TiO_2 , doping with appropriate ions or atoms is advantageous since this method can improve the intrinsic nature of TiO_2 by adjusting its electronic structure and forming more open channels and active sites for Li ion transport via the expanding interplanar spacing of TiO_2 lattices.

Finally, from this short review, we can conclude that high energy density, high cycle life, and high efficiency battery will still be the mainstream in the future growth of lithium batteries. In order to utilize the TiO_2 -based materials as effective anodes in commercial LIBs, interdisciplinary effort in this area is however required.

Although considerable advances have been achieved in improving the Li ion storage performance of TiO_2 , several fundamental issues are still needed to be solved. For example, nanomaterials usually show large surface area, which leads to more significant side reactions and results in low coulombic efficiency. Besides, nanopowder has lower density compared to the block material, which would reduce the volumetric energy density of battery. The following two possible strategies may be helpful to solve the abovementioned problem: (1) adopting surface modification or coating to reduce unnecessary side reactions; (2) designing hierarchical structures to enhance the tap density of anode materials.

Conflict of Interests

The authors declare that there is no conflict of interests regarding the publication of this paper.

Acknowledgments

This work was financially supported by Start-Up Foundation of Jiangsu University (15JJDG144), the National Natural

Science Foundation of China (no. 51402262), the 521 Talent Project of Zhejiang Sci-Tech University, and Science Foundation of Zhejiang Sci-Tech University (ZSTU) under Grant no. 13012143-Y.

References

- [1] Z. Yang, D. Choi, S. Kerisit et al., "Nanostructures and lithium electrochemical reactivity of lithium titanites and titanium oxides: a review," *Journal of Power Sources*, vol. 192, no. 2, pp. 588–598, 2009.
- [2] L. Jabbour, R. Bongiovanni, D. Chaussy, C. Gerbaldi, and D. Beneventi, "Cellulose-based Li-ion batteries: a review," *Cellulose*, vol. 20, no. 4, pp. 1523–1545, 2013.
- [3] P. Xiong, L. Peng, D. Chen, Y. Zhao, X. Wang, and G. Yu, "Two-dimensional nanosheets based Li-ion full batteries with high rate capability and flexibility," *Nano Energy*, vol. 12, pp. 816–823, 2015.
- [4] D. Ma, Z. Cao, and A. Hu, "Si-based anode materials for Li-ion batteries: a mini review," *Nano-Micro Letters*, vol. 6, no. 4, pp. 347–358, 2014.
- [5] A. Yoshino, "The birth of the lithium-ion battery," *Angewandte Chemie—International Edition*, vol. 51, no. 24, pp. 5798–5800, 2012.
- [6] L. Xia, Y. Xia, and Z. Liu, "Thiophene derivatives as novel functional additives for high-voltage LiCoO₂ operations in lithium ion batteries," *Electrochimica Acta*, vol. 151, pp. 429–436, 2015.
- [7] S. Muto, K. Tatsumi, Y. Kojima et al., "Effect of Mg-doping on the degradation of LiNiO₂-based cathode materials by combined spectroscopic methods," *Journal of Power Sources*, vol. 205, pp. 449–455, 2012.
- [8] H. Ji, G. Yang, X. Miao, and A. Hong, "Efficient microwave hydrothermal synthesis of nanocrystalline orthorhombic LiMnO₂ cathodes for lithium batteries," *Electrochimica Acta*, vol. 55, no. 9, pp. 3392–3397, 2010.
- [9] X. Yin, K. Huang, S. Liu, H. Wang, and H. Wang, "Preparation and characterization of Na-doped LiFePO₄/C composites as cathode materials for lithium-ion batteries," *Journal of Power Sources*, vol. 195, no. 13, pp. 4308–4312, 2010.
- [10] T. Doi, S. Yatomi, T. Kida, S. Okada, and J.-I. Yamaki, "Liquid-phase synthesis of uniformly nanosized LiMnPO₄ particles and their electrochemical properties for lithium-ion batteries," *Crystal Growth & Design*, vol. 9, no. 12, pp. 4990–4992, 2009.
- [11] S. Goriparti, E. Miele, F. De Angelis, E. Di Fabrizio, R. P. Zaccaria, and C. Capiglia, "Review on recent progress of nanostructured anode materials for Li-ion batteries," *Journal of Power Sources*, vol. 257, pp. 421–443, 2014.
- [12] L. Bai, F. Fang, Y. Zhao et al., "A sandwich structure of mesoporous anatase TiO₂ sheets and reduced graphene oxide and its application as lithium-ion battery electrodes," *RSC Advances*, vol. 4, no. 81, pp. 43039–43046, 2014.
- [13] N. Nitta, F. Wu, J. T. Lee, and G. Yushin, "Li-ion battery materials: present and future," *Materials Today*, vol. 18, no. 5, pp. 252–264, 2015.
- [14] X. Zheng and J. Li, "A review of research on hematite as anode material for lithium-ion batteries," *Ionics*, vol. 20, no. 12, pp. 1651–1663, 2014.
- [15] V. J. Babu, S. Vempati, T. Uyar, and S. Ramakrishna, "Review of one-dimensional and two-dimensional nanostructured materials for hydrogen generation," *Physical Chemistry Chemical Physics*, vol. 17, no. 5, pp. 2960–2986, 2015.
- [16] X. Li, Y. Zhang, T. Li, Q. Zhong, H. Li, and J. Huang, "Graphene nanoscrolls encapsulated TiO₂ (B) nanowires for lithium storage," *Journal of Power Sources*, vol. 268, pp. 372–378, 2014.
- [17] J. Jin, S.-Z. Huang, J. Liu et al., "Design of new anode materials based on hierarchical, three dimensional ordered macroporous TiO₂ for high performance lithium ion batteries," *Journal of Materials Chemistry A*, vol. 2, no. 25, pp. 9699–9708, 2014.
- [18] W. Wei, G. Oltean, C.-W. Tai, K. Edström, F. Björefors, and L. Nyholm, "High energy and power density TiO₂ nanotube electrodes for 3D Li-ion microbatteries," *Journal of Materials Chemistry A*, vol. 1, no. 28, pp. 8160–8169, 2013.
- [19] V. Aravindan, Y. Lee, R. Yazami, and S. Madhavi, "TiO₂ polymorphs in 'rocking-chair' Li-ion batteries," *Materials Today*, vol. 18, no. 6, pp. 345–351, 2015.
- [20] P. Bottke, Y. Ren, I. Hanzu, P. G. Bruce, and M. Wilkening, "Li ion dynamics in TiO₂ anode materials with an ordered hierarchical pore structure—insights from *ex situ* NMR," *Physical Chemistry Chemical Physics*, vol. 16, no. 5, pp. 1894–1901, 2014.
- [21] D. Yuan, W. Yang, J. Ni, and L. Gao, "Sandwich structured MoO₂@TiO₂@CNT nanocomposites with high-rate performance for lithium ion batteries," *Electrochimica Acta*, vol. 163, pp. 57–63, 2015.
- [22] C. Yang, Z. Wang, T. Lin et al., "Core-shell nanostructured 'black' rutile titania as excellent catalyst for hydrogen production enhanced by sulfur doping," *Journal of the American Chemical Society*, vol. 135, no. 47, pp. 17831–17838, 2013.
- [23] J. S. Chen, H. Liu, S. Z. Qiao, and X. W. Lou, "Carbon-supported ultra-thin anatase TiO₂ nanosheets for fast reversible lithium storage," *Journal of Materials Chemistry*, vol. 21, no. 15, pp. 5687–5692, 2011.
- [24] J. S. Chen and X. W. Lou, "Anatase TiO₂ nanosheet: an ideal host structure for fast and efficient lithium insertion/extraction," *Electrochemistry Communications*, vol. 11, no. 12, pp. 2332–2335, 2009.
- [25] T.-D. Nguyen-Phan, V. H. Pham, H. Kweon et al., "Uniform distribution of TiO₂ nanocrystals on reduced graphene oxide sheets by the chelating ligands," *Journal of Colloid and Interface Science*, vol. 367, no. 1, pp. 139–147, 2012.
- [26] J. S. Chen and X. W. Lou, "Unusual rutile TiO₂ nanosheets with exposed (001) facets," *Chemical Science*, vol. 2, no. 11, pp. 2219–2223, 2011.
- [27] H. Huang, J. Fang, Y. Xia et al., "Construction of sheet-belt hybrid nanostructures from one-dimensional mesoporous TiO₂(B) nanobelts and graphene sheets for advanced lithium-ion batteries," *Journal of Materials Chemistry A*, vol. 1, no. 7, pp. 2495–2500, 2013.
- [28] S. Ding, J. S. Chen, Z. Wang et al., "TiO₂ hollow spheres with large amount of exposed (001) facets for fast reversible lithium storage," *Journal of Materials Chemistry*, vol. 21, no. 6, pp. 1677–1680, 2011.
- [29] F. Wu, Z. Wang, X. Li, and H. Guo, "Simple preparation of petal-like TiO₂ nanosheets as anode materials for lithium-ion batteries," *Ceramics International*, vol. 40, no. 10, pp. 16805–16810, 2014.
- [30] J. Liu, J. S. Chen, X. Wei, X. W. Lou, and X.-W. Liu, "Sandwich-like, stacked ultrathin titanate nanosheets for ultrafast lithium storage," *Advanced Materials*, vol. 23, no. 8, pp. 998–1002, 2011.

- [31] J. Tian, Z. Zhao, A. Kumar, R. I. Boughton, and H. Liu, "Recent progress in design, synthesis, and applications of one-dimensional TiO₂ nanostructured surface heterostructures: a review," *Chemical Society Reviews*, vol. 43, no. 20, pp. 6920–6937, 2014.
- [32] B. Yuan and L. Cademartiri, "Flexible one-dimensional nanostructures: a review," *Journal of Materials Science & Technology*, vol. 31, no. 6, pp. 607–615, 2015.
- [33] X. Feng, K. Shankar, O. K. Varghese, M. Paulose, T. J. Latempa, and C. A. Grimes, "Vertically aligned single crystal TiO₂ nanowire arrays grown directly on transparent conducting oxide coated glass: synthesis details and applications," *Nano Letters*, vol. 8, no. 11, pp. 3781–3786, 2008.
- [34] Q. Tian, Z. Zhang, L. Yang, and S.-I. Hirano, "Facile fabrication of one-dimensional mesoporous titanium dioxide composed of nanocrystals for lithium storage," *Electrochimica Acta*, vol. 138, pp. 155–162, 2014.
- [35] Y. Tang, Z. Liu, X. Lü, B. Wang, and F. Huang, "TiO₂ nanotubes grown on graphene sheets as advanced anode materials for high rate lithium ion batteries," *RSC Advances*, vol. 4, no. 68, pp. 36372–36376, 2014.
- [36] S. Peng, L. Li, Y. Hu et al., "Fabrication of spinel one-dimensional architectures by single-spinneret electrospinning for energy storage applications," *ACS Nano*, vol. 9, no. 2, pp. 1945–1954, 2015.
- [37] Y. Tan, Q. Gao, C. Yang, K. Yang, W. Tian, and L. Zhu, "One-dimensional porous nanofibers of Co₃O₄ on the carbon matrix from human hair with superior lithium ion storage performance," *Scientific Reports*, vol. 5, Article ID 12382, 2015.
- [38] J. L. Xie, C. X. Guo, and C. M. Li, "Construction of one-dimensional nanostructures on graphene for efficient energy conversion and storage," *Energy & Environmental Science*, vol. 7, no. 8, pp. 2559–2579, 2014.
- [39] P. Tammawat and N. Meethong, "Synthesis and characterization of stable and binder-free electrodes of TiO₂ nanofibers for Li-ion batteries," *Journal of Nanomaterials*, vol. 2013, Article ID 413692, 8 pages, 2013.
- [40] A. R. Armstrong, G. Armstrong, J. Canales, and P. G. Bruce, "TiO₂-B nanowires," *Angewandte Chemie—International Edition*, vol. 43, no. 17, pp. 2286–2288, 2004.
- [41] A. R. Armstrong, G. Armstrong, J. Canales, and P. G. Bruce, "TiO₂-B nanowires as negative electrodes for rechargeable lithium batteries," *Journal of Power Sources*, vol. 146, no. 1-2, pp. 501–506, 2005.
- [42] A. R. Armstrong, G. Armstrong, J. Canales, R. García, and P. G. Bruce, "Lithium-ion intercalation into TiO₂-B nanowires," *Advanced Materials*, vol. 17, no. 7, pp. 862–865, 2005.
- [43] H. Wang, C. Guan, X. Wang, and H. J. Fan, "A high energy and power Li-ion capacitor based on a TiO₂ nanobelt array anode and a graphene hydrogel cathode," *Small*, vol. 11, no. 12, pp. 1470–1477, 2015.
- [44] H.-R. Xia, J. Li, C. Peng, W.-T. Sun, L.-W. Li, and L.-M. Peng, "Floating growth of large-scale freestanding TiO₂ nanorod films at the gas-liquid interface for additive-free li-ion battery applications," *ACS Applied Materials & Interfaces*, vol. 6, no. 20, pp. 17376–17383, 2014.
- [45] T. Hu, X. Sun, H. Sun et al., "Flexible free-standing graphene-TiO₂ hybrid paper for use as lithium ion battery anode materials," *Carbon*, vol. 51, no. 1, pp. 322–326, 2013.
- [46] C. Wang, D. Li, C. O. Too, and G. G. Wallace, "Electrochemical properties of graphene paper electrodes used in lithium batteries," *Chemistry of Materials*, vol. 21, no. 13, pp. 2604–2606, 2009.
- [47] Y. Liu, W. Wang, L. Gu et al., "Flexible CuO nanosheets/reduced-graphene oxide composite paper: binder-free anode for high-performance lithium-ion batteries," *ACS Applied Materials & Interfaces*, vol. 5, no. 19, pp. 9850–9855, 2013.
- [48] Y. Liu, W. Wang, H. Huang, L. Gu, Y. Wang, and X. Peng, "The highly enhanced performance of lamellar WS₂ nanosheet electrodes upon intercalation of single-walled carbon nanotubes for supercapacitors and lithium ions batteries," *Chemical Communications*, vol. 50, no. 34, pp. 4485–4488, 2014.
- [49] L. Ma, X. Zhou, L. Xu, X. Xu, L. Zhang, and W. Chen, "Chitosan-assisted fabrication of ultrathin MoS₂/graphene heterostructures for Li-ion battery with excellent electrochemical performance," *Electrochimica Acta*, vol. 167, pp. 39–47, 2015.
- [50] T. Zhang, F. Zhang, L. Zhang et al., "High energy density Li-ion capacitor assembled with all graphene-based electrodes," *Carbon*, vol. 92, pp. 106–118, 2015.
- [51] H. Liu, D. Su, G. Wang, and S. Z. Qiao, "An ordered mesoporous WS₂ anode material with superior electrochemical performance for lithium ion batteries," *Journal of Materials Chemistry*, vol. 22, no. 34, pp. 17437–17440, 2012.
- [52] H. Hwang, H. Kim, and J. Cho, "MoS₂ nanoplates consisting of disordered graphene-like layers for high rate lithium battery anode materials," *Nano Letters*, vol. 11, no. 11, pp. 4826–4830, 2011.
- [53] A. N. Enyashin and A. L. Ivanovskii, "Structural and electronic properties and stability of MX₂ MX₂ functionalized by methoxy groups," *Journal of Physical Chemistry C*, vol. 117, no. 26, pp. 13637–13643, 2013.
- [54] J. Come, M. Naguib, P. Rozier et al., "A non-aqueous asymmetric cell with a Ti₂C-based two-dimensional negative electrode," *Journal of the Electrochemical Society*, vol. 159, no. 8, pp. A1368–A1373, 2012.
- [55] Y. Liu, W. Wang, Y. Ying, Y. Wang, and X. Peng, "Binder-free layered Ti₃C₂/CNTs nanocomposite anodes with enhanced capacity and long-cycle life for lithium-ion batteries," *Dalton Transactions*, vol. 44, no. 16, pp. 7123–7126, 2015.
- [56] C.-L. Liu, Y. Wang, C. Zhang, X.-S. Li, and W.-S. Dong, "In situ synthesis of α -MoO₃/graphene composites as anode materials for lithium ion battery," *Materials Chemistry and Physics*, vol. 143, no. 3, pp. 1111–1118, 2014.
- [57] Y. Qian, A. Vu, W. Smyrl, and A. Stein, "Facile preparation and electrochemical properties of V₂O₅-graphene composite films as free-standing cathodes for rechargeable lithium batteries," *Journal of the Electrochemical Society*, vol. 159, no. 8, pp. A1135–A1140, 2012.
- [58] K. Zhu, X. Liu, J. Du et al., "In situ synthesis of mesoporous single-grain layer anatase TiO₂ nanosheets without additives via a mild and simple process for a long-term Li-ion battery," *Journal of Materials Chemistry A*, vol. 3, no. 12, pp. 6455–6463, 2015.
- [59] X. Lü, F. Huang, J. Wu, S. Ding, and F. Xu, "Intelligent hydrated-sulfate template assisted preparation of nanoporous TiO₂ spheres and their visible-light application," *ACS Applied Materials & Interfaces*, vol. 3, no. 2, pp. 566–572, 2011.
- [60] X. Lü, S. Ding, Y. Xie, and F. Huang, "Non-aqueous preparation of high-crystallinity hierarchical TiO₂ hollow spheres with excellent photocatalytic efficiency," *European Journal of Inorganic Chemistry*, no. 18, pp. 2879–2883, 2011.
- [61] S. Ding, T. Lin, Y. Wang, X. Lü, and F. Huang, "New facile synthesis of TiO₂ hollow sphere with an opening hole and its enhanced rate performance in lithium-ion batteries," *New Journal of Chemistry*, vol. 37, no. 3, pp. 784–789, 2013.

- [62] S. Ding, Y. Wang, Z. Hong, X. Lü, D. Wan, and F. Huang, "Biomolecule-assisted route to prepare titania mesoporous hollow structures," *Chemistry—A European Journal*, vol. 17, no. 41, pp. 11535–11541, 2011.
- [63] G. Grinbom, D. Dureau, G. Gershinsky, L. Monconduit, and D. Zitoun, "Silicon/hollow gamma-Fe₂O₃ nanoparticles as efficient anodes for Li-ion batteries," *Chemistry of Materials*, vol. 27, no. 7, pp. 2703–2710, 2015.
- [64] X. Wang, Y. Wang, L. Yang, K. Wang, X. Lou, and B. Cai, "Template-free synthesis of homogeneous yolk-shell TiO₂ hierarchical microspheres for high performance lithium ion batteries," *Journal of Power Sources*, vol. 262, pp. 72–78, 2014.
- [65] W. Wei, L.-X. Song, and L. Guo, "SnO₂ hollow nanospheres assembled by single layer nanocrystals as anode material for high performance Li ion batteries," *Chinese Chemical Letters*, vol. 26, no. 1, pp. 124–128, 2015.
- [66] S. Zhang, W. He, X. Zhang, and X. Yang, "Rational design of carbon-coated hollow MnO nanotubes for Li-ion batteries," *Journal of Materials Science: Materials in Electronics*, vol. 26, no. 4, pp. 2189–2197, 2015.
- [67] Y.-C. Chang, C.-W. Peng, P.-C. Chen, C.-Y. Lee, and H.-T. Chiu, "Bio-ingredient assisted formation of porous TiO₂ for Li-ion battery electrodes," *RSC Advances*, vol. 5, no. 44, pp. 34949–34955, 2015.
- [68] G. Hasegawa, T. Sato, K. Kanamori, K. Nakanishi, and T. Abe, "Synthesis and electrochemical performance of hierarchically porous N-doped TiO₂ for Li-ion batteries," *New Journal of Chemistry*, vol. 38, no. 4, pp. 1380–1384, 2014.
- [69] H. Ming, Y. Yan, J. Ming et al., "Porous TiO₂ nanoribbons and TiO₂ nanoribbon/carbon dot composites for enhanced Li-ion storage," *RSC Advances*, vol. 4, no. 25, pp. 12971–12976, 2014.
- [70] H.-W. Shim, D. K. Lee, I.-S. Cho, K. S. Hong, and D.-W. Kim, "Facile hydrothermal synthesis of porous TiO₂ nanowire electrodes with high-rate capability for Li ion batteries," *Nanotechnology*, vol. 21, no. 25, Article ID 255706, 2010.
- [71] F. Di Lupo, A. Tuel, V. Mendez et al., "Mesoporous TiO₂ nanocrystals produced by a fast hydrolytic process as high-rate long-lasting Li-ion battery anodes," *Acta Materialia*, vol. 69, pp. 60–67, 2014.
- [72] S. Casino, F. Di Lupo, C. Francia, A. Tuel, S. Bodoardo, and C. Gerbaldi, "Surfactant-assisted sol gel preparation of high-surface area mesoporous TiO₂ nanocrystalline Li-ion battery anodes," *Journal of Alloys and Compounds*, vol. 594, pp. 114–121, 2014.
- [73] G. Zhang, H. B. Wu, T. Song, U. Paik, and X. W. Lou, "TiO₂ hollow spheres composed of highly crystalline nanocrystals exhibit superior lithium storage properties," *Angewandte Chemie—International Edition*, vol. 53, no. 46, pp. 12590–12593, 2014.
- [74] X.-Y. Yu, H. B. Wu, L. Yu, F.-X. Ma, and X. W. D. Lou, "Rutile TiO₂ submicroboxes with superior lithium storage properties," *Angewandte Chemie—International Edition*, vol. 54, no. 13, pp. 4001–4004, 2015.
- [75] S. Li and X. Wang, "Micro Li-ion capacitor with activated carbon/graphite configuration for energy storage," *Journal of Power Sources*, vol. 282, pp. 394–400, 2015.
- [76] C. Yuan, L. Zhang, S. Zhu, H. Cao, J. Lin, and L. Hou, "Heterostructured core-shell ZnMn₂O₄ nanosheets@carbon nanotubes' coaxial nanocables: a competitive anode towards high-performance Li-ion batteries," *Nanotechnology*, vol. 26, no. 14, Article ID 145401, 2015.
- [77] J.-M. Feng, L. Dong, Y. Han, X.-F. Li, and D.-J. Li, "Efficient exfoliation N-doped graphene from N-containing bamboo-like carbon nanotubes for anode materials of Li-ion battery and Na-ion battery," *Applied Physics A: Materials Science & Processing*, vol. 120, no. 2, pp. 471–478, 2015.
- [78] R. Jin, G. Li, Z. Zhang, L. Yang, and G. Chen, "Carbon coated flower like Bi₂S₃ grown on nickel foam as binder-free electrodes for electrochemical hydrogen and Li-ion storage capacities," *Electrochimica Acta*, vol. 173, pp. 458–464, 2015.
- [79] X. Lu, F. Yang, Y. Wang, X. Geng, and P. Xiao, "The influence of graphene/carbon mass ratio on microstructure and electrochemical behavior in the graphene-SnO₂-carbon composite as anodes for Li-ion batteries," *Journal of Alloys and Compounds*, vol. 636, pp. 202–210, 2015.
- [80] C. Zhang, H. Song, C. Liu et al., "Fast and reversible Li ion insertion in carbon-encapsulated Li₃VO₄ as anode for lithium-ion battery," *Advanced Functional Materials*, vol. 25, no. 23, pp. 3497–3504, 2015.
- [81] S. Fang, L. Shen, Z. Tong, H. Zheng, F. Zhang, and X. Zhang, "Si nanoparticles encapsulated in elastic hollow carbon fibres for Li-ion battery anodes with high structural stability," *Nanoscale*, vol. 7, no. 16, pp. 7409–7414, 2015.
- [82] X. Lv, J. Deng, J. Wang, J. Zhong, and X. Sun, "Carbon-coated alpha-Fe₂O₃ nanostructures for efficient anode of Li-ion battery," *Journal of Materials Chemistry A*, vol. 3, no. 9, pp. 5183–5188, 2015.
- [83] S. Wang, C. Xiao, Y. Xing, H. Xu, and S. Zhang, "Carbon nanofibers/nanosheets hybrid derived from cornstalks as a sustainable anode for Li-ion batteries," *Journal of Materials Chemistry A*, vol. 3, no. 13, pp. 6742–6746, 2015.
- [84] S. Wang, Y. Xing, C. Xiao, X. Wei, H. Xu, and S. Zhang, "Hollow carbon-shell/carbon-nanorod arrays for high performance Li-ion batteries and supercapacitors," *RSC Advances*, vol. 5, no. 11, pp. 7959–7963, 2015.
- [85] M. Ara, V. R. Chitturi, S. O. Salley, and K. Y. S. Ng, "Nitrogen-doped carbon-coated Sn_xO_y (x=1 and y=0 and 2) nanoparticles for rechargeable Li-ion batteries," *Electrochimica Acta*, vol. 161, pp. 269–278, 2015.
- [86] X. H. Wang, C. Guan, L. M. Sun, R. A. Susantyoko, H. J. Fan, and Q. Zhang, "Highly stable and flexible Li-ion battery anodes based on TiO₂ coated 3D carbon nanostructures," *Journal of Materials Chemistry A*, vol. 3, no. 30, pp. 15394–15398, 2015.
- [87] S. S. Tang, G. R. Li, B. H. Liu, and Z. P. Li, "Carbon-coated titanium dioxide micro-bowls as an anode material for Li-ion batteries," *Electrochimica Acta*, vol. 125, pp. 199–205, 2014.
- [88] G. Lu, S. Qiu, H. Lv et al., "Li-ion storage performance of MnO nanoparticles coated with nitrogen-doped carbon derived from different carbon sources," *Electrochimica Acta*, vol. 146, pp. 249–256, 2014.
- [89] T. Xia, W. Zhang, Z. Wang et al., "Amorphous carbon-coated TiO₂ nanocrystals for improved lithium-ion battery and photocatalytic performance," *Nano Energy*, vol. 6, pp. 109–118, 2014.
- [90] J. Brumbarov, J. P. Vivek, S. Leonardi, C. Valero-Vidal, E. Portenkirchner, and J. Kunze-Liebhäuser, "Oxygen deficient, carbon coated self-organized TiO₂ nanotubes as anode material for Li-ion intercalation," *Journal of Materials Chemistry A*, vol. 3, no. 32, pp. 16469–16477, 2015.
- [91] Y. Fu, H. Ming, Q. Zhou, L. Jin, X. Li, and J. Zheng, "Nitrogen-doped carbon coating inside porous TiO₂ using small nitrogen-containing molecules for improving performance of lithium-ion batteries," *Electrochimica Acta*, vol. 134, pp. 478–485, 2014.
- [92] J. A. Puértolas and S. M. Kurtz, "Evaluation of carbon nanotubes and graphene as reinforcements for UHMWPE-based

- composites in arthroplastic applications: a review,” *Journal of the Mechanical Behavior of Biomedical Materials*, vol. 39, pp. 129–145, 2014.
- [93] Q. Wang and B. Arash, “A review on applications of carbon nanotubes and graphenes as nano-resonator sensors,” *Computational Materials Science*, vol. 82, pp. 350–360, 2014.
- [94] C. Kang, R. Baskaran, J. Hwang, B.-C. Ku, and W. Choi, “Large scale patternable 3-dimensional carbon nanotube-graphene structure for flexible Li-ion battery,” *Carbon*, vol. 68, pp. 493–500, 2014.
- [95] H. Liu, “Carbon nanotubes anchored with SnO₂ nanosheets as anode for enhanced Li-ion storage,” *Journal of Materials Science: Materials in Electronics*, vol. 25, no. 8, pp. 3353–3357, 2014.
- [96] H. Pan, “Graphitic carbon nitride nanotubes as Li-ion battery materials: a first-principles study,” *The Journal of Physical Chemistry C*, vol. 118, no. 18, pp. 9318–9323, 2014.
- [97] A. Varzi, C. Täubert, M. Wohlfahrt-Mehrens, M. Kreis, and W. Schütz, “Study of multi-walled carbon nanotubes for lithium-ion battery electrodes,” *Journal of Power Sources*, vol. 196, no. 6, pp. 3303–3309, 2011.
- [98] H. Zhang, G. Cao, Z. Wang, Y. Yang, Z. Shi, and Z. Gu, “Carbon nanotube array anodes for high-rate Li-ion batteries,” *Electrochimica Acta*, vol. 55, no. 8, pp. 2873–2877, 2010.
- [99] J. Chen, J. Z. Wang, A. I. Minett et al., “Carbon nanotube network modified carbon fibre paper for Li-ion batteries,” *Energy & Environmental Science*, vol. 2, no. 4, pp. 393–396, 2009.
- [100] A. Antic, V. Barone, and B. D. Fahlman, “Comparison of oxidized carbon nanotubes for Li-ion storage capacity,” *Journal of Applied Electrochemistry*, vol. 45, no. 2, pp. 161–167, 2015.
- [101] J.-C. Kim, I.-S. Hwang, S.-D. Seo, and D.-W. Kim, “Nanocomposite Li-ion battery anodes consisting of multiwalled carbon nanotubes that anchor CoO nanoparticles,” *Materials Letters*, vol. 104, pp. 13–16, 2013.
- [102] J.-C. Kim, I.-S. Hwang, S.-D. Seo et al., “Superior long-term cycling stability of SnO₂ nanoparticle/multiwalled carbon nanotube heterostructured electrodes for Li-ion rechargeable batteries,” *Nanotechnology*, vol. 23, no. 46, Article ID 465402, 2012.
- [103] L. Zhuo, Y. Wu, J. Ming et al., “Facile synthesis of a Co₃O₄-carbon nanotube composite and its superior performance as an anode material for Li-ion batteries,” *Journal of Materials Chemistry A*, vol. 1, no. 4, pp. 1141–1147, 2013.
- [104] P. Acevedo-Peña, M. Haro, M. E. Rincón, J. Bisquert, and G. Garcia-Belmonte, “Facile kinetics of Li-ion intake causes superior rate capability in multiwalled carbon nanotube@TiO₂ nanocomposite battery anodes,” *Journal of Power Sources*, vol. 268, pp. 397–403, 2014.
- [105] Y.-X. Wang, J. Xie, G.-S. Cao, T.-J. Zhu, and X.-B. Zhao, “Electrochemical performance of TiO₂/carbon nanotubes nanocomposite prepared by an in situ route for Li-ion batteries,” *Journal of Materials Research*, vol. 27, no. 2, pp. 417–423, 2012.
- [106] A. W. Anwar, A. Majeed, N. Iqbal et al., “Specific capacitance and cyclic stability of graphene based metal/metal oxide nanocomposites: a review,” *Journal of Materials Science & Technology*, vol. 31, no. 7, pp. 699–707, 2015.
- [107] S. M. Lee, J.-H. Kim, and J.-H. Ahn, “Graphene as a flexible electronic material: mechanical limitations by defect formation and efforts to overcome,” *Materials Today*, vol. 18, no. 6, pp. 336–344, 2015.
- [108] H. Miao, Y. Xue, X. Zhou, and Z. Liu, “Graphene-based oxygen reduction reaction catalysts for metal air batteries,” *Progress in Chemistry*, vol. 27, no. 7, pp. 935–944, 2015.
- [109] H. Wang, X. Yuan, G. Zeng et al., “Three dimensional graphene based materials: synthesis and applications from energy storage and conversion to electrochemical sensor and environmental remediation,” *Advances in Colloid and Interface Science*, vol. 221, pp. 41–59, 2015.
- [110] D. Li, Y. Liu, B. Lin, Y. Sun, H. Yang, and X. Zhang, “Graphene/metal oxide composites as electrode material for supercapacitors,” *Progress in Chemistry*, vol. 27, no. 4, pp. 404–415, 2015.
- [111] M. Mao, J. Hu, and H. Liu, “Graphene-based materials for flexible electrochemical energy storage,” *International Journal of Energy Research*, vol. 39, no. 6, pp. 727–740, 2015.
- [112] Y. Zhao, X. Li, B. Yan, D. Li, S. Lawes, and X. Sun, “Significant impact of 2D graphene nanosheets on large volume change tin-based anodes in lithium-ion batteries: a review,” *Journal of Power Sources*, vol. 274, pp. 869–884, 2015.
- [113] G. Fang, S. Kaneko, W. Liu et al., “Persistent cycle stability of carbon coated Zn-Sn metal oxide/carbon microspheres as highly reversible anode material for lithium-ion batteries,” *Electrochimica Acta*, vol. 111, pp. 627–634, 2013.
- [114] Y. Fang, Y. Lv, R. Che et al., “Two-dimensional mesoporous carbon nanosheets and their derived graphene nanosheets: synthesis and efficient lithium ion storage,” *Journal of the American Chemical Society*, vol. 135, no. 4, pp. 1524–1530, 2013.
- [115] V. Etacheri, J. E. Yourey, and B. M. Bartlett, “Chemically bonded TiO₂-Bronze nanosheet/reduced graphene oxide hybrid for high-power lithium ion batteries,” *ACS Nano*, vol. 8, no. 2, pp. 1491–1499, 2014.
- [116] J. Kim, W.-H. Khoh, B.-H. Wee, and J.-D. Hong, “Fabrication of flexible reduced graphene oxide-TiO₂ freestanding films for supercapacitor application,” *RSC Advances*, vol. 5, no. 13, pp. 9904–9911, 2015.
- [117] H. Aydın and A. Bozkurt, “Nanocomposite polymer electrolytes comprising PVA-graft-PEGME/TiO₂ for Li-ion batteries,” *Journal of Materials Research*, vol. 29, no. 5, pp. 625–632, 2014.
- [118] J. Cao, L. Wang, Y. Shang et al., “Dispersibility of nano-TiO₂ on performance of composite polymer electrolytes for Li-ion batteries,” *Electrochimica Acta*, vol. 111, pp. 674–679, 2013.
- [119] Q. Zhu, H. Hu, G. Li, C. Zhu, and Y. Yu, “TiO₂ nanotube arrays grafted with MnO₂ nanosheets as high-performance anode for lithium ion battery,” *Electrochimica Acta*, vol. 156, pp. 252–260, 2015.
- [120] S. Park, S.-D. Seo, S. Lee et al., “Sb:SnO₂@TiO₂ heteroepitaxial branched nanoarchitectures for Li ion battery electrodes,” *The Journal of Physical Chemistry C*, vol. 116, no. 41, pp. 21717–21726, 2012.
- [121] X. Wu, S. Zhang, L. Wang et al., “Coaxial SnO₂@TiO₂ nanotube hybrids: from robust assembly strategies to potential application in Li⁺ storage,” *Journal of Materials Chemistry*, vol. 22, no. 22, pp. 11151–11158, 2012.
- [122] C. Guan, X. Wang, Q. Zhang, Z. Fan, H. Zhang, and H. J. Fan, “Highly stable and reversible lithium storage in SnO₂ nanowires surface coated with a uniform hollow shell by atomic layer deposition,” *Nano Letters*, vol. 14, no. 8, pp. 4852–4858, 2014.
- [123] J.-H. Jeun, K.-Y. Park, D.-H. Kim et al., “SnO₂@TiO₂ double-shell nanotubes for a lithium ion battery anode with excellent high rate cyclability,” *Nanoscale*, vol. 5, no. 18, pp. 8480–8483, 2013.
- [124] C. Wang, L. Wu, H. Wang, W. Zuo, Y. Li, and J. Liu, “Fabrication and shell optimization of synergistic TiO₂-MoO₃ core-shell nanowire array anode for high energy and power density lithium-ion batteries,” *Advanced Functional Materials*, vol. 25, no. 23, pp. 3524–3533, 2015.

- [125] M. J. Armstrong, D. M. Burke, T. Gabriel et al., "Carbon nanocage supported synthesis of V_2O_5 nanorods and V_2O_5/TiO_2 nanocomposites for Li-ion batteries," *Journal of Materials Chemistry A*, vol. 1, no. 40, pp. 12568–12578, 2013.
- [126] M. Madian, L. Giebeler, M. Klose et al., "Self-organized TiO_2/CoO nanotubes as potential anode materials for lithium ion batteries," *ACS Sustainable Chemistry & Engineering*, vol. 3, no. 5, pp. 909–919, 2015.
- [127] D. Ma, P. Dou, X. Yu et al., "Novel hollow SnO_2 nanosphere@ TiO_2 yolk-shell hierarchical nanospheres as anode material for high-performance lithium-ion batteries," *Materials Letters*, vol. 157, pp. 228–230, 2015.
- [128] C. Chen, S. H. Lee, M. Cho, and Y. Lee, "Core-shell $CuO@TiO_2$ nanorods as a highly stable anode material for lithium-ion batteries," *Materials Letters*, vol. 140, pp. 111–114, 2015.
- [129] X. Lü, W. Yang, Z. Quan et al., "Enhanced electron transport in Nb-doped TiO_2 nanoparticles via pressure-induced phase transitions," *Journal of the American Chemical Society*, vol. 136, no. 1, pp. 419–426, 2014.
- [130] X. Lü, X. Mou, J. Wu et al., "Improved-performance dye-sensitized solar cells using Nb-doped TiO_2 electrodes: efficient electron injection and transfer," *Advanced Functional Materials*, vol. 20, no. 3, pp. 509–515, 2010.
- [131] S. K. Das, M. Gnanavel, M. U. M. Patel, C. Shivakumara, and A. J. Bhattacharyya, "Anomolously high lithium storage in mesoporous nanoparticulate aggregation of Fe^{3+} doped anatase titania," *Journal of the Electrochemical Society*, vol. 158, no. 12, pp. A1290–A1297, 2011.
- [132] Y. Ren, J. Li, and J. Yu, "Enhanced electrochemical performance of TiO_2 by Ti^{3+} doping using a facile solvothermal method as anode materials for lithium-ion batteries," *Electrochimica Acta*, vol. 138, pp. 41–47, 2014.
- [133] N. A. Kyeremateng, F. Vacandio, M.-T. Sougrati et al., "Effect of Sn-doping on the electrochemical behaviour of TiO_2 nanotubes as potential negative electrode materials for 3D Li-ion micro batteries," *Journal of Power Sources*, vol. 224, pp. 269–277, 2013.
- [134] J.-H. Jeong, D.-W. Jung, E. W. Shin, and E.-S. Oh, "Boron-doped TiO_2 anode materials for high-rate lithium ion batteries," *Journal of Alloys and Compounds*, vol. 604, pp. 226–232, 2014.
- [135] H. Tian, F. Xin, X. Tan, and W. Han, "High lithium electroactivity of boron-doped hierarchical rutile submicrosphere TiO_2 ," *Journal of Materials Chemistry A*, vol. 2, no. 27, pp. 10599–10606, 2014.
- [136] Y. Zhang, Q. Fu, Q. Xu et al., "Improved electrochemical performance of nitrogen doped TiO_2 -B nanowires as anode materials for Li-ion batteries," *Nanoscale*, vol. 7, no. 28, pp. 12215–12224, 2015.
- [137] D. Liu, Y. Zhang, P. Xiao et al., " TiO_2 nanotube arrays annealed in CO exhibiting high performance for lithium ion intercalation," *Electrochimica Acta*, vol. 54, no. 27, pp. 6816–6820, 2009.
- [138] V. Gentili, S. Brutti, L. J. Hardwick, A. R. Armstrong, S. Panero, and P. G. Bruce, "Lithium insertion into anatase nanotubes," *Chemistry of Materials*, vol. 24, no. 22, pp. 4468–4476, 2012.
- [139] H. Fujimoto, A. Mabuchi, C. Natarajan, and T. Kasuh, "Properties of graphite prepared from boron-doped pitch as an anode for a rechargeable Li ion battery," *Carbon*, vol. 40, no. 4, pp. 567–574, 2002.
- [140] R. P. Hardikar, D. Das, S. S. Han, K.-R. Lee, and A. K. Singh, "Boron doped defective graphene as a potential anode material for Li-ion batteries," *Physical Chemistry Chemical Physics*, vol. 16, no. 31, pp. 16502–16508, 2014.
- [141] M. Sahoo, K. P. Sreena, B. P. Vinayan, and S. Ramaprabhu, "Green synthesis of boron doped graphene and its application as high performance anode material in Li ion battery," *Materials Research Bulletin*, vol. 61, pp. 383–390, 2015.
- [142] R. Gokhale, V. Aravindan, P. Yadav et al., "Oligomer-salt derived 3D, heavily nitrogen doped, porous carbon for Li-ion hybrid electrochemical capacitors application," *Carbon*, vol. 80, no. 1, pp. 462–471, 2014.
- [143] T. Sharifi, M. Valvo, E. Gracia-Espino, R. Sandström, K. Edström, and T. Wågberg, "Hierarchical self-assembled structures based on nitrogen-doped carbon nanotubes as advanced negative electrodes for Li-ion batteries and 3D microbatteries," *Journal of Power Sources*, vol. 279, pp. 581–592, 2015.
- [144] U. Tanaka, T. Sogabe, H. Sakagoshi, M. Ito, and T. Tojo, "Anode property of boron-doped graphite materials for rechargeable lithium-ion batteries," *Carbon*, vol. 39, no. 6, pp. 931–936, 2001.
- [145] Y. Zhou, Q. Bao, L. A. L. Tang, Y. Zhong, and K. P. Loh, "Hydrothermal dehydration for the 'green' reduction of exfoliated graphene oxide to graphene and demonstration of tunable optical limiting properties," *Chemistry of Materials*, vol. 21, no. 13, pp. 2950–2956, 2009.
- [146] C. D. Joyce, T. McIntyre, S. Simmons et al., "Synthesis and electrochemical evaluation of an amorphous titanium dioxide derived from a solid state precursor," *Journal of Power Sources*, vol. 195, no. 7, pp. 2064–2068, 2010.
- [147] S. Chen, W. Chu, Y. Y. Huang, X. Liu, and D. G. Tong, "Preparation of porous nitrogen-doped titanium dioxide microspheres and a study of their photocatalytic, antibacterial and electrochemical activities," *Materials Research Bulletin*, vol. 47, no. 12, pp. 4514–4521, 2012.

Research Article

Modified Sol-Gel Synthesis of Carbon Nanotubes Supported Titania Composites with Enhanced Visible Light Induced Photocatalytic Activity

Quanjie Wang,¹ Yanqing Wang,^{1,2} Baorong Duan,¹ and Mengmeng Zhang¹

¹Department of Light Industry of Technology and Engineering, College of Chemistry and Chemical Engineering, Yantai University, Yantai 264005, China

²Key Laboratory of Wetland Ecology and Environment, Northeast Institute of Geography and Agro-Ecology, Chinese Academy of Sciences, Changchun 130102, China

Correspondence should be addressed to Quanjie Wang; wangquanjie@126.com and Yanqing Wang; ytever@hotmail.com

Received 28 July 2015; Revised 8 November 2015; Accepted 12 November 2015

Academic Editor: Xujie Lü

Copyright © 2016 Quanjie Wang et al. This is an open access article distributed under the Creative Commons Attribution License, which permits unrestricted use, distribution, and reproduction in any medium, provided the original work is properly cited.

Multiwalled carbon nanotube (MWCNT) enhanced MWCNT/TiO₂ nanocomposites were synthesized by surface coating of carbon nanotube with mixed phase of anatase and rutile TiO₂ through a modified sol-gel approach using tetrabutyl titanate as raw material. The morphological structures and physicochemical properties of the nanocomposites were characterized by FT-IR, XRD, DTA-TG, TEM, and UV-Vis spectra. The results show that TiO₂ nanoparticles with size of around 15 nm are closely attached on the sidewall of MWCNT. The nanocomposites possess good absorption properties not only in the ultraviolet but also in the visible light region. Under irradiation of ultraviolet lamp, the prepared composites have the highest photodegradation efficiency of 83% within 4 hours towards the degradation of Methyl Orange (MO) aqueous solution. The results indicate that the carbon nanotubes supported TiO₂ nanocomposites exhibit high photocatalytic activity and stability, showing great potentials in the treatment of wastewater.

1. Introduction

Treatment of the industrial wastewater, especially the organic pollutants which are difficult to be biochemically degraded, is currently viewed as an active research area [1, 2]. Titanium dioxide (TiO₂) is an environmental-friendly photocatalyst material due to its high catalytic activity, thermal stability, strong oxidizing power, and nontoxic, low cost, and other unique advantages [3–5]. However, its photoefficiency is not high enough and the speed of ultraviolet photoresponse is not satisfactory [6, 7]. On the other hand, there is a measurable reduction in the photocatalytic activity for the recycled use of the photocatalysts. The disadvantage of TiO₂ semiconductor is that it only absorbs a small portion of solar spectrum in the ultraviolet region, which limits its applications. Therefore, the development of modified TiO₂ with enhanced visible light induced properties is needed to increase the photocatalytic activity for the organic pollutants [8–10].

Carbon nanotube (CNT) is a new category of carbon structure, which was founded in 1991 by Iijima [11]. The ideal carbon nanotubes own seamless, hollow tube structure rolled by graphite surfaces slice layer composed of hexagon carbon atom. According to the number of graphite surface layers, they can be divided into single walled carbon nanotube (SWCNT) and multiwalled carbon nanotube (MWCNT). CNTs are considered to be ideal catalyst carriers due to their huge specific surface area, remarkable chemical stability, unique electronic structure, nanoscale hollow tube property, and good absorbability [12–15].

It was demonstrated in the paper that CNTs are regarded as the carrier of TiO₂ nanoparticle with the aim of improving the photocatalytic activity effectively and make TiO₂ easy to recycle. Herein, MWCNT/TiO₂ nanocomposites were synthesized by surface coating of carbon nanotubes with anatase and rutile types TiO₂ through a modified sol-gel approach using tetrabutyl titanate as the raw material. The obtained

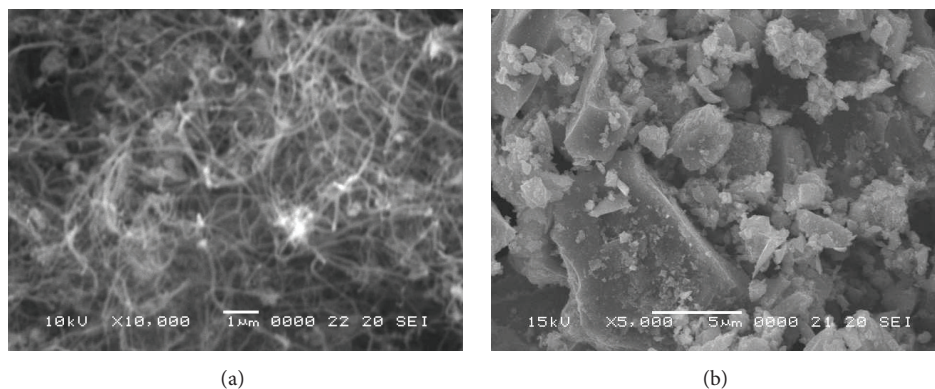


FIGURE 1: Typical SEM morphology of (a) modified MWCNT and (b) MWCNT/TiO₂ nanocomposites.

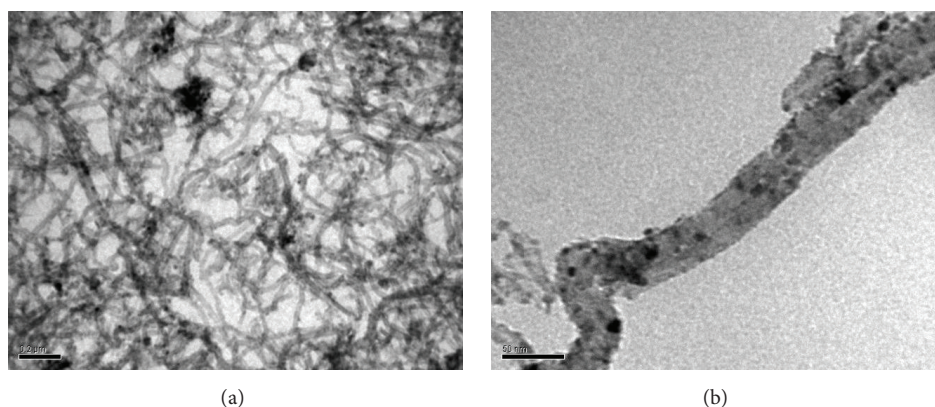


FIGURE 2: Typical TEM images of acid modified MWCNT coated with nanosized TiO₂ materials in low magnification (a) and high magnification (b).

photocatalysts exhibit higher performance for Methyl Orange (MO) than pure TiO₂.

2. Results and Discussion

The morphology and microstructure of the acid modified MWCNT and MWCNT/TiO₂ nanocomposites were observed by Scanning Electron Microscope (SEM) and transmission electron microscope (TEM) investigations, respectively. As shown in Figure 1(a), the acid modified MWCNTs were dispersed uniformly with no or less aggregation. The weaved interconnected networks of carbon nanotubes contribute largely to the homogenous supporting of photocatalyst nanoparticles. After being supported by TiO₂ photocatalysts, as shown in Figure 1(b), the interval space of these weaved MWCNT networks was filled with nanosized TiO₂.

In the TEM image with low magnification (Figure 2(a)), MWCNTs coated with TiO₂ nanoparticles are identified with minor agglomeration of MWCNT. From the TEM image with higher magnification (Figure 2(b)), it can be seen that the TiO₂ nanoparticles with an average size of 15 nm are closely attached on the walls of MWCNT, which agrees with the XRD results below. Furthermore, the long and

tube-like aperture structure of carbon nanotubes with large surface area contributes to the adsorption of the organic molecules. On the other hand, it is observed that the surfaces of MWCNT were not fully covered by TiO₂ nanoparticles, since the number of active sites on MWCNT generated by the acid treatment is not sufficient for the full covering [16].

Figure 3 presents the Fourier transform infrared (FT-IR) spectroscopy spectrum of MWCNT/TiO₂ nanocomposites. The appearance of two strong absorption peaks at 2920 cm⁻¹ and 2850 cm⁻¹ is attributed to symmetrical and asymmetric telescopic vibration of methylene group (-CH₂-) of carbon nanotubes, which indicates that the methylene structure of carbon nanotubes is not destroyed. Two absorption peaks at 1728 cm⁻¹ and 1160 cm⁻¹ demonstrate the formation of carboxyl groups and carbonyl groups in the modification stage [17]. Additionally, the band in the low wavenumber around 670 cm⁻¹ in the spectrum corresponds to the characteristic absorption peak of TiO₂ [18].

In order to describe the crystalline structure of the obtained nanocomposites, X-ray diffraction (XRD) spectra were involved in the characterization. As shown in Figure 4, a characteristic diffraction peak at $2\theta = 26.23^\circ$ is the typical feature of carbon nanotubes. In curve (b), the peaks at $2\theta = 25.33^\circ$ and 27.48° are attributed to anatase and rutile structure

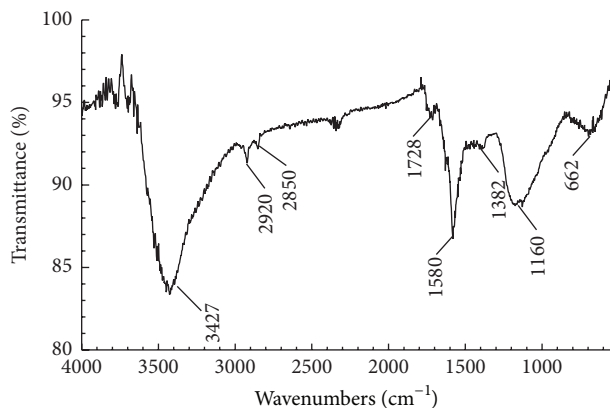
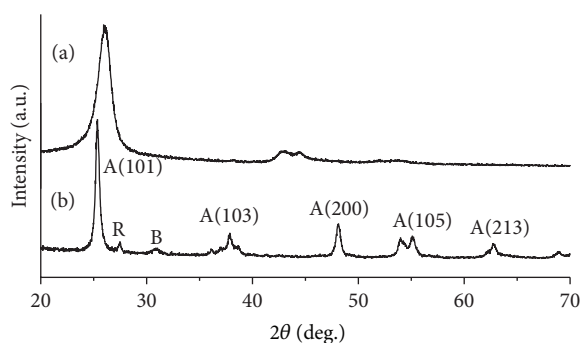


FIGURE 3: FT-IR spectrum of MWCNT/TiO₂ nanocomposites.



A: anatase
R: rutile
B: brookite

FIGURE 4: XRD patterns of MWCNT (a) and MWCNT/TiO₂ (b) nanocomposites.

of TiO₂, respectively [19]. The main characteristic diffraction peak of carbon nanotubes at 25.33° is overlapped with characteristic feature of TiO₂. Furthermore, the obtained TiO₂ particles with around 15 nm were calculated by Scherrer equation using the peak of $2\theta = 25.33^\circ$ [20], which is consistent with TEM images.

In order to evaluate and confirm the chemical compositions of the prepared samples, differential thermal analysis and thermogravimetric (DTA-TG) analysis of carbon nanotubes and MWCNT/TiO₂ nanocomposites is shown in Figure 5. There is an obviously exothermic peak at 650°C, which is attributed to the peak of carbon nanotube. TG curve shows that a weight loss happens at 600°C and it can be supposed that the framework of carbon nanotubes was destroyed and then volatilized. The loading amount of MWCNT in the MWCNT/TiO₂ nanocomposites is about 12 wt.%, which is in agreement with the results of previous reports that the low ratio of carbon-based supporter contributes to the dispersion of catalysts on the supporters [21].

Figure 6 shows the UV-Vis spectra of the pure TiO₂, MWCNT, and MWCNT/TiO₂ nanocomposites. The absorption spectrum for the composites in 400 nm is much higher than that of pure TiO₂. The composites also have stable

absorption in the region of visible light from 400 to 800 nm with slight increase of absorption intensity between 700 and 800 nm in the wavelength. The composites have good absorption properties not only in the ultraviolet area but also in the visible light region, which is of significance for us to exploit and utilize solar energy resources in the application of environmental remediation [22].

To explore the photocatalytic activity of MWCNT/TiO₂ nanocomposites, photocatalytic experiments are performed using MO as the model pollutant under irradiation of ultraviolet lamp. Figure 7 shows the relation of the irradiation time and the degradation of MO by MWCNT/TiO₂, pure TiO₂, and MWCNT. The prepared composites have higher degradation efficiency than pure TiO₂, which is comparable with the previous result that metal-doped TiO₂ (P25) has a much higher photocatalytic activity than pure TiO₂ with a degradation ratio of less than 10% under visible light and around 30% even under a 500 W high-pressure Hg lamp [23]. Within 4 h, the highest photodegradation efficiency can reach 83%. However, only about 53% and 34% of MO were degraded by using pure TiO₂ and MWCNT, respectively. The photocatalytic activities of TiO₂ were largely improved through the addition of MWCNT. The reason can be concluded as follows: firstly, MWCNT can absorb dissolved oxygen and organic matter on the outside of its surface due to the large surface area and special aperture structure; secondly, MWCNTs are eminent electronic conductors that can orderly export electrons from the surface of TiO₂ and quickly reduce electronic accumulation on TiO₂ [24, 25].

3. Experimental Section

3.1. Materials. MWCNT (diameter 10–20 nm, length 1–2 μm, purity: 98%, and ashes 0.2 wt.%) was purchased from Nano Port of Shenzhen Inc.; tetrabutyl titanate (CP) and other chemicals were purchased from Sinopharm Chemical Reagent Limited Corporation.

3.2. Purification of MWCNT. 1.0 g MWCNT were acidified in a mixed solution of concentrated sulfuric (98%) and nitric acids (65%–68%) with a volume ratio of 3:1 under ultrasonication at 70°C for 3 h. Then, the MWCNTs were separated by filtration, followed by the washing with distilled water until pH = 7. The purified MWCNTs were dried at 100°C and ground for the further using.

3.3. Preparation of MWCNT/TiO₂ Composites. In a typical experiment for the preparation of composites, titanium dioxide coated MWCNT was prepared by the following procedure. A precursor solution was prepared by the mixing of 5 mL of ethanol and 1.5 mL of glacial acetic acid as inhibitors. 20 mL of tetrabutyl titanate as a TiO₂ precursor was added dropwise to the solution under stirring. The resulting solution was designated as A. 20 mg of surface modified carbon nanotubes was dispersed in a mixture solution of nitric acid, deionized water, and ethanol. After ultrasonic vibration for 20 min, the obtained suspension was mixed with solution A under constant stirring until the gel formation. The gel was

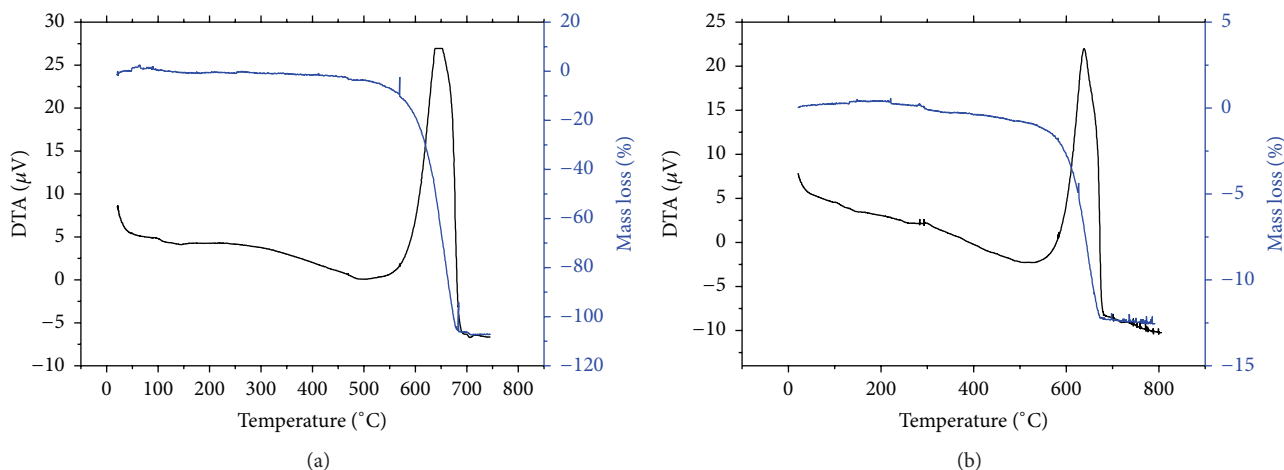


FIGURE 5: DTA-TG curves of MWCNT (a) and MWCNT/TiO₂ (b) nanocomposites.

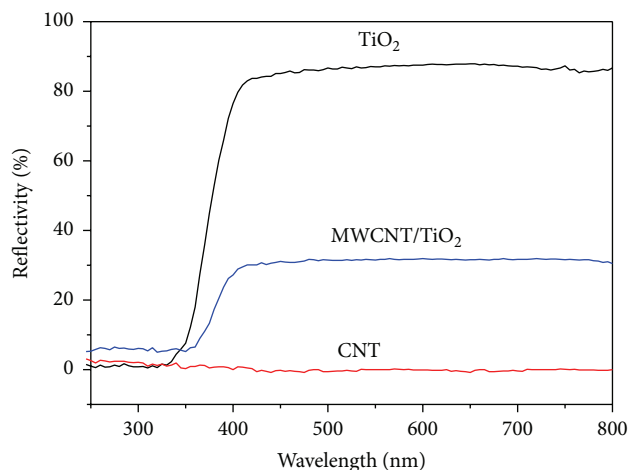


FIGURE 6: UV-Vis absorption spectra of pure TiO₂, MWCNT, and MWCNT/TiO₂ nanocomposites.

aged for 48 h at room temperature, followed by the drying in air at 105°C for about 8 h and the further grinding to a powder. The powder was then calcined at 450°C in air for 2 h to produce MWCNT/TiO₂ nanocomposites.

3.4. Photocatalytic Degradation Experiment. 200 mg nanocomposites were added into 250 mL Methyl Orange (MO) solution with concentration of 20 mg/L. After the pH value of degradation solution was adjusted to about 3, the solution under vigorous stirring was irradiated by 200 W medium mercury lamp with a main wavelength of 365 nm (Beijing Institute of Light Sources). The dispersion was kept in the dark for 60 min for dark adsorption experiments, after which photodegradation was carried out. The dark adsorption was designed to be 60 min because the adsorption results indicate that MO molecules were absorbed to saturation on the surface of catalysts (data not shown). A certain amount of aliquots (3 mL) was taken from solutions every 30 min to

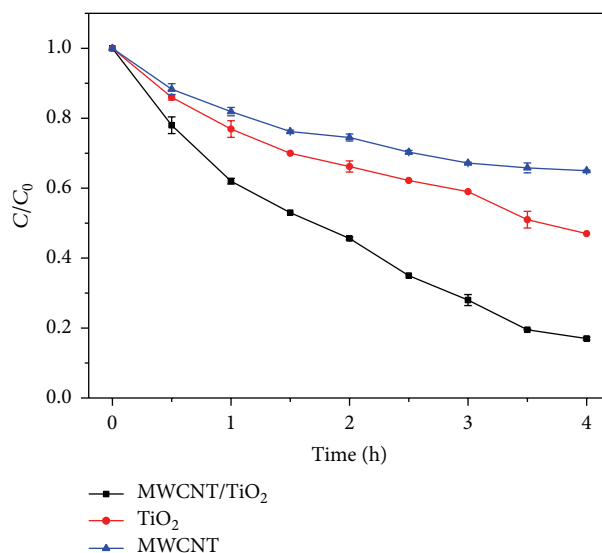


FIGURE 7: Effect of photocatalytic decomposition of Methyl Orange with irradiation time.

determine the concentration of the sample. The concentration of the MO dye was monitored by UV-Vis spectroscopy by recording the absorbance of the characteristic peak of MO at 465 nm. The change of MO concentration was regarded as the evaluation of photocatalytic activity of the composites.

3.5. Characterization and Testing. The FT-IR spectra were recorded on a Shimadzu IR-440 infrared spectrometer. The morphology of the particles was observed by JEM-1230 transmission electron microscope and JSM-5610LV scanning electron microscope. DTA-TG measurement was carried out in static air condition at room temperature. The X-ray diffraction (XRD) patterns were recorded by a PANalytical X'Pert PRO diffractometer operating at 50 kV with Cu $\kappa\alpha$ radiation. The XRD intensity was measured by step scanning

in the 2θ range 10° – 70° with a step of 0.0167° . The UV-Vis spectra of the powder solids were measured on TU-1901 UV-Vis spectrophotometry.

4. Conclusions

In conclusion, MWCNT-based MWCNT/TiO₂ nanocomposites have higher photocatalytic activity than single TiO₂ photocatalyst for the degradation of MO aqueous solution under ultraviolet light irradiation, which is attributable to the uniform coating of TiO₂ nanoparticles and widening of absorption wavelength. This study provides an avenue for the preparation of carbon nanotube-based photocatalysts that utilize ultraviolet as an energy source in the application of environmental remediation. Researches on the composites of including both highly dispersed TiO₂ nanoparticles and highly dispersed carbon nanotubes are anticipated.

Conflict of Interests

The authors declare that there is no conflict of interests regarding the publication of this paper.

Authors' Contribution

The paper was written by contributions of all authors. Yanqing Wang designed the project, conducted the preparation of photocatalysts, the characterization, and its application test, analyzed the results, and was responsible for paper writing. Quanjie Wang analyzed the results and contributed importantly to the paper writing. Baorong Duan and Mengmeng Zhang analyzed the results and gave suggestions. All authors have given approval to the final version of the paper.

Acknowledgments

This study was supported by the National Natural Science Foundation of China (no. 2177142) and the Important Deployment Project of Chinese Academy of Sciences (KZZD-EW-TZ-16).

References

- [1] M. A. Lazar, S. Varghese, and S. S. Nair, "Photocatalytic water treatment by titanium dioxide: recent updates," *Catalysts*, vol. 2, no. 4, pp. 572–601, 2012.
- [2] A. Alinsafi, F. Evenou, E. M. Abdulkarim et al., "Treatment of textile industry wastewater by supported photocatalysis," *Dyes and Pigments*, vol. 74, no. 2, pp. 439–445, 2007.
- [3] M. S. A. S. Shah, K. Zhang, A. R. Park et al., "Single-step solvothermal synthesis of mesoporous Ag–TiO₂–reduced graphene oxide ternary composites with enhanced photocatalytic activity," *Nanoscale*, vol. 5, no. 11, pp. 5093–5101, 2013.
- [4] X. Chen, S. Shen, L. Guo, and S. S. Mao, "Semiconductor-based photocatalytic hydrogen generation," *Chemical Reviews*, vol. 110, no. 11, pp. 6503–6570, 2010.
- [5] A. Di Paola, E. García-López, G. Marci, and L. Palmisano, "A survey of photocatalytic materials for environmental remediation," *Journal of Hazardous Materials*, vol. 211–212, pp. 3–29, 2012.
- [6] J. C. Tristão, F. Magalhães, P. Corio, and M. T. C. Sansiviero, "Electronic characterization and photocatalytic properties of CdS/TiO₂ semiconductor composite," *Journal of Photochemistry and Photobiology A: Chemistry*, vol. 181, no. 2–3, pp. 152–157, 2006.
- [7] K. Hashimoto, H. Irie, and A. Fujishima, "TiO₂ photocatalysis: a historical overview and future prospects," *Japanese Journal of Applied Physics*, vol. 44, no. 12, pp. 8269–8285, 2005.
- [8] R. Asahi, T. Morikawa, T. Ohwaki, K. Aoki, and Y. Taga, "Visible-light photocatalysis in nitrogen-doped titanium oxides," *Science*, vol. 293, no. 5528, pp. 269–271, 2001.
- [9] S. Wang, X. Shi, G. Shao, X. Duan, H. Yang, and T. Wang, "Preparation, characterization and photocatalytic activity of multi-walled carbon nanotube-supported tungsten trioxide composites," *Journal of Physics and Chemistry of Solids*, vol. 69, no. 10, pp. 2396–2400, 2008.
- [10] W. Wang, P. Serp, P. Kalck, C. G. Silva, and J. L. Faria, "Preparation and characterization of nanostructured MWCNT–TiO₂ composite materials for photocatalytic water treatment applications," *Materials Research Bulletin*, vol. 43, no. 4, pp. 958–967, 2008.
- [11] S. Iijima, "Helical microtubules of graphitic carbon," *Nature*, vol. 354, no. 6348, pp. 56–58, 1991.
- [12] R. C. Tenent, T. M. Barnes, J. D. Bergeson et al., "Ultrasoft, large-area, high-uniformity, conductive transparent single-walled-carbon-nanotube films for photovoltaics produced by ultrasonic spraying," *Advanced Materials*, vol. 21, pp. 3210–3216, 2009.
- [13] T. Yamamoto, S. Noda, and M. Kato, "A simple and fast method to disperse long single-walled carbon nanotubes introducing few defects," *Carbon*, vol. 49, no. 10, pp. 3179–3183, 2011.
- [14] X. Li, F. Gittleson, M. Carmo, R. C. Sekol, and A. D. Taylor, "Scalable fabrication of multifunctional freestanding carbon nanotube/polymer composite thin films for energy conversion," *ACS Nano*, vol. 6, no. 2, pp. 1347–1356, 2012.
- [15] Y. Wang and B. Fugetsu, "Mono-dispersed ultra-long single-walled carbon nanotubes as enabling components in transparent and electrically conductive thin films," *Carbon*, vol. 82, pp. 152–160, 2015.
- [16] K. Zhu, N. R. Neale, A. Miedaner, and A. J. Frank, "Enhanced charge-collection efficiencies and light scattering in dye-sensitized solar cells using oriented TiO₂ nanotubes arrays," *Nano Letters*, vol. 7, no. 1, pp. 69–74, 2007.
- [17] S. Muduli, W. Lee, V. Dhas et al., "Enhanced conversion efficiency in dye-sensitized solar cells based on hydrothermally synthesized TiO₂-MWCNT nanocomposites," *ACS Applied Materials and Interfaces*, vol. 1, no. 9, pp. 2030–2035, 2009.
- [18] T. A. Saleh and V. K. Gupta, "Photo-catalyzed degradation of hazardous dye methyl orange by use of a composite catalyst consisting of multi-walled carbon nanotubes and titanium dioxide," *Journal of Colloid and Interface Science*, vol. 371, no. 1, pp. 101–106, 2012.
- [19] Y.-J. Xu, Y. Zhuang, and X. Fu, "New insight for enhanced photocatalytic activity of TiO₂ by doping carbon nanotubes: a case study on degradation of benzene and methyl orange," *The Journal of Physical Chemistry C*, vol. 114, no. 6, pp. 2669–2676, 2010.
- [20] K. Zhang, X. Du, M. B. Katz et al., "Creating high quality Ca:TiO₂-B (CaTi₅O₁₁) and TiO₂-B epitaxial thin films by pulsed laser deposition," *Chemical Communications*, vol. 51, no. 41, pp. 8584–8587, 2015.

- [21] D. Lahiri, F. Rouzaud, S. Namin et al., "Carbon nanotube reinforced polylactide-caprolactone copolymer: mechanical strengthening and interaction with human osteoblasts in vitro," *ACS Applied Materials and Interfaces*, vol. 1, no. 11, pp. 2470–2476, 2009.
- [22] H. Eskandarloo, A. Badii, M. A. Behnajady, and G. M. Ziarani, "UV-LEDs assisted preparation of silver deposited TiO₂ catalyst bed inside microchannels as a high efficiency microphotoreactor for cleaning polluted water," *Chemical Engineering Journal*, vol. 270, pp. 158–167, 2015.
- [23] X.-T. Zhou, H.-B. Ji, and X.-J. Huang, "Photocatalytic degradation of methyl orange over metalloporphyrins supported on TiO₂ degussa P25," *Molecules*, vol. 17, no. 2, pp. 1149–1158, 2012.
- [24] K. Woan, G. Pyrgiotakis, and W. Sigmund, "Photocatalytic carbon-nanotube-TiO₂ composites," *Advanced Materials*, vol. 21, no. 21, pp. 2233–2239, 2009.
- [25] W. Chen, Z. Fan, B. Zhang et al., "Enhanced visible-light activity of titania via confinement inside carbon nanotubes," *Journal of the American Chemical Society*, vol. 133, no. 38, pp. 14896–14899, 2011.

Research Article

Enhanced Adsorption and Removal of Ciprofloxacin on Regenerable Long TiO₂ Nanotube/Graphene Oxide Hydrogel Adsorbents

Yuan Zhuang,¹ Fei Yu,^{2,3} and Jie Ma^{1,4}

¹State Key Laboratory of Pollution Control and Resource Reuse, School of Environmental Science and Engineering, Tongji University, 1239 Siping Road, Shanghai 200092, China

²Tianjin Key Laboratory of Aquatic Science and Technology, Tianjin Chengjian University, 26 Jinjing Road, Tianjin 300384, China

³College of Chemistry and Environmental Engineering, Shanghai Institute of Technology, Shanghai 2001418, China

⁴Jiangsu Key Laboratory for Environment Functional Materials, Suzhou University of Science and Technology, Suzhou 215009, China

Correspondence should be addressed to Fei Yu; fyu@vip.163.com and Jie Ma; jma@tongji.edu.cn

Received 24 October 2015; Accepted 26 November 2015

Academic Editor: Bao Yu Xia

Copyright © 2015 Yuan Zhuang et al. This is an open access article distributed under the Creative Commons Attribution License, which permits unrestricted use, distribution, and reproduction in any medium, provided the original work is properly cited.

To improve the adsorption performance and regeneration ability of adsorbent, a simple method was designed to synthesize long TiO₂ nanotube/reduced graphene oxide (rGO-TON) hydrogel, which has good adsorption and regeneration capacity toward ciprofloxacin. rGO-TON hydrogel could form 3D structure, which makes the separation and regeneration of adsorbent easy. For comparison, commercial P25 particle is used to prepare composite hydrogel with rGO; the results showed that TiO₂ nanotube supports the graphene sheets better than P25 particles, which would reduce the agglomeration of graphene sheets. rGO-TON have larger specific surface area (138.2 m²/g) than rGO-P25 (79.4 m²/g). In this paper, ciprofloxacin was chosen as target pollutants, the rGO-TON obtain excellent adsorption capacity, and the maximum adsorption capacities of rGO-TON for ciprofloxacin calculated from Langmuir model are 178.6 mg/g ($R^2 = 0.9929$), 181.8 mg/g ($R^2 = 0.9954$), and 108.7 mg/g ($R^2 = 0.9964$) for graphene oxide (GO), GO-TON, and GO-P25, respectively. In regeneration, the adsorption capacity of rGO-TON and rGO-P25 has little reduced after 5 cycles, while the adsorption capacity of rGO decreases to below 100 mg/g. Results of this work are of great significance for environmental applications of regenerable long TiO₂ nanotube/graphene oxide hydrogel as a promising adsorbent nanomaterial for antibiotic pollutants from aqueous solutions.

1. Introduction

As the pharmaceuticals industry is blooming these years, more and more antibiotics are polluted into the environment. Moreover, they are usually deposited continuously and maintain stability for a long time in the ecosystem [1]. Ciprofloxacin is a kind of second generation fluoroquinolone antibiotic which has been commonly used in various areas; however, it has a high solubility in aqueous solution at various pH conditions and a high stability in soil and wastewater systems; thus the removal of ciprofloxacin from water is very important [2]. Various chemical and physical methods could be used to remove antibiotic from wastewater [3], such as membrane techniques [4], biodegradation [5], chemical oxidation [6–8], adsorption [9–12], and ion-exchange [13]. Among them,

adsorption is widely used in water treatment as it is easily operated with high removal efficiency. Thus, the adsorbent disposal is necessary after adsorption process [14, 15]. At present, there are two groups of regeneration methods [16]: wet reclamation and dry reclamation. Thermal regeneration, which is a kind of dry reclamation, is the most popular method. However, if not combusted, it could produce pollutant gas. For overcoming these defects, microwave irradiation has been increasingly investigated these years [17]. However, in microwave method, some organic pollutants may volatilize rather than mineralize, and it still could not be used for continuous regeneration.

As a semiconducting metal oxide, titanium dioxide (TiO₂) is widely used due to its excellent photocatalytic

property [8]. Electrons could be excited from the valence band to the conduction band while being irradiated by UV light; during this process, electron-hole pairs are created. Thus TiO_2 possesses photocatalytic character. However, the traditional photocatalytic degradation method has some defect, such as the low usage of the light and the high consume of the energy [18]. For TiO_2 , electron-hole pairs are easy to be recovered which may be faster than the pollutant degradation rate. To overcome the defects in which the electron-hole pairs are easy to be recovered which would reduce the photocatalytic efficiency, a combination of TiO_2 with carbon nanomaterials has been considered as an efficient way [19]. Graphene oxide (GO) has a single layer two-dimensional graphite structure with abundant oxygen functional groups [20, 21]. Through treatment by reduction, GO could form a reduced graphene oxide (rGO) hydrogel, which possesses high adsorption capacity toward antibiotics [22]. GO has great potential to promote fast electron transfer. Thus the photoexcited electrons from TiO_2 are transferred to GO to hinder electron-hole recombination and to enhance oxidative reactivity [23]. There have been many investigations which reported the developments in the preparation of TiO_2 /GO composites for the removal of organic pollutants in water [24, 25]. However, though GO has high adsorption capacity, the regeneration ability is not well for reuse [26]. After the addition of TiO_2 into GO, the composite could be better reused through photocatalytic degradation after adsorption.

Providing TiO_2 with greater interracial contact with the GO surface with lower aggregation is important to improve the photocatalytic performance of GO- TiO_2 composites as this could promote the electron transfer and charge separation from TiO_2 to GO [25]. Comparing with TiO_2 nanoparticles, long TiO_2 nanotubes (TON) have a higher specific surface area and more active sites. Then, while TON and GO have a greater degree of interfacial contact, charge separation would be better; moreover, under higher aspect ratio of TON, the photocatalytic property would be improved [27]. Therefore, we put forward a simple way for the preparation of the rGO-TON hydrogel to remove ciprofloxacin from aqueous solution. Rather than the traditional simultaneous adsorption and photocatalytic degradation, the photocatalytic degradation is operated after adsorption in our study, which would acquire better light availability because the pollutant is more concentrated on the adsorbents after adsorption. The separation of adsorption and photocatalytic degradation would avoid the light scattering caused by external environment or the pollutants. For rGO-TON hydrogel with a 3D microstructure, the separation and regeneration are easy. The results of this work are of great significance for environmental applications of regenerable long TiO_2 nanotube/graphene oxide, as a promising adsorbent nanomaterial for ciprofloxacin pollutants from aqueous solutions.

2. Materials and Methods

2.1. Materials. All chemicals were purchased from Sino-pharm Chemical Reagent Co., Ltd. (Shanghai, China), in analytical purity and were used in the experiments without

any further purification. All solutions were prepared using deionized water.

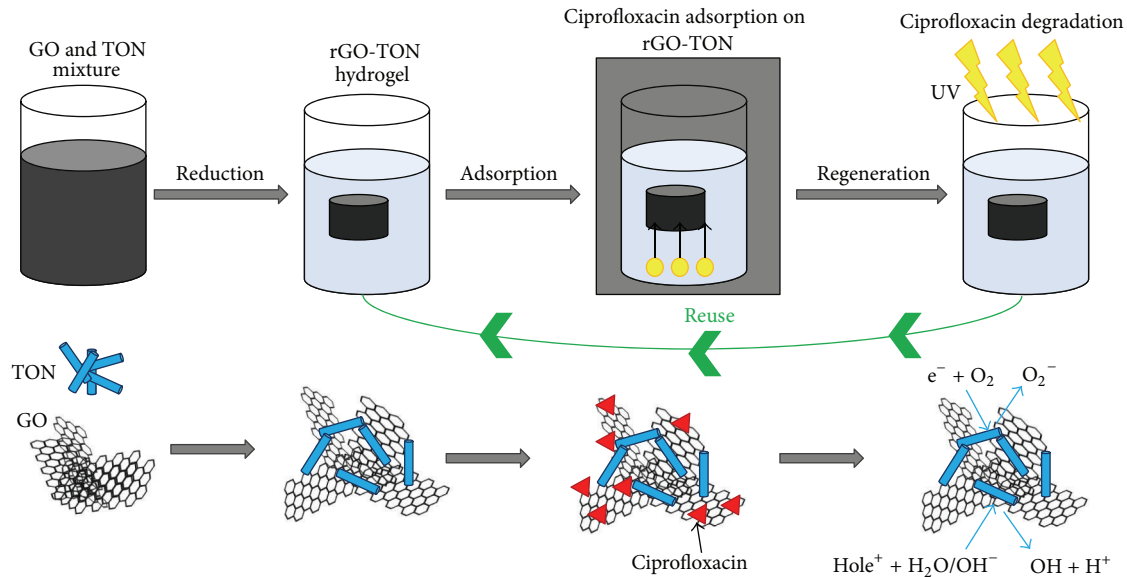
2.2. Preparation. Graphite oxide was prepared using the modified Hummers' method [28–30]. To get GO solution, graphite oxide is dispersed in deionized water and sonicated in an ultrasound bath for 12 h. Commercial P25 (a mixture of 80% anatase and 20% rutile with an average surface area of $50 \text{ m}^2/\text{g}$, size 20–30 nm) was purchased from Degussa Company, Essen, Germany.

TON is prepared by hydrothermal method [31]. 2.7 g P25 powder is put into 300 mL sodium hydroxide solution (8 mol/L), ultrasonic stirred for 2 h, and then magnetic stirred for 5 h, so that the titanium dioxide was fully dissolved in sodium hydroxide solution; then, the solution was transferred into 150 mL polytetrafluoroethylene reactor, the reaction kettle was put into stainless steel jacket, the reaction kettle was assembled and put into the oil bath with the heat conduction oil, and the rotating speed is maintained at 400 rpm, heating up to 130 for 28 h; after the reaction, the reactor was naturally cooled to room temperature; the mother liquor was centrifuged at 4000 rpm for 20 min to obtain coarse product; the filter cake was put into the water to rinse 5 times, until the washing supernatant pH is 12; then hydrochloric acid was added until the pH value of the solution was 2; then the sodium titanate became a hydrogen titanate; the solution was washed 4 times until the supernatant pH was 6, and then the solution was put into the hydrochloric acid; the pH value of the solution was adjusted to 2; after 5 hours, the sodium type is converted into a hydrogen titanate type; through suction filtration and freeze-drying, TON could be obtained.

TON (or P25) and ascorbic acid were put into the GO solution and placed into an ultrasound bath for 5 h to form a uniform solution. The mass ratio of GO to TiO_2 was 2 : 1. The mixed solution was heated under 90°C for 12 h to prepare a hydrogel [2, 11]. The hydrogel without TiO_2 was named rGO.

2.3. Characterization Methods. The material surface morphology of the material was tested by a field-emission scanning electron microscopy (SEM, Hitachi, S-4800) and transmission electron microscopy (TEM, JEOL, JEM-2010). X-ray diffraction (XRD) was tested on a Bragg-Brentano diffractometer (Rigaku, D/Max-2200) under monochromatic $\text{Cu K}\alpha$ radiation ($\lambda = 1.5418 \text{ \AA}$) in a graphite curve monochromator, and the data was collected from $2\theta = 10^\circ - 50^\circ$ with a scan rate of $2^\circ/\text{min}$. The specific surface area and pore parameters were measured using an Accelerated Surface Area and Porosimetry system (Micromeritics, ASAP 2020), calculated from the N_2 adsorption/desorption isotherms at 77 K using BJH model.

2.4. Batch Sorption Experiments. To evaluate the ciprofloxacin adsorption on the adsorbents, batch experiments were operated. Ciprofloxacin (200 mg) is dissolved in 1 L deionized water 200 mg/L stock solution to obtain a 200 mg/L stock solution. The stock solution was diluted with deionized water to get the required concentrations. All the adsorption experiments were operated in 100 mL flasks containing 10 mg



SCHEME 1: Preparation, adsorption, and regeneration process of rGO-TON.

adsorbent and 20 mL ciprofloxacin solutions with required concentrations. The flasks were shaken in a thermostatic shaker at 150 rpm at 298 K for 24 h in the dark. All the adsorption experiments were made in duplicate and calculate the mean values. To ensure that the decrease in the concentration was actually due to the adsorbent rather than by the adsorption on the glass bottle wall, the blank experiments were conducted without the addition of adsorbent. After adsorption, the adsorbent was separated through a $0.45 \mu\text{m}$ membrane. The ciprofloxacin concentration is analyzed by an ultraviolet spectrophotometer (Tianmei UV-2310(II)) at 270 nm for ciprofloxacin. After adsorption, the adsorbents were placed in distilled water UV light for 24 h for regeneration. The above process was repeated 5 times to study the ability of the photocatalytic technology to regenerate the adsorbents.

The adsorption isotherm was studied under initial concentration from 1 mg/L to 200 mg/L at pH = 7, 25°C. The adsorption capacity (mg/g) was calculated using

$$q_t = (C_0 - C_t) \times \frac{V}{m}, \quad (1)$$

where C_0 is the initial concentration, C_t is the concentration of time t (mg/L), V is the initial solution volume (L), and m is the adsorbent dosage (g).

Langmuir model, which assumes that the adsorbate forms a monolayer on the homogenous surface of the adsorbent and there is no interaction between the adsorbed molecules, is used to analyze the adsorption isotherms shown in

$$\frac{C_e}{q_e} = \frac{1}{K_L} + \left(\frac{\alpha_L}{K_L} \right) C_e, \quad (2)$$

where K_L (L/g) and α_L (L/mg) are the Langmuir isotherm constants and α_L relates to the energy of adsorption. When C_e/q_e is plotted against C_e , a straight line will be obtained.

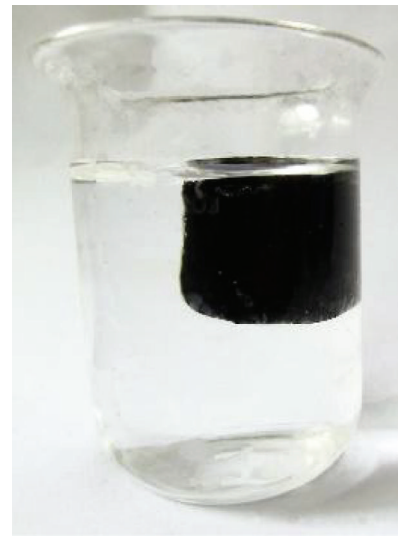


FIGURE 1: Optic image of rGO-TON.

3. Results and Discussion

3.1. Morphology Characterization. The preparation process of rGO-TON hydrogel for ciprofloxacin removal is shown in Scheme 1. GO and TON were mixed to form a uniform solution first, and then the composite hydrogel could be formed after hydrothermal treatment. The ciprofloxacin adsorption on GO/TON was operated in dark. Thus the ciprofloxacin was just adsorbed on GO/TON rather than being degraded. After adsorption, the rGO-TON was treated under UV, and the TON could degrade the ciprofloxacin. Thus the rGO-TON could be reused for adsorption. Optic image of rGO-TON is shown in Figure 1.

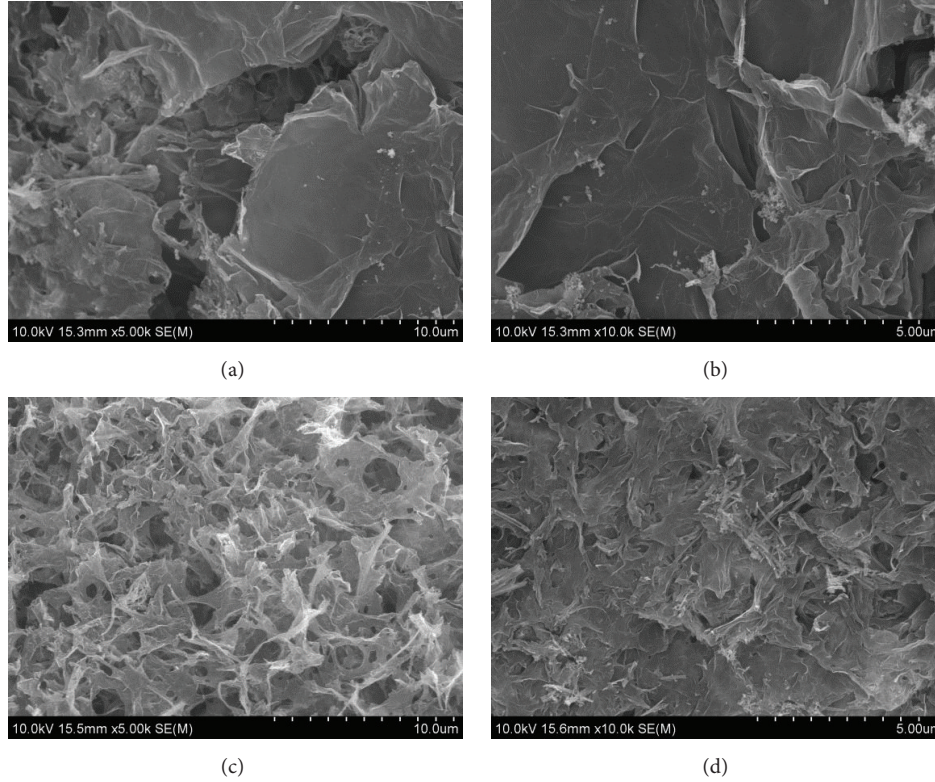


FIGURE 2: SEM images of rGO-P25 (a, b) and rGO-TON (c, d).

To investigate the morphology of rGO-P25 and rGO-TON, the SEM analysis is shown in Figure 2. Obviously, the structure of rGO-TON is totally different, the surface of rGO-P25 consists of thick blocks, while the surface of rGO-TON is fiber-like, as shown in Figures 2(c) and 2(d).

The TEM images of TON, rGO, rGO-P25, and rGO-TON are shown in Figure 3. In Figure 3(a), the as-prepared rGO is shown to have a typical layered structure. In Figures 3(c) and 3(d), it can be seen that both P25 and TON are anchored onto the rGO sheets after the hydrothermal reaction, the diameter of TON is ~ 30 nm, and the diameter of P25 is ~ 50 nm. The length of TON in rGO-TON is more than 500 nm, which is 10 times larger than its diameter. Both the P25 and TON tend to be distributed on the wrinkles and edges of the rGO sheets, which may help to prevent the rGO from agglomeration.

3.2. Composition and Structure Analysis. The specific surface area (SSA) and pore size distribution characterization of rGO, TON, rGO-TON, and rGO-P25 are shown in Figures 4(a) and 4(b). The SSA of rGO and TON are $119.2 \text{ m}^2/\text{g}$ and $139.8 \text{ m}^2/\text{g}$, while rGO-TON and rGO-P25 are $138.2 \text{ m}^2/\text{g}$ and $79.4 \text{ m}^2/\text{g}$, respectively. It can be seen that rGO-TON has larger SSA than rGO-P25, indicating that the tube-like structure of TON may support the graphene sheets better than the particles of P25. Moreover, it can be seen from the pore distribution analysis, as shown in Table 1, that rGO-TON has the highest pore volume among rGO, TON, rGO-TON, and rGO-P25, which indicate that the graphene sheets are well separated by TON. For further investigating the interaction between

TABLE 1: Physical properties of rGO, rGO-TON, and rGO-P25.

Sample	TON	rGO	rGO-TON	rGO-P25
Specific surface area (m^2/g)	139.8	119.2	138.2	79.4
Average pore size (nm)	7.9	6.2	6.5	5.3
Total pore volume (m^3/g)	0.28	0.27	0.48	0.22

graphene and TON or P25, XRD patterns of GO, rGO, TON, rGO-TON, and rGO-P25 are shown in Figure 5. The peak at 10.5° in GO indicates the interlayer space of 0.9 nm. However, in rGO, TON, rGO-TON, and rGO-P25, all the peaks at $2\theta = 10.5^\circ$ are obviously weaker than in GO, indicating that the GO has been reduced to rGO [32]. The disappearance of the rGO characteristic peaks in the rGO-TON indicates that the graphene sheets are separated by TON [33]; however, it can be seen that there is still a small peak around 27° in rGO-P25, indicating that the graphene sheets are better separated by TON than P25, which may be a benefit for SSA of rGO-TON. The peaks of rGO-TON and TON in 25.3° , 37.8° , and 48° correspond to the (101), (004), and (200) planes of the anatase TiO_2 (JCPDS 21-1272), respectively [31].

3.3. Adsorption and Regeneration Properties. Langmuir isotherm is used to fit the ciprofloxacin adsorption on rGO, rGO-TON, and rGO-P25, as shown in Figure 6(a); all the samples were operated in 3 duplicates with presented data equally ($R^2 > 0.9800$). The maximum adsorption capacities are 178.6 mg/g ($R^2 = 0.9929$), 181.8 mg/g ($R^2 = 0.9954$),

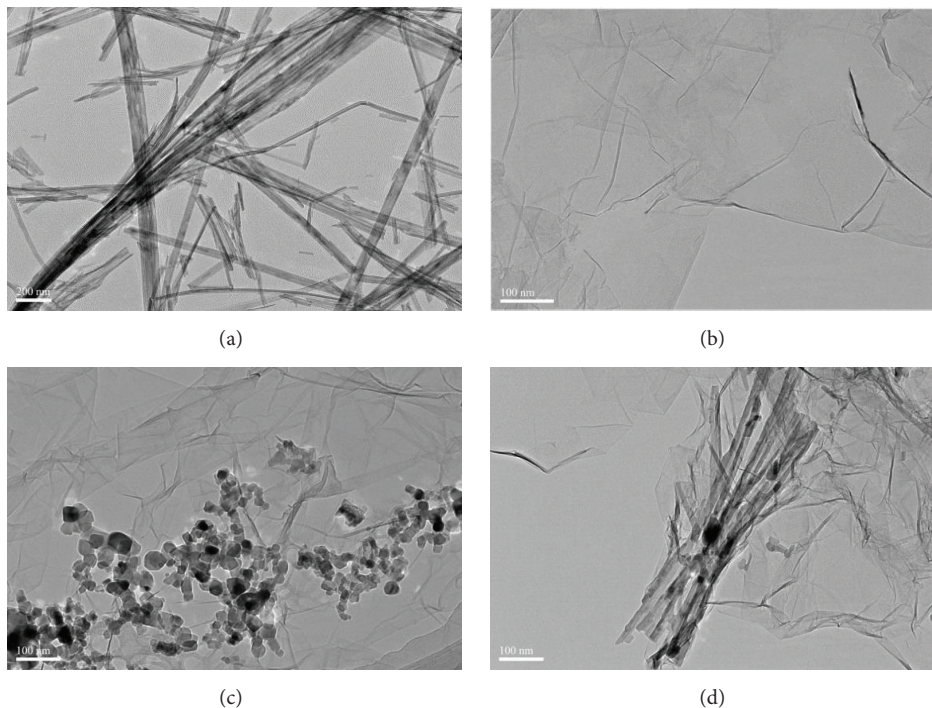


FIGURE 3: TEM images of TON (a), rGO (b), rGO-P25 (c), and rGO-TON (d).

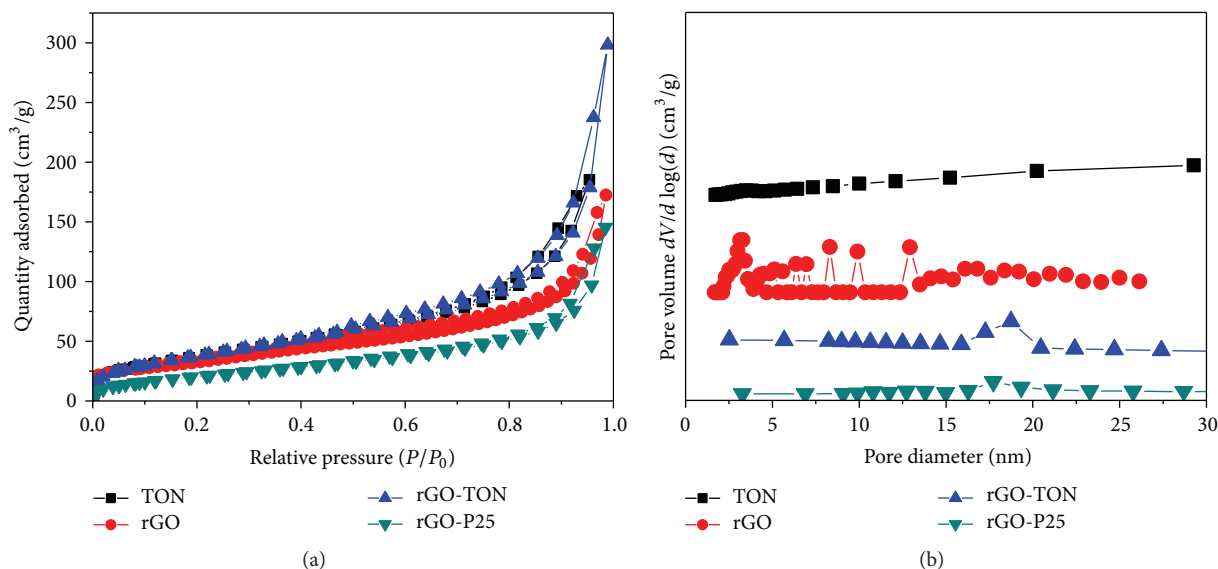


FIGURE 4: N_2 adsorption/desorption isotherms (a) and BJH pore size distribution (b) of rGO, TON, rGO-TON, and rGO-P25.

and 108.7 mg/g ($R^2 = 0.9964$), respectively. The excellent adsorption capacity of rGO-TON is mainly attributed to its larger SSA. Besides physical adsorption, chemical adsorption also plays important role in this adsorption process. During ciprofloxacin adsorption on rGO, rGO-TON, and rGO-P25, the graphene provides $\pi-\pi$ bond and hydrogen bond with ciprofloxacin. One of the driving forces for the organic chemicals adsorption on graphene is electron donor-acceptor interaction owing to the benzene rings. With -OH groups

on the surface, graphene could act as electron donors and enhanced adsorption significantly through forming $\pi-\pi$ bond [34]. Figure 6(b) shows the regeneration of rGO, rGO-TON, and rGO-P25; all the samples were operated in 3 duplicates with presented data equally ($R^2 > 0.98$). Obviously, the rGO-TON and rGO-P25 have little reduction of adsorption capacity after 5 cycles, while the rGO decreases to below 100 mg/g. It can be seen that both TON and P25 promote the composite hydrogel with good regeneration

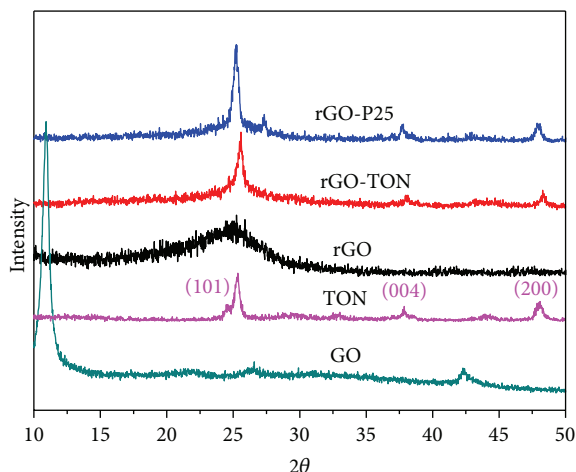
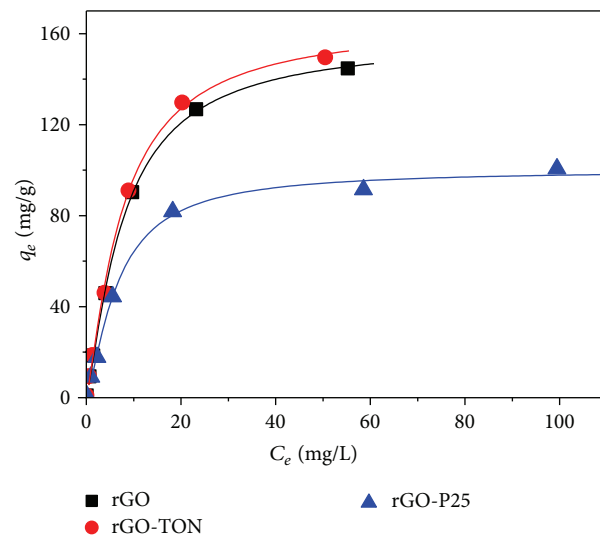


FIGURE 5: XRD of rGO, TON, rGO-TON, and rGO-P25.

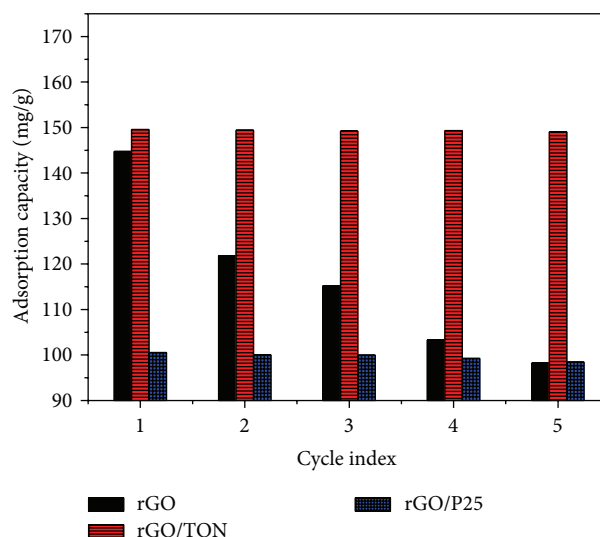
ability. While under the UV irradiation, electron-hole pairs are generated in TiO_2 , which could move immediately from valence band to conduction band in the excited state, and the charge separation and hydroxyl radical formation occur in the regeneration process. Moreover, the electrons transfer from TiO_2 to rGO, and the photogenerated holes stay behind in the valence band. Therefore, the electrons and holes are separated immediately and then react with dissolved oxygen and water molecules to form hydroxyl radical, acting as a strong oxidant for ciprofloxacin degradation [35]. Therefore, the rGO has good adsorption capacity but low regeneration capacity; however, the rGO-P25 has good regeneration ability but the adsorption capacity is not well while the rGO-TON has both good adsorption capacity and regeneration ability.

4. Conclusion

To combine the adsorption of graphene and photocatalytic degradation of TiO_2 , TiO_2 nanotube-reduced graphene oxide (rGO-TON) hydrogel is prepared toward ciprofloxacin removal. Commercial P25 particle is used for comparison with long TON; graphene sheets are shown to be better separated by TON than P25. The resulting rGO-TON have a higher specific surface area, adsorption capacity, and regeneration ability than rGO-P25. Calculated from Langmuir model, the maximum adsorption capacities of ciprofloxacin on the hydrogels are 178.6, 181.8, and 108.7 mg/g, respectively, indicating the excellent adsorption ability of rGO-TON. The rGO has good adsorption capacity, but the regeneration ability is low while the rGO-P25 has good regeneration ability but the adsorption capacity is not well. However, the rGO-TON overcome the above-mentioned defects of rGO and rGO-P25; it has both good adsorption capacity and regeneration ability attributed to the combination of graphene and long TON. Therefore, results of this work are of great significance for environmental applications of regenerable long TiO_2 nanotube/graphene oxide hydrogel adsorbent for antibiotic pollutants.



(a)



(b)

FIGURE 6: Langmuir isotherm model (a) and regeneration properties (b) (initial concentration 200 mg/L) of rGO, rGO-TON, and rGO-P25.

Conflict of Interests

The authors declare that there is no conflict of interests regarding the publication of this paper.

Acknowledgments

This research was supported by the National Natural Science Foundation of China (no. 21577099), the Research Fund of Tianjin Key Laboratory of Aquatic Science and Technology (no. TJKLAST-ZD-2014-06), the Opening Project (no. SJHG140) of the Jiangsu Key Laboratory for Environment Functional Materials, State Key Laboratory of Pollution Control and Resource Reuse Foundation (no. PCRRF14021),

and the Fundamental Research Funds for the Central Universities.

References

- [1] J. Ma, M. X. Yang, F. Yu, and J. H. Chen, "Easy solid-phase synthesis of pH-insensitive heterogeneous CNTs/FeS Fenton-like catalyst for the removal of antibiotics from aqueous solution," *Journal of Colloid and Interface Science*, vol. 444, pp. 24–32, 2015.
- [2] Y. Zhuang, F. Yu, J. Ma, and J. H. Chen, "Adsorption of ciprofloxacin onto graphene–soy protein biocomposites," *New Journal of Chemistry*, vol. 39, no. 5, pp. 3333–3336, 2015.
- [3] V. Homem and L. Santos, "Degradation and removal methods of antibiotics from aqueous matrices—a review," *Journal of Environmental Management*, vol. 92, no. 10, pp. 2304–2347, 2011.
- [4] I. Koyuncu, O. A. Arıkan, M. R. Wiesner, and C. Rice, "Removal of hormones and antibiotics by nanofiltration membranes," *Journal of Membrane Science*, vol. 309, no. 1–2, pp. 94–101, 2008.
- [5] S. Chelliapan, T. Wilby, and P. J. Sallis, "Performance of an up-flow anaerobic stage reactor (UASR) in the treatment of pharmaceutical wastewater containing macrolide antibiotics," *Water Research*, vol. 40, no. 3, pp. 507–516, 2006.
- [6] I. Arslan-Alaton and S. Dogruel, "Pre-treatment of penicillin formulation effluent by advanced oxidation processes," *Journal of Hazardous Materials*, vol. 112, no. 1–2, pp. 105–113, 2004.
- [7] Y. B. Liu, J. H. Li, B. X. Zhou et al., "Photoelectrocatalytic degradation of refractory organic compounds enhanced by a photocatalytic fuel cell," *Applied Catalysis B: Environmental*, vol. 111–112, pp. 485–491, 2012.
- [8] Y. Liu, B. Zhou, J. Bai et al., "Efficient photochemical water splitting and organic pollutant degradation by highly ordered TiO₂ nanopore arrays," *Applied Catalysis B: Environmental*, vol. 89, no. 1–2, pp. 142–148, 2009.
- [9] Y. Zhuang, F. Yu, J. Ma, and J. Chen, "Graphene as a template and structural scaffold for the synthesis of a 3D porous bio-adsorbent to remove antibiotics from water," *RSC Advances*, vol. 5, no. 35, pp. 27964–27969, 2015.
- [10] F. Yu, J. Ma, and D. Bi, "Enhanced adsorptive removal of selected pharmaceutical antibiotics from aqueous solution by activated graphene," *Environmental Science and Pollution Research*, vol. 22, no. 6, pp. 4715–4724, 2014.
- [11] J. Ma, Y. Mingxuan, F. Yu, and Z. Jie, "Water-enhanced removal of ciprofloxacin from water by porous graphene hydrogel," *Scientific Reports*, vol. 5, article 13578, 2015.
- [12] F. Yu, J. Ma, and S. Han, "Adsorption of tetracycline from aqueous solutions onto multi-walled carbon nanotubes with different oxygen contents," *Scientific Reports*, vol. 4, article 5326, 2014.
- [13] K.-J. Choi, J.-H. Choi, E.-H. Hwang, Y.-W. Rhee, and T.-S. Hwang, "Preparation and characterization of heterogeneous anion exchange membrane for recovery of sulfate ion from waste water," *Polymer*, vol. 31, no. 3, pp. 247–254, 2007.
- [14] A. S. A. Bakr, Y. M. Moustafa, M. M. H. Khalil, M. M. Yehia, and E. A. Motawea, "Magnetic nanocomposite beads: synthesis and uptake of Cu(II) ions from aqueous solutions," *Canadian Journal of Chemistry*, vol. 93, no. 3, pp. 289–296, 2015.
- [15] T. Gao, W. Wang, and A. Wang, "A pH-sensitive composite hydrogel based on sodium alginate and medical stone: synthesis, swelling, and heavy metal ions adsorption properties," *Macromolecular Research*, vol. 19, no. 7, pp. 739–748, 2011.
- [16] F. Yu, L. Chen, J. Ma et al., "Self-regenerative adsorbent based on the cross-linking chitosan for adsorbing and mineralizing azo dye," *RSC Advances*, vol. 4, no. 11, pp. 5518–5523, 2014.
- [17] K. B. Yang, J. H. Peng, C. Srinivasakannan, L. B. Zhang, H. Y. Xia, and X. H. Duan, "Preparation of high surface area activated carbon from coconut shells using microwave heating," *Bioresource Technology*, vol. 101, no. 15, pp. 6163–6169, 2010.
- [18] J. Ma, M. X. Yang, Y. R. Sun et al., "Fabrication of Ag/TiO₂ nanotube array with enhanced photo-catalytic degradation of aqueous organic pollutant," *Physica E: Low-Dimensional Systems and Nanostructures*, vol. 58, pp. 24–29, 2014.
- [19] S. H. Hsieh, W. J. Chen, and C. T. Wu, "Pt-TiO₂/graphene photocatalysts for degradation of AO7 dye under visible light," *Applied Surface Science*, vol. 340, pp. 9–17, 2015.
- [20] Q. Xiang, J. Yu, and M. Jaroniec, "Enhanced photocatalytic H₂-production activity of graphene-modified titania nanosheets," *Nanoscale*, vol. 3, no. 9, pp. 3670–3678, 2011.
- [21] L. Yu, Y. Ma, C. N. Ong, J. Xie, and Y. Liu, "Rapid adsorption removal of arsenate by hydrous cerium oxide–graphene composite," *RSC Advances*, vol. 5, no. 80, pp. 64983–64990, 2015.
- [22] J. Ma, M. X. Yang, F. Yu, and J. Zheng, "Water-enhanced removal of ciprofloxacin from water by porous graphene hydrogel," *Scientific Reports*, vol. 5, Article ID 13578, 2015.
- [23] D. L. Zhao, G. D. Sheng, C. L. Chen, and X. K. Wang, "Enhanced photocatalytic degradation of methylene blue under visible irradiation on graphene@TiO₂ dyade structure," *Applied Catalysis B: Environmental*, vol. 111–112, pp. 303–308, 2012.
- [24] G. Williams, B. Seger, and P. V. Kamt, "TiO₂-graphene nanocomposites. UV-assisted photocatalytic reduction of graphene oxide," *ACS Nano*, vol. 2, no. 7, pp. 1487–1491, 2008.
- [25] S. D. Perera, R. G. Mariano, K. Vu et al., "Hydrothermal synthesis of graphene-TiO₂ nanotube composites with enhanced photocatalytic activity," *ACS Catalysis*, vol. 2, no. 6, pp. 949–956, 2012.
- [26] Y. Zhuang, F. Yu, J. Ma, and J. H. Chen, "Graphene as a template and structural scaffold for the synthesis of a 3D porous bio-adsorbent to remove antibiotics from water," *RSC Advances*, vol. 5, no. 35, pp. 27964–27969, 2015.
- [27] Y. Yao, G. Li, S. Ciston, R. M. Lueptow, and K. A. Gray, "Photoreactive TiO₂/carbon nanotube composites: synthesis and reactivity," *Environmental Science and Technology*, vol. 42, no. 13, pp. 4952–4957, 2008.
- [28] T. S. Gendy, Y. Barakat, and A. I. Mead, "Adsorption of ethoxylated alkylphenol–formaldehyde polymeric surfactants at the aqueous solution–air interface," *Polymer International*, vol. 33, no. 3, pp. 247–252, 1994.
- [29] M. Hirata, T. Gotou, S. Horiuchi, M. Fujiwara, and M. Ohba, "Thin-film particles of graphite oxide I: high-yield synthesis and flexibility of the particles," *Carbon*, vol. 42, no. 14, pp. 2929–2937, 2004.
- [30] S. Mao, H. H. Pu, and J. H. Chen, "Graphene oxide and its reduction: modeling and experimental progress," *RSC Advances*, vol. 2, no. 7, pp. 2643–2662, 2012.
- [31] P. Gao, A. Li, D. D. Sun, and W. J. Ng, "Effects of various TiO₂ nanostructures and graphene oxide on photocatalytic activity of TiO₂," *Journal of Hazardous Materials*, vol. 279, pp. 96–104, 2014.
- [32] C. Xu, X. Wang, and J. Zhu, "Graphene–metal particle nanocomposites," *Journal of Physical Chemistry C*, vol. 112, no. 50, pp. 19841–19845, 2008.

- [33] W. Yao, Y. Li, D. Yan et al., "Fabrication and photocatalysis of TiO₂-graphene sandwich nanosheets with smooth surface and controlled thickness," *Chemical Engineering Journal*, vol. 229, pp. 569–576, 2013.
- [34] H. Chen, B. Gao, and H. Li, "Functionalization, pH, and ionic strength influenced sorption of sulfamethoxazole on graphene," *Journal of Environmental Chemical Engineering*, vol. 2, no. 1, pp. 310–315, 2014.
- [35] P. Gao, A. R. Li, D. D. Sun, and W. J. Ng, "Effects of various TiO₂ nanostructures and graphene oxide on photocatalytic activity of TiO₂," *Journal of Hazardous Materials*, vol. 279, pp. 96–104, 2014.

Research Article

Preparation of Stellerite Loading Titanium Dioxide Photocatalyst and Its Catalytic Performance on Methyl Orange

Hua Chen,^{1,2,3} Jianhua Wang,¹ Huajun Wang,¹ Fei Yang,² Jia-nan Zhou,³ Jiajun Fu,³ Jie Yang,³ Zheng Yuan,³ and Bingbing Zheng³

¹Zhejiang Yongtai Paper Co. Ltd., Hangzhou 311421, China

²State Key Lab of Pulp and Paper Engineering, South China University of Technology, Guangzhou 510640, China

³Zhejiang Provincial Key Lab for Chem & Bio Processing Technology of Farm Product, School of Light Industry, Zhejiang University of Science and Technology, Hangzhou 310023, China

Correspondence should be addressed to Fei Yang; 7008774@qq.com

Received 7 October 2015; Accepted 11 November 2015

Academic Editor: Bao Yu Xia

Copyright © 2015 Hua Chen et al. This is an open access article distributed under the Creative Commons Attribution License, which permits unrestricted use, distribution, and reproduction in any medium, provided the original work is properly cited.

TiO₂/stellerite composite photocatalysts were prepared by dispersing TiO₂ onto the surface of HCl, NaOH, or NaCl treated stellerite using a sol-gel method. The materials were characterized by scanning electron microscopy (SEM), energy dispersive X-ray (EDX), Fourier transform infrared spectroscopy (FT-IR), BET surface area analysis, and X-ray diffraction (XRD). HCl and NaCl modification result in the promotion of the pore formation at the stellerite surfaces and induced the microscopic changes, while the surface morphology and structure of the stellerite were almost ruined by NaOH modification. Supported TiO₂ calcinated at 200°C presented anatase structure. The photocatalytic degradation activities of TiO₂ loaded HCl and NaCl modified stellerite were better than that of natural stellerite, accompanied with increasing specific surface area. On the contrary, NaOH modification induced the loss of photocatalytic ability of composite due to the generation of silicates.

1. Introduction

In recent years, with the rapid development of China's economy, the industry has achieved a rapid development. However, the environmental impact should not be overlooked. For example, the amount of discharge of papermaking wastewater amounted to 2.855 billion tons in 2013, accounting for 14.9% of total industrial wastewater.

The traditional industrial wastewater treatment included physical chemistry and biochemical methods [1, 2]. However, the adsorbable organic halogens (AOX) in wastewater cannot be effectively treated by those methods. It was reported that AOX can be decomposed by enzyme treatment, but the technique is still at the experimental stage because of high costs, considerable treatment time, and lack of substrates [3].

In recent years, titanium dioxide catalyst is generally applied for treating wastewater containing organic contaminants due to its excellent ability to achieve complete mineralization of the organic contaminants under moderate

conditions such as ambient temperature and ambient pressure [4, 5]. TiO₂ photocatalytic degradation of a cellulose ECF effluent was evaluated by Pérez et al. [6]. It was found that after 30 min of reaction more than 60% of the toxicity was removed and after 420 min of reaction none of the initial chlorinated low molecular weight compounds were detected, suggesting an extensive mineralization which was corroborated by 95 and 50% AOX and TOC removals, respectively.

However, the difficulties of the nano TiO₂ particle's fixation and recovery due to its small diameter seriously impede its industrialization, so the supported problem has become a hot research topic in TiO₂ photocatalysis domain at present.

Recent research has investigated many kinds of supports for dispersing TiO₂: zeolite [7], glass [8], stainless steel [9], carbon nanotube [10], and graphene [11] are some very recent examples reported in the literature.

Among these materials, zeolites are attractive candidates due to their uniform pores and channel sizes, huge surface area, high adsorption capacity, and low cost. However, the adsorption ability of natural zeolite to pollutants is very limited because the channels and cavities of the zeolite structure were blocked. In order to improve the absorption and exchange capacities and pollution treatment capabilities of zeolite, many attempts have been made such as ion exchange, organic modification, and calcination modification. Among them, the ion exchange modification method becomes the research focus because of its convenient operation, pollution, and environmental friendliness.

In this study, we are concerned with the photocatalytic decomposition of methyl orange (MO) over TiO₂ composite nanophotocatalyst prepared by dispersing TiO₂ on the surface of modified stellerite. The structure, crystal phase, morphology, BET surface area, and photocatalytic activity of the prepared photocatalyst were also investigated.

2. Experimental

2.1. Materials

2.1.1. Modified of Stellerite. Stellerite was obtained from Jinshansida Co. Ltd. (Guangxi, China). Chemical composition of the zeolite is (K_{0.017}Na_{0.042}Ca_{1.13})_{1.189}[Al_{1.997}Si_{7.05}O₁₈]_{6.75}H₂O. The stellerite was washed repeatedly by distilled water in order to remove some impurity ions and then was dehydrated in an oven box at 100°C for 12 h. 7.5 g of stellerite was put into a round flask containing 75 mL different concentrations of HCl, NaOH, or NaCl aqueous solution. The reaction was maintained at 90°C for 4 h under stirring. The solid-liquid mixture was filtrated afterwards, and the stellerite was cleaned with distilled water. A AgNO₃ test was performed to make sure that no Cl⁻ remained in the stellerite. After grinding, the stellerite was calcinated at 100°C for 12 h. These stellerites were denoted as *n*AcMS, *n*AIMS, and *n*SMS, where *n* is the concentration of HCl, NaOH, and NaCl aqueous solution.

2.1.2. Scanning Electron Microscopy (SEM) Analysis. Morphologies of the fracture surfaces were examined with a scanning electron microscope (SEM S3700, Hitachi, Japan) operating at an accelerating voltage of 10 kV. Before observation, the samples were coated with gold using a vacuum sputter-coater.

2.1.3. Fourier Transform Infrared Spectroscopy Analysis. Fourier transform infrared spectroscopy analysis (FTIR) of the samples was carried out in transmission mode using macro techniques (13 mm Φ pellet; ca. 1.5 mg sample with 350 mg KBr). The spectra were recorded with a Nexus Vector spectrometer made by Thermo Nicolet (Nexus 670, Thermo Nicolet Company, USA) under the following specifications: apodization: triangular; detector: DTGS/KBr; regulation: 4 cm⁻¹; number of scans: 32.

2.1.4. X-Ray Diffraction Analysis. The X-ray powder diffraction patterns of the samples were recorded on Bruker D8

Advance X-ray diffractometer (step size 0.02°, 17.7 s per step). A generator with 40 kV and current of 40 mA was employed as a source for CuKα radiation.

2.1.5. Preparation of Photocatalyst. TiO₂ loaded on stellerite was prepared by sol-gel process. The precursor solution composites consist of tetra-*n*-butyl titanate, pure ethanol, and nitric acid. The nitric acid was used as catalyst to control the hydrolysis process. The detailed steps are as follows: A given amount of tetrabutyl titanate was dissolved in pure ethanol with a volume ratio of 1:4 of tetrabutyl titanate to ethanol, and then nitric acid solution was added dropwise into the solution to readjust the pH value to 4. Stirring for 20 min, a certain amount of natural stellerite or modified stellerite was added and the ratio of TiO₂:stellerite is 28:100. Stirring for 10 min, a certain amount of distilled water was added and the volume ratio of distilled water: nitric acid is 1:1. After stirring for 15 min, weak gray sol was obtained and then dried at 100°C for 24 h and at 200°C for 4 h and ground to fine powder in an agate mortar. By this procedure, TiO₂ loaded on stellerite was prepared, denoted as TiO₂/stellerite or *n*TiO₂/AcMS, *n*TiO₂/AIMS, and *n*TiO₂/SMS, where *n* is the concentration of HCl, NaOH, or NaCl aqueous solution in the procedure of stellerite modified treatment.

2.1.6. Characterization of Photocatalyst. The effect of stellerite modification on the photocatalytic activity of TiO₂/stellerite photocatalyst was investigated using methyl orange (MO) as the target compound. A total amount of 0.8 g of photocatalyst was suspended in a 400 mL of 15 mg/L MO solution. The suspension was stirred magnetically for 30 min to reach adsorption equilibrium. The photocatalytic reactions were carried out in a quartz tube irradiated by 365 nm UV light (light irradiation of 2200 μW/cm²). The suspensions were withdrawn at intervals and centrifuged at 14,000 rpm for 10 min and then the residual concentration of MO was determined in solution at 460 nm using a UV-Vis spectrophotometer (DR5000, HACH, USA). The removal rate of MO was calculated by the following equation:

$$\eta = \frac{C_0 - C}{C_0} = \frac{A_0 - A}{A_0} \times 100\%, \quad (1)$$

where C_0 and A_0 are the initial concentration and absorbency of MO solution; C and A are the concentration and absorbency of MO solution after a certain time. Control experiments (direct photolysis) were also carried out without the addition of photocatalyst.

All experiments were run in triplicate with the relative standard deviations (RSD) of about 5%.

3. Results and Discussion

3.1. SEM Imaging of Natural and Modified Stellerites. The surface morphology of natural and modified stellerites is shown in Figure 1. It was found that natural stellerite occurs as clear layer shape structure. As a result of HCl and NaCl modification, microcracks developed on the surface of stellerite. However, the layer shape structure of stellerite changes

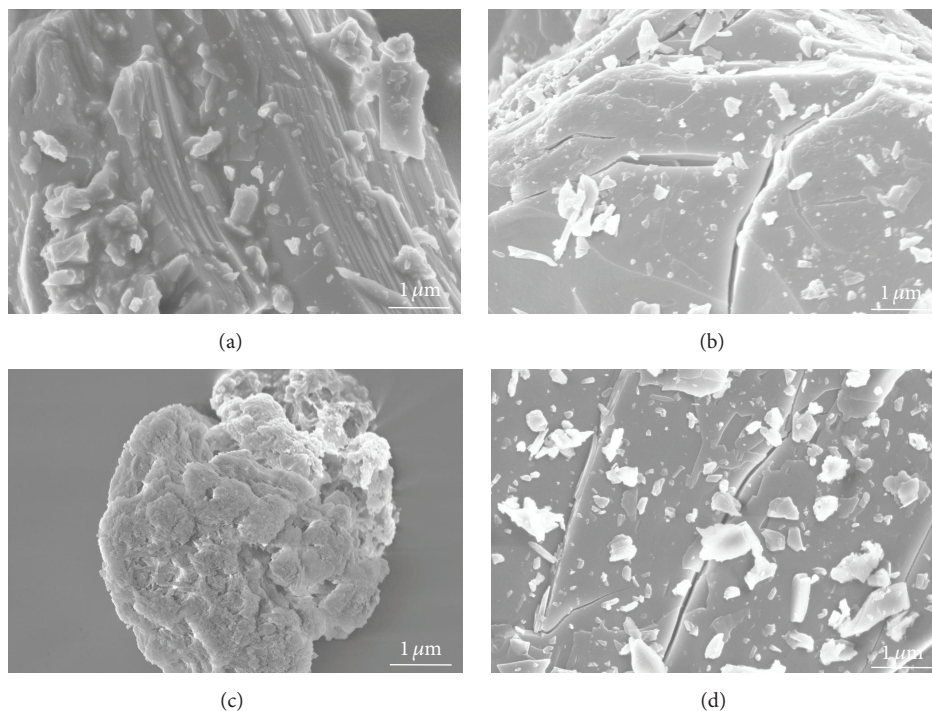


FIGURE 1: SEM images of natural and modified stellerites: (a) natural stellerite, (b) 1.0AcMS, (c) 0.2AlMS, and (d) 1.0SMS.

to irregular granular structure because of the corrosion by NaOH solution.

3.2. Si/Al Atomic Ratio. The influence on the Si/Al atomic ratios of stellerites by different concentrations of modifying agents is shown in Figure 2. In HCl modification, the Si/Al atomic ratio was raised with the increase of HCl concentration and 13.86 (surged almost fourfold) of Si/Al atomic ratio was obtained by HCl modification with the concentration of 1.0 mol/L, indicating that HCl has a strong dealuminization power correlated with the occurrence of hydroxy nest [12]. The dealuminization reaction can be represented as in Scheme 1.

Instead, the Si/Al atomic ratio decreased with the increase in the concentration of NaOH and NaCl, particularly in NaOH modification; these results are in accord with previous report [13]. The mechanism of silica dissolution is shown in Scheme 2.

3.3. FTIR Spectra Analysis. The FTIR spectra of natural and modified stellerite samples are shown in Figure 3. The bands at 3480 and 1642 cm^{-1} were attributed to the valence and bending vibrations of water molecules in stellerite. The peak at 1040 cm^{-1} indicates the asymmetrical extensional vibrations of Si(Al)-O. The bands at 795 and 456 cm^{-1} were due to the symmetric stretching and bending vibrations of Si(Al)-O.

An obvious shift of the IR vibrations to high frequency for 1.0AcMS in comparison with that of the corresponding natural stellerite sample indicates the dealumination during

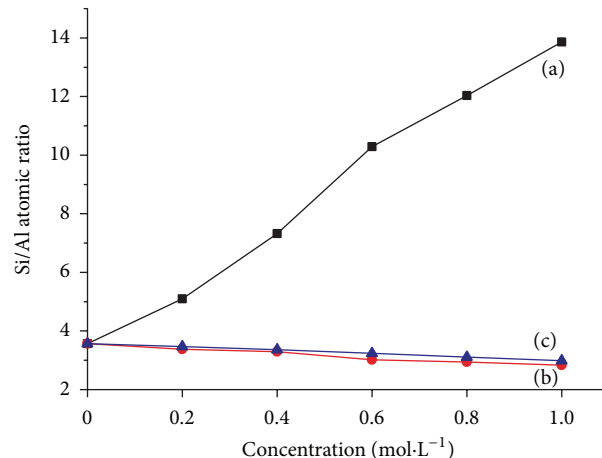
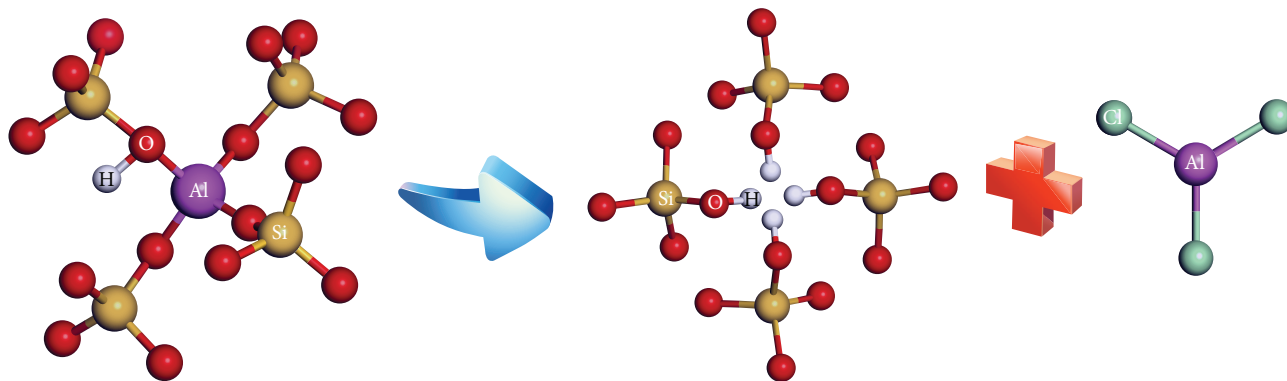
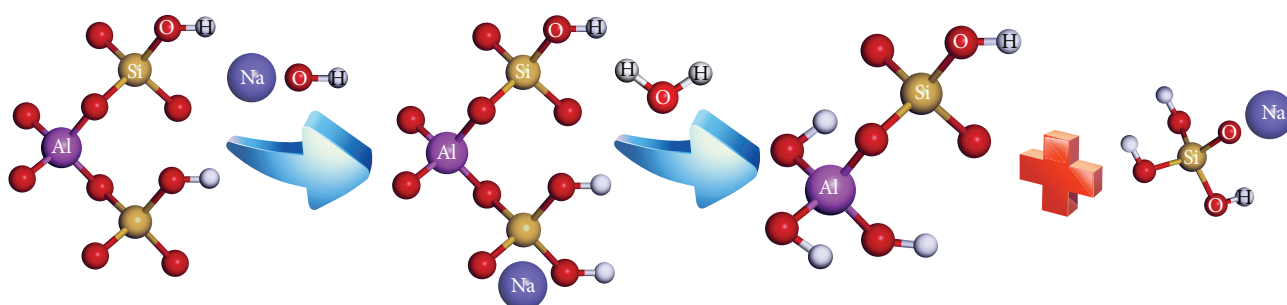


FIGURE 2: Si/Al atomic ratios of natural and modified stellerites: (a) HCl modification, (b) NaOH modification, and (c) NaCl modification.

hydrochloric acid modification. The blue shift is particularly obvious for the Si(Al)-O intensive asymmetric stretching vibrations at about 1040 cm^{-1} . By contrast, NaOH modification caused noticeable red shift at 1035 cm^{-1} in spectra (c) because of the desilication processes (the vibration frequency of Si-O is higher than Al-O). Contrary to the spectra of (a) and (d), most band positions did not change following NaCl modification, suggesting that the base stellerite did not collapse.



SCHEME 1: Schematic representation of the dealuminization upon treatment in hydrochloric acid.



SCHEME 2: Schematic representation of the desilication upon treatment in NaOH solution.

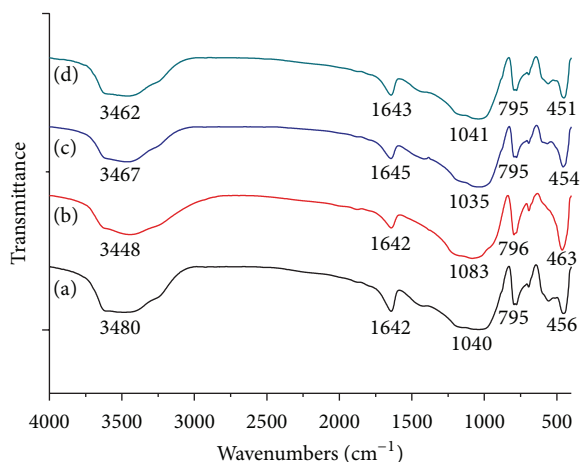


FIGURE 3: FTIR spectra of (a) natural stellerite, (b) 1.0AcMS, (c) 0.2AlMS, and (d) 1.0SMS.

3.4. Structural Analysis. Table 1 presents the parameters of porous structure of various samples. The S_{BET} value for natural stellerite is $2.2 \text{ m}^2/\text{g}$; in the case of treatment of stellerite with 0.4 M HCl , its S_{BET} value grows to $67.9 \text{ m}^2/\text{g}$ and the V_{BET} value grew by 7 times. Besides, D_{BET} and D_{BJH} of the HCl and NaCl modified samples are also significantly smaller in comparison with the natural stellerite, indicating the creation of microporous structure. However, D_{BET} and D_{BJH} of the NaOH modified sample grow to 12.7 and 41.0 nm

and reveal that NaOH modified stellerite can bring about different effect of surface topography compared with HCl and NaCl modified stellerite, and this result is consistent with Figure 1.

The adsorption-desorption isotherms for natural and modified stellerite are shown in Figure 4. Based on conventional classification of adsorption, the isotherms of natural and 0.2AlMS can be considered as isotherms of IV type with the hysteresis loop of the type H3. In comparison, the nitrogen adsorption on the HCl and NaCl modified stellerite is expressed by I type isotherm with wide hysteresis loop which does not close at low relative pressure. The obvious increases of the micropore volumes of the HCl and NaCl modified stellerite are caused by unblocking of the channels of framework structure of stellerite through dealuminization during acid modification or ion exchange action during NaCl modification.

3.5. X-Ray Diffraction Analysis. X-ray examination of the different samples showed (Figure 5) that modifications of stellerite did not damage the stellerite structure that is characterized by the main peaks at 2θ equal to 9.759° which can be assigned as {020}. The characteristic XRD peaks of anatase were observed at $2\theta = 25.352^\circ, 37.784^\circ, 48.072^\circ, 53.928^\circ, \text{ and } 55.115^\circ$ for TiO_2 supported on modified stellerite, which can be assigned as {101}, {004}, {200}, {105}, and {221}. No significant rutile peak was found, showing that rutile phase did not form on the surface of stellerite.

TABLE 1: The parameters of stellerite porous structures by nitrogen adsorption/desorption method.

Sample	Specific surface area (m^2/g)			Pore volume (cm^3/g)		Pore size (nm)	
	S_{BET}	S_m	S_e	V_{BET}	V_{BJH}	D_{BET}	D_{BJH}
Natural	2.2	1.1	1.1	0.0045	0.0096	8.2	38.7
0.4AcMS	67.9	53.7	14.2	0.0363	0.0088	2.1	10.2
0.2AIMS	18.0	1.5	16.5	0.0570	0.1244	12.7	41.0
1.0SMS	33.1	23.9	9.2	0.0216	0.0154	2.6	10.4

$S_m = S_{t\text{-plot}}$ (micropore area); $S_e = S_{t\text{-plot}}$ (external surface area).

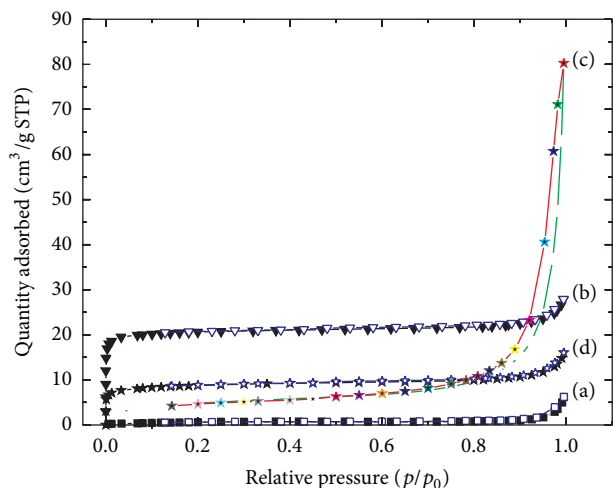


FIGURE 4: Low temperature of adsorption/desorption isotherms of nitrogen on different samples: (a) natural stellerite, (b) 0.4AcMS, (c) 0.2AIMS, and (d) 1.0SMS.

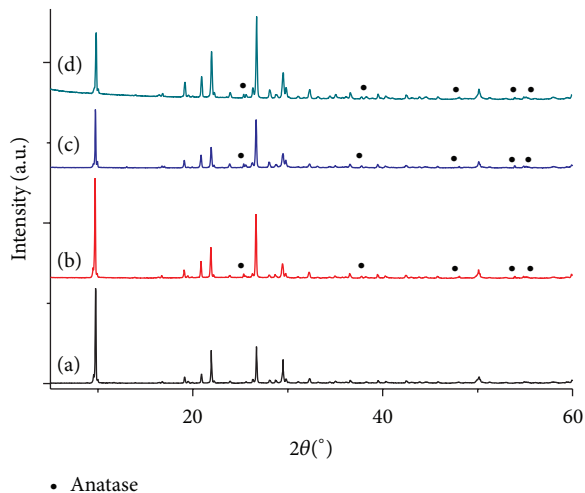


FIGURE 5: XRD patterns of (a) natural stellerite, (b) 0.4TiO₂/AcMS, (c) 0.2TiO₂/AlMS, and (d) 1.0TiO₂/SMS. The ratio of TiO₂ : modified stellerite was fixed to 28 : 100.

3.6. Photocatalytic Activity. Figure 6 shows the relationship between MO degradation and irradiation time for different TiO₂ loaded samples at 2 g/L of photocatalyst. Photocatalytic activity of natural stellerite was also studied as comparison. It was found that natural stellerite has no photocatalytic

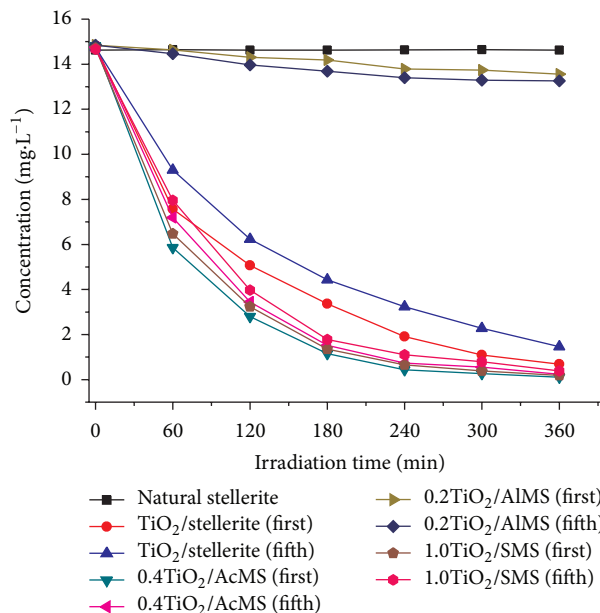


FIGURE 6: MO photocatalytic degradation with prolonged irradiation time.

activity on MO degradation under UV irradiation. MO degradation rates increased with irradiation time using either TiO₂/stellerite or TiO₂ load modified stellerite. After 180 min of irradiation, MO degradation rates were 77.60%, 92.33%, and 91.00% using TiO₂/stellerite, 0.4TiO₂/AcMS, and 1.0TiO₂/SMS as photocatalyst. The results show that photocatalytic activity of TiO₂ is improved by HCl and NaCl modification of stellerite. The photocatalyst was recycled after filtration and heating treatment at 100°C for 12 h and 200°C for 2 h in every cycle. After four cycles, MO orange degradation rates decreased from 77.60%, 92.33%, and 91.00% to 70.47%, 89.86%, and 88.13%, respectively. The slight decrease of photocatalytic activity was due to TiO₂ loss from the surface of stellerite and the fouling of the photocatalyst by byproducts during degradation.

On the contrary, the photocatalytic activity of 0.2TiO₂/AlMS was also disappeared due to the follow reasons: First, the porous structure of stellerite was damaged to some extent by NaOH; second, the photocatalysts agglomerate together to form larger clusters due to the viscous silicates; third, the transparency of the solution was decreased by silicates.

4. Conclusions

- (1) TiO₂ was dispersed using sol-gel method on the surfaces of stellerite treated by HCl, NaOH, or NaCl.
- (2) The S_{BET} value of stellerite was increased by modification. D_{BET} of natural stellerite, 0.4AcMS, 0.2AIMS, and 1.0SMS was 8.2, 2.1, 12.7, and 2.6 nm, respectively. HCl and NaCl modification stimulate the production of micropores, and the surface of stellerite appeared to dissolve by NaOH modification.
- (3) The photocatalytic activity of 0.4TiO₂/AcMS and 1.0TiO₂/SMS was better than that of natural stellerite. The composite photocatalyst had excellent photocatalytic activity after four recycles.

Conflict of Interests

The authors declare that there is no conflict of interests regarding the publication of this paper.

Acknowledgments

The authors would like to acknowledge support from the Key Projects in the National Science & Technology Pillar Program during the Twelfth Five-year Plan Period (Grant no. 2013BAC16B04).

References

- [1] Y. Tian, H. Li, L. P. Li et al., "In-situ integration of microbial fuel cell with hollow-fiber membrane bioreactor for wastewater treatment and membrane fouling mitigation," *Biosensors & Bioelectronics*, vol. 64, pp. 189–195, 2015.
- [2] A. G. D. Prasad and M. A. Abdullah, "Biosorption of Cr(VI) from synthetic wastewater using the fruit shell of gulmohar (*delonix regia*): application to electroplating wastewater," *BioResources*, vol. 5, no. 2, pp. 838–853, 2010.
- [3] D. Pokhrel and T. Viraraghavan, "Treatment of pulp and paper mill wastewater—a review," *Science of the Total Environment*, vol. 333, no. 1–3, pp. 37–58, 2004.
- [4] Ö. Kerkez and İ. Boz, "Photodegradation of methylene blue with Ag₂O/TiO₂ under visible light: operational parameters," *Chemical Engineering Communications*, vol. 202, no. 4, pp. 534–541, 2015.
- [5] N. Mahmoud, T. Ahmed, O. Shinichi, and S. Masaaki, "Biological hydrogen production from starch wastewater using a novel up-flow anaerobic staged reactor," *BioResources*, vol. 8, no. 4, pp. 4951–4968, 2013.
- [6] M. Pérez, F. Torrades, J. Peral et al., "Multivariate approach to photocatalytic degradation of a cellulose bleaching effluent," *Applied Catalysis B: Environmental*, vol. 33, no. 2, pp. 89–96, 2001.
- [7] L. Chen and B. Yan, "Multi-color luminescence of hybrids based with lanthanide functionalized zeolite A and titania," *Colloid and Polymer Science*, vol. 293, no. 6, pp. 1847–1853, 2015.
- [8] M. R. Espino-Estévez, C. Fernández-Rodríguez, O. M. González-Díaz, J. A. Navío, D. Fernández-Hevia, and J. M. Doña-Rodríguez, "Enhancement of stability and photoactivity of TiO₂ coatings on annular glass reactors to remove emerging pollutants from waters," *Chemical Engineering Journal*, vol. 279, pp. 488–497, 2015.
- [9] D. C. L. Vasconcelos, E. H. M. Nunes, A. C. S. Sabioni, P. M. P. Vasconcelos, and W. L. Vasconcelos, "Optical characterization of 316L stainless steel coated with sol-gel titania," *Journal of Non-Crystalline Solids*, vol. 358, no. 22, pp. 3042–3047, 2012.
- [10] Z. H. Gao, Z. D. Cui, S. L. Zhu, Y. Q. Liang, Z. Y. Li, and X. J. Yang, "Design and synthesis of MWN/Ts-TiO₂ nanotube hybrid electrode and its supercapacitance performance," *Journal of Power Sources*, vol. 283, pp. 397–407, 2015.
- [11] A. J. Wang, W. Yu, Y. Fang et al., "Facile hydrothermal synthesis and optical limiting properties of TiO₂-reduced graphene oxide nanocomposites," *Carbon*, vol. 89, pp. 130–141, 2012.
- [12] M.-C. Silaghi, C. Chizallet, and P. Raybaud, "Challenges on molecular aspects of dealumination and desilication of zeolites," *Microporous and Mesoporous Materials*, vol. 191, pp. 82–96, 2014.
- [13] Z. Liang and J. R. Ni, "Improving the ammonium ion uptake onto natural zeolite by using an integrated modification process," *Journal of Hazardous Materials*, vol. 166, no. 1, pp. 52–60, 2009.

Research Article

New Insights into Benzene Hydrocarbon Decomposition from Fuel Exhaust Using Self-Support Ray Polarization Plasma with Nano-TiO₂

Tao Zhu,¹ Wenjuan Zhao,¹ Wenjing Zhang,² Ni Xia,¹ and Xiaoyang Li¹

¹School of Chemical & Environmental Engineering, China University of Mining & Technology-Beijing, Ding 11, Xueyuan Road, Haidian District, Beijing 100083, China

²Chinese Academy for Environmental Planning, No. 8, Dayangfang Road, Chaoyang District, Beijing 100012, China

Correspondence should be addressed to Tao Zhu; bamboo@cumtb.edu.cn

Received 17 June 2015; Revised 11 August 2015; Accepted 3 September 2015

Academic Editor: Hao Tang

Copyright © 2015 Tao Zhu et al. This is an open access article distributed under the Creative Commons Attribution License, which permits unrestricted use, distribution, and reproduction in any medium, provided the original work is properly cited.

A new insight into self-support ray polarization (SSRP) of nonthermal plasma for benzene hydrocarbon decomposition in fuel exhaust was put forward. A wire-tube dielectric barrier discharge (DBD) AC plasma reactor was used at atmospheric pressure and room temperature. The catalyst was made of nano-TiO₂ and ceramic raschig rings. Nano-TiO₂ was prepared as an active component by ourselves in the laboratory. Ceramic raschig rings were selected for catalyst support materials. Then, the catalyst was packed into nonthermal plasma (NTP) reactor. Six aspects, benzene initial concentration, gas flux, electric field strength, removal efficiency, ozone output, and CO₂ selectivity on benzene removal efficiency, were investigated. The results showed SSRP can effectively enhance benzene removal efficiency. The removal efficiency of benzene was up to 99% at electric field strength of 12 kV/cm. At the same time, SSRP decreases ozone yield and shows a better selectivity of CO₂ than the single technology of nonthermal plasma. The final products were mostly CO, CO₂, and H₂O. Our research will lay the foundation for SSRP industrial application in the future.

1. Introduction

Since 1997, after the use of unleaded gasoline, gasoline composition and chemical composition of automobile emissions in Beijing have changed. Now, automobile exhaust pollutants mainly consist of the mixtures of fuel evaporation and incomplete combustion products. Lu et al. [1] established the source component spectrum of automobile exhaust and the spectrum of gasoline vapor and liquid gasoline volatile organic compounds (VOCs), including gasoline, diesel, and liquefied petroleum gas (LPG) as the fuel by sampling on site and the data normalization processing method. It was found that benzene, toluene, xylene, 1,2,4-trimethyl benzene, and other aromatic compounds have higher proportion in gasoline and diesel exhaust. Some researchers have found that some membranes like CNT membranes could be used to filtrate benzene hydrocarbon [2]. Aromatic volatile organic compounds, due to their toxicity and harm on the atmospheric environment,

attract widespread concern of scholars at home and abroad [3–6].

In recent years, nanometer photocatalysis processes for VOCs decomposition have received considerable attention because of low energy consumption, high efficiency, and no secondary pollution. Photochemical reactor is the core equipment of photocatalysis process, and solid phase photocatalytic oxidation reactor and fixed bed reactor are mainly used at present. However, these reactors cannot deal well with VOCs from automobile emission so far. Therefore, how to improve ideal photocatalysis reactor has become the key for VOCs decomposition.

The author uses self-support ray polarization (SSRP) of nonthermal plasma (NTP) for benzene hydrocarbon removal in fuel exhaust. A wire-tube dielectric barrier discharge (DBD) AC plasma reactor was used at atmospheric pressure and room temperature. The catalyst was made of nano-TiO₂ and ceramic raschig rings. Nano-TiO₂ was prepared as an

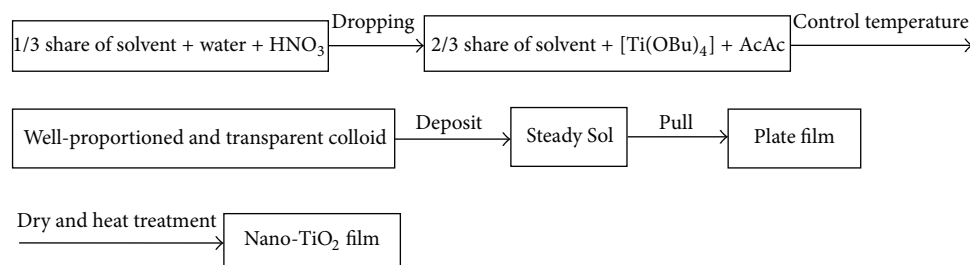


FIGURE 1: Flow chart on preparing nano-TiO₂ thin film by Sol-Gel method.

active component by us in the laboratory. Ceramic raschig rings were selected for catalyst support materials. Then, the catalyst was packed into nonthermal plasma (NTP) reactor [7].

When imposing external voltage on plasma reactor's discharge electrode, a mess of micro discharges will be generated along with gas discharge. These micro discharges come with a certain amount of ultraviolet. Once the photocatalyst was packed into NTP reactor, these ultraviolet lights would activate the photocatalysts with gas discharge happening to treat gaseous VOCs. Ceramic raschig rings, as the main carrier of nano-TiO₂ photocatalyst, lead to chemical reactions in the photocatalyst surface. SSRP generated with plasma happens to promote the photocatalytic reaction. Plasma and photocatalyst work together to improve the removal efficiency of the gaseous pollutants. So SSRP has a better degradation effect than general fixed bed reactor.

2. Materials and Methods

2.1. Materials Preparation. Nano-TiO₂ films were prepared by the Sol-Gel method in the experiment [8]. Flow chart on preparing nano-TiO₂ thin film by Sol-Gel method is given in Figure 1.

Precursor solution is as follows: 1 mol tetrabutyl titanate (precursor substance) + 12 mol ethanol (solvent) + 1.2 mol acetylacetonate (chelating reagent).

Droplet solution is as follows: 6 mol ethanol (solvent) + 1 mol HNO₃ (catalyzer) + 2.5 mol distilled water.

Droplet solution was dropped slowly into the original solution at 35°C and the whole solution was mixed well together. The steady Sol would be obtained, and then the Sol should be deposited at least 24 hours. The packed materials (i.d. 5 mm, thickness 3 mm, length 10 mm, raschig ceramic ring) must be washed by microwave cleaning apparatus before they were immersed into the Sol. Later, the packed materials were pulled out from the Sol at the speed of 1.5 mm/s to get the nanometer TiO₂ film. The packed materials with nanometer film would be dried at 80°C for one hour before they were put into a muffle furnace to calcine at 450~600°C for two hours. At last, the film gradually refrigerated to ambient temperature [9].

In this experiment, we plated nano-TiO₂ thin film on the surface of ceramic raschig rings 3 times, and the weight of nano-TiO₂ thin film was 0.003 g/cm². Ceramic raschig ring was selected with length of 1 cm and wall thickness of 1 mm

and inner diameter of 5 mm as catalyst carrier. The structure of ceramic raschig ring is tested by X-Ray Diffraction (XRD) and can be seen in Table 1.

2.2. NTP System. The NTP system consisted of a tube-wire packed-bed reactor system, an AC power supply, a continuous flow gas supplying system, and an electric and gaseous analytical system. The schematic diagram of NTP system is shown in Figure 2. Dry air (78% N₂, 21% O₂) was used as a balance gas for benzene decomposition. Air supplied from an air compressor was divided into two air flows with each flow rate controlled by a mass flow controller (MFC). One dry air flow was introduced into a bottle of liquid benzene to produce saturated benzene. The vapor was then mixed with the other dry air flow in a blender so that benzene waste gas was diluted to a desired concentration. The voltage and current waves were measured by oscilloscope (Tektronix 2014). The voltage applied to the reactor was sampled by a 12500:1 voltage divider. Also, the current was determined from the voltage drop across a shunt resistor ($R_3 = 10\text{ k}\Omega$) connected in series with the grounded electrode. In order to obtain the total charge and discharge power, simultaneously, a capacitor ($C_m = 2\text{ }\mu\text{F}$) was placed instead of the shunt resistor. The electrical power provided to the discharge was measured using the Q - V Lissajous diagram. The power source used in the experiment is high voltage alternate current power supply whose frequency is 50 Hz, ranging from 0 to 30 kV.

The NTP packed-bed reactor was shown in Figure 3. The coaxial cylindrical NTP reactor was made of an organic-glass tube with an inner diameter of 50 mm and wall thickness of 5 mm wrapped by a copper mesh of 50 cm in length as a ground electrode. A tungsten wire (1.5 mm in diameters) placed on the axis of NTP reactor served as the inner discharge electrode. The relative humidity of 25% in NTP reactor was controlled by a thermohygrometer.

2.3. Detect Methods. Adapt the production to benzene gas concentration detected by Gas Chromatography-Mass Spectrometer (produced by American Thermos Finnegan, TRACE-MS) matching hydrogen flame ion detector (FID); minimum detection quantity can reach 10–15 g. Chromatographic column is 30 m long, with inner diameter 0.32 mm and DB-1 nonpolar capillary column. Choose iodine quantity method to determine ozone concentration. Use Tektronix TDS2014 type oscilloscope to measure discharge parameters in experiment process. Use Lissajous method to determine

TABLE 1: Physics characteristics of the packed material raschig ceramic ring.

Quartz	Component/%		Interstitial rate %	Hygroscopic coefficient %	Volume density (g·cm ⁻³)	Hole rate %
	Al ₂ O ₃	Noncrystal				
15	35	50	9.4	5.9	2.17	12.7

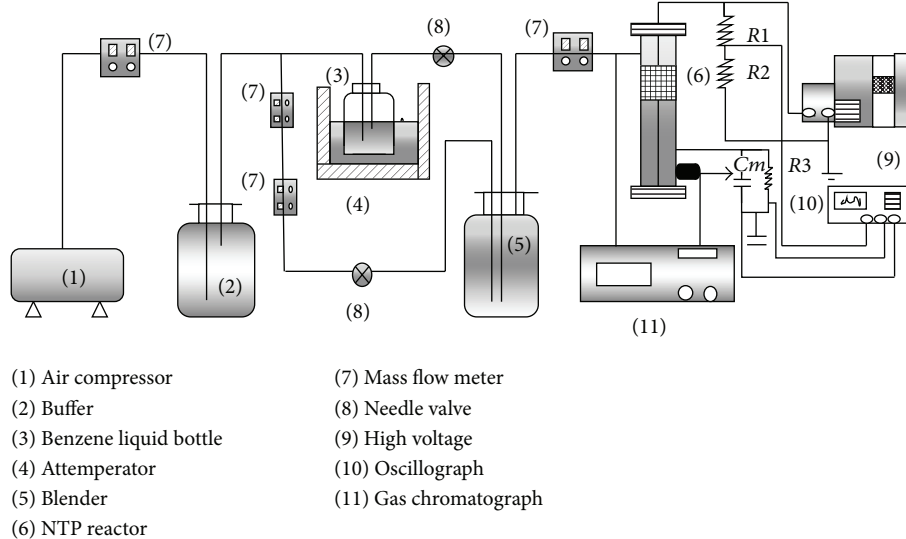


FIGURE 2: Schematic diagram of NTP system for benzene removal.

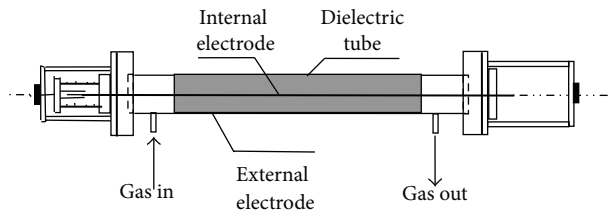


FIGURE 3: NTP reactor. Reactor: organic-glass tube (i.d. 32 mm, packed infilling length of packed materials of 200 mm); internal electrode: tungsten filament (i.d. 0.5 mm); external electrode: dense steel mesh.

discharge power. Use the domestic SC-1001 type Gas Chromatograph to detect CO₂ and CO content in final product, matching hydrogen flame ion detector (FID); methanation converter is connected to the detection top, the minimum detection quantity is 10–12 g, and linear range is 10⁷. The surface characteristic of TiO₂ samples was detected by XRD.

Evaluation standard of benzene degradation effect is evaluated by the following calculation equations:

$$\eta = \frac{C_0 - C}{C_0} \times 100\% \quad (1)$$

$$s_{\text{CO}_2} = \frac{C_{\text{CO}_2}}{n \times (C_0 - C)} \times 100\%. \quad (2)$$

In (1), η represents removal efficiency of the benzene, %; C_0 represents benzene gas inlet mass concentration, mg/m³; C is the mass concentration of outlet benzene, mg/m³. In (2),

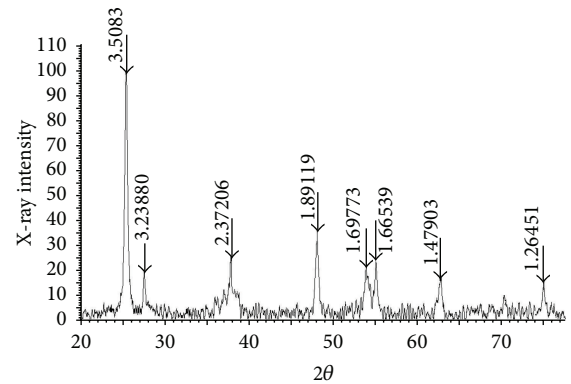
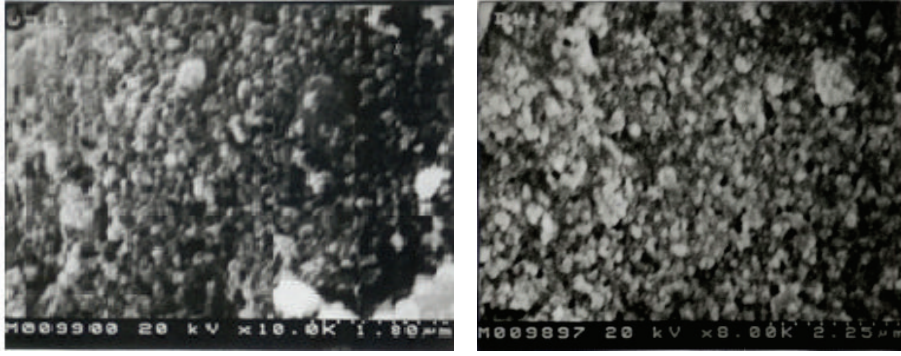


FIGURE 4: XRD of nano-titania.

s_{CO_2} represents the selectivity of CO₂ after benzene degradation reaction, %; C_{CO_2} represents the quality concentration after reaction, mg/m³; and n represents the carbon atom number VOCs molecule contains.

3. Results and Discussion

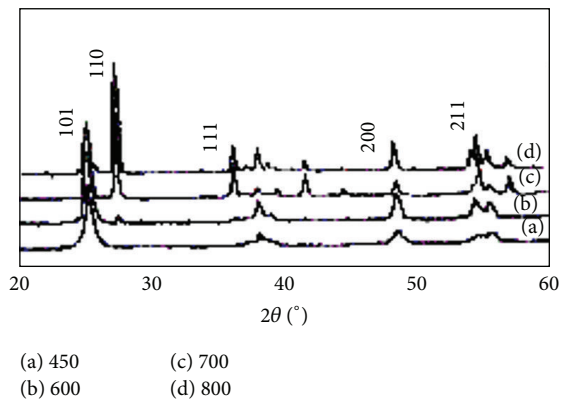
3.1. Characterization of Nano-TiO₂. To carry out XRD phase analysis for prepared TiO₂ samples, XRD spectra are shown in Figure 4. There are two kinds of crystal of rutile and anatase in the phase because of heat treatment temperature of 600°C for TiO₂ photocatalyst preparation. The mass ratio of anatase crystal and rutile crystal is 17:3, and anatase crystal is the main component of TiO₂ catalysts [10]. At the same time,

FIGURE 5: SEM micrograph of TiO₂.

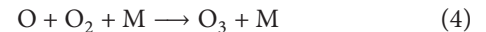
XRD detected results show that the average particle size of anatase crystals of TiO₂ is 28.7 nm, and the average particle size of rutile crystal of TiO₂ is 35.1 nm.

The nanometer TiO₂ thin film was inspected and analyzed by Scan Electric Mirror (SEM, made in Japan, S-2700). The results of SEM micrograph showed that average particulate diameters of TiO₂ were less than 100 nm. SEM micrograph of the samples is referred to in Figure 5.

3.2. Effect of Self-Support Photocatalytic on Removal Efficiency of Benzene. Figure 7 shows the relationship between electric field strength and removal efficiency with or without catalysts. Benzene removal efficiency is increased to over 80%, and removal efficiency increases 10% with catalyst compared to that without catalyst in the conditions of benzene concentration (C_0) of 600 mg/m³ and electric field strength (E) of 9 kV/cm. Benzene is triggered not only to form C₆H₅[•] but to form short carbon chain radicals and molecular fragments. Medium stops free radicals, such as [•]OH, [•]O from oxidizing C₆H₅[•], molecular fragment, short carbon chain, and CO. Some of the free radicals generated from reactants in the strong electric field happen to be composited again after the reaction zone, so that oxidation of benzene is incomplete. If catalyst was added in the reaction zone, these free radicals as well as oxygen free radical are absorbed on the surface of the catalyst before compositing inactivation. Oxidation reaction occurs further, and the removal efficiency is higher with catalyst than the single DBD. At lower electric field strength, corona discharge is weak within reactor, and corona discharge district concentrates only near corona feeder. At this time, ultraviolet rays discharged are weaker, and the function of TiO₂ photocatalyst is weaker. The active free radicals produced by discharging are limited to the surroundings of corona district and cannot react collaboratively with the catalyst of packing surface beyond the corona district. So benzene removal efficiency is approximate with or without catalyst. When electric field strength is gradually enhanced and corona district expands, ultraviolet rays discharged are enhanced and catalytic activity gradually increases. It is obvious that benzene removal efficiency increases. When the electric field strength rises up to a certain degree, catalyst is fully activated, and removal efficiency of benzene tends to be stable.

FIGURE 6: The result of TiO₂ thin film by heat treatment.

3.3. Effect of Self-Support Photocatalytic on Ozone Generation. Figure 8 shows ozone concentration (C_{O_3}) gradually increased with the gas flux (v_{Gas}) increasing. O₂ concentration increases in the air with gas flux increasing. Under high voltage, energetic electrons are throughout the reactor space, and they bombard O₂ molecule to react as follows:



Thus, the ozone concentration is in the upward trend.

It can be also seen from Figure 6 that ozone concentration is lower with catalyst than that without catalysts when benzene gas flux entering the reactor is kept the same. It indicates that TiO₂ photocatalyst has an inhibitory effect on ozone formation. During the removal of benzene, electron-hole pairs are energetic which are from SSRP on the surface of the catalyst. High energy electrons generated in the gases discharge process are preemptively composited with the photo-induced hole to reduce the amount of high energy electron which is used to produce ozone in the air. So ozone yield decreases.

Figure 9 shows the relationship between benzene initial concentration (C_0) and ozone concentration (C_{O_3}) with or without catalyst. It can be seen from Figure 8 that ozone concentration increases with benzene initial concentration

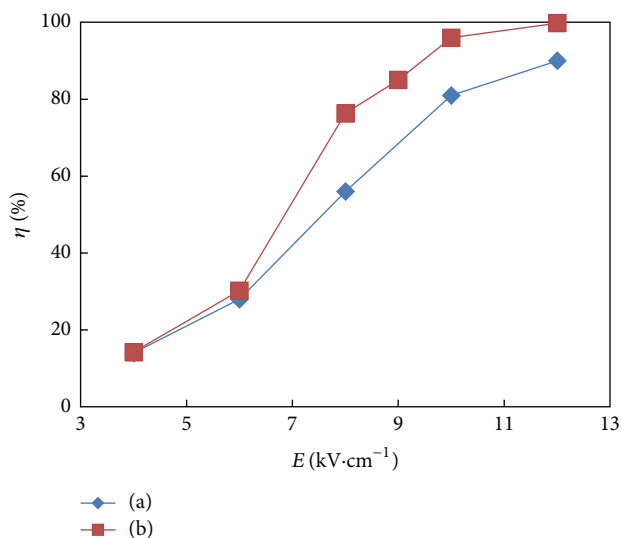


FIGURE 7: Relationship between electric field strength (E) and removal efficiency (η) with or without catalyst ($v_{\text{Gas}} = 100$ L/h; $C_0 = 600$ mg/m³): (a) without catalyst, (b) with catalyst.

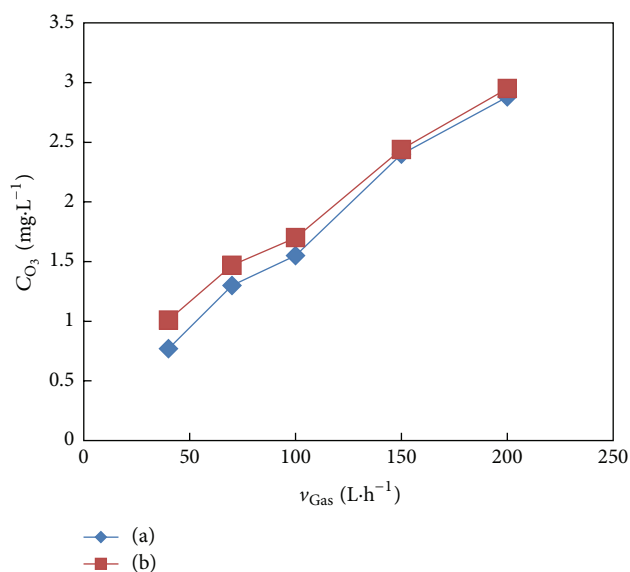


FIGURE 8: Relationship between gas flux (v_{Gas}) and ozone concentration (C_{O_3}) with or without catalyst ($C_0 = 600$ mg/m³; $E = 12$ kV/cm): (a) without catalyst, (b) with catalyst.

decreasing. When C_0 rises, C_6H_6 molecules cost part of the free electrons and free radicals to affect ozone generation. We found that C_6H_6 still exists in emission gas in the case of high O_3 concentrations through Gas Chromatography-Mass Spectrometry (GC-MS). It indicates that O_3 does not react with C_6H_6 directly. That means ozone decomposes into radical fragments firstly, rather than reacting directly with benzene, and free radicals, such as $\cdot\text{OH}$, $\cdot\text{O}$, play a major role as oxidants. This conclusion is supported previously by Assadi et al. [11].

3.4. Effect of Self-Support Photocatalytic on CO_2 and CO Concentration and CO_2 Selectivity. Figure 10 shows

the relationship between electric field strength (E) and CO_2 and CO concentration (C_{CO_2} , C_{CO}) with or without catalyst. C_{CO_2} and C_{CO} increase with the electric field strength increasing. When the electric field strength is 12 kV/cm, C_{CO_2} is 3.5 times higher than C_{CO} . As the field strength increases, energetic electron, O_3 , and other oxidizing radicals increase in the NTP process. At the same time, there are a large amount of electron-hole pairs and $\cdot\text{OH}$, $\cdot\text{O}$ radicals in SSRP process. They work together with benzene molecules to decompose to CO_2 and CO. It was found that when the electric field intensity is higher than 12 kV/cm, except of CO, CO_2 , and H_2O , no other products were found in the emission exhaust through GC-MS.

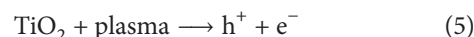
Figure 11 shows the relationship between electric field strength (E) and CO_2 selectivity (s_{CO_2}) with or without photocatalyst. s_{CO_2} increases with the electric field strength increasing. When the electric field strength is 11 kV/cm, s_{CO_2} is 15% higher with catalyst than that without catalyst. It means SSRP is favorable to improving s_{CO_2} . SSRP not only improves the reaction selectivity of benzene molecules in the plasma region and on the surface of the catalyst but also makes byproducts generated in NTP process oxidize into CO, CO_2 in NTP region and on the surface of catalyst finally.

4. Reaction Mechanism

Ultraviolet rays coming from plasma's self-support ray polarization provide a good power source for nanometer photocatalytic materials. When the UV radiates nano- TiO_2 photocatalyst, the catalyst's surface will produce electron and hole which react with O_2 or H_2O adsorbed on the surface, generating OH free radical, as a result, and react with VOC_S [12]. Plasma self-support ray polarization reactor adheres to the following 3 procedures in treatment of VOC_S :

- (1) Energetic electron bombards VOC_S to inspire, ionize, and dissociate chemical bond breaking, thus playing the role of damaging VOC_S .
- (2) There exist large amounts of free radicals and ozone in the plasma, which oxidize VOC_S to generate CO_2 , H_2O , and CO.
- (3) When the UV radiates nano- TiO_2 photocatalyst, the catalyst's surface will produce electron and hole which react with O_2 or H_2O adsorbed on the surface, generating $\cdot\text{OH}$ free radical, as a result, and degraded VOC_S . Chemical reactions are as follows [13].

The wavelength threshold of the light absorbed is 387.5 nm corresponding to TiO_2 band gap of 3.2 eV. When irradiated by the light whose wavelength is less than or equal to 387.5 nm, electron is fired on the valence band to cross the gap band and enter the conduction band [14]. At the same time, the corresponding hole on the valence band produces [15]



Electron-hole pairs have limited life, and they will soon compound the following reaction:



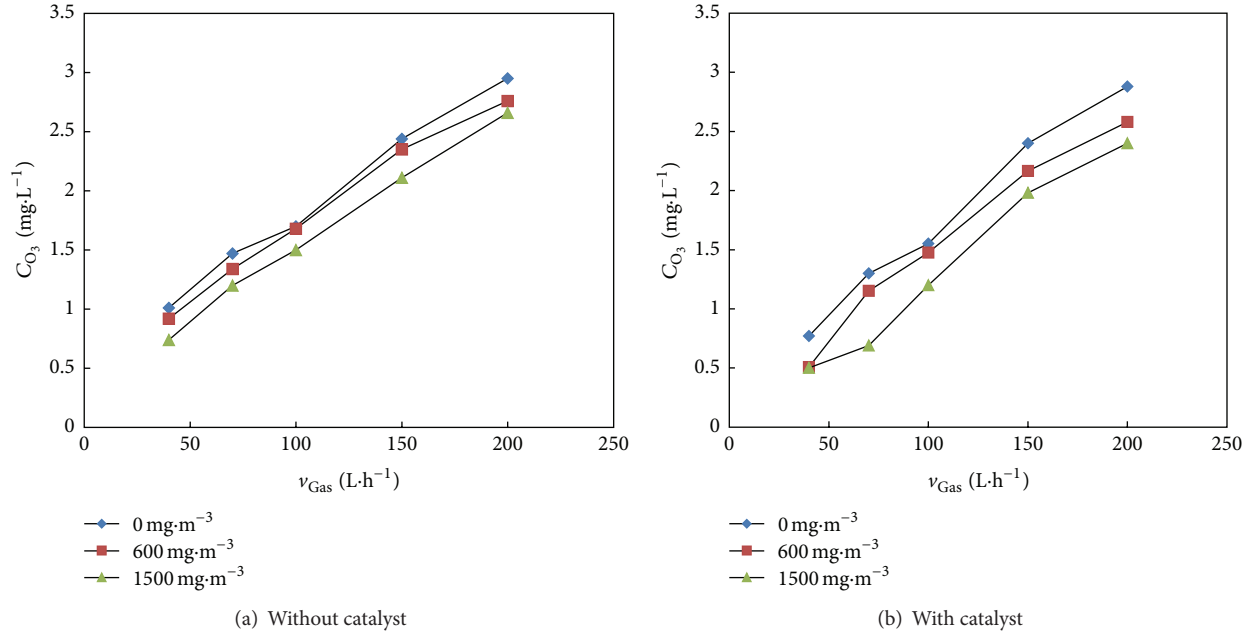


FIGURE 9: Relationship between benzene initial concentration (C_0) and ozone concentration (C_{O_3}) with or without catalyst ($E = 12$ kV/cm).

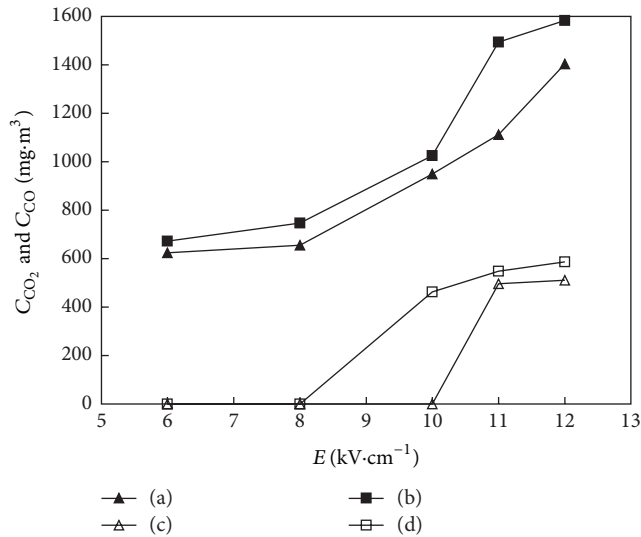


FIGURE 10: Relationship between electric field strength (E) and CO_2 and CO concentration with or without catalyst ($C_0 = 600$ mg/m³, $E = 12$ kV/cm, and $v_{Gas} = 100$ L/h). (a) CO_2 concentration without catalyst, (b) CO_2 concentration with catalyst, (c) CO concentration without catalyst, and (d) CO concentration with catalyst.

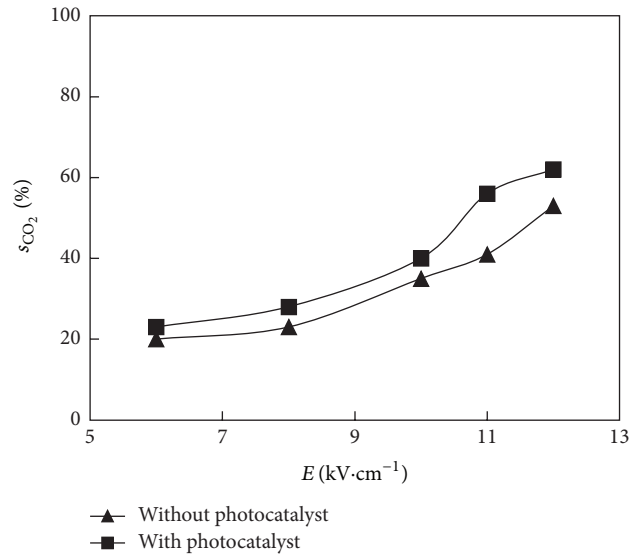
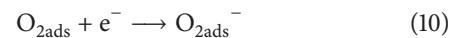


FIGURE 11: Relationship between electric field strength (E) and CO_2 selectivity (s_{CO_2}) with or without photocatalyst ($C_0 = 600$ mg/m³, $E = 12$ kV/cm, and $v_{Gas} = 100$ L/h).

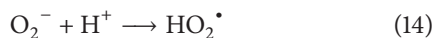
Photo-induced hole can be captured by the water or hydroxyl adsorbed on the surface of catalyst and then produce $\cdot OH$ free radicals:



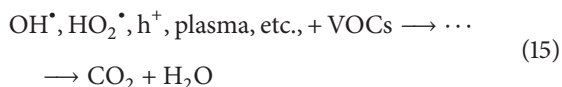
Photo-induced electron is mainly captured by oxygen adsorbed on the surface of catalyst:



Part of photo-induced hole can be captured by oxygen adsorbed on the surface of catalyst at the same time:



OH^\bullet , HO_2^\bullet , h^+ , plasma, and so forth, as the strongest oxidizing oxidants, join some other free radicals to affect VOCs:



5. Conclusions

The authors use SSRP of NTP for benzene hydrocarbon removal in fuel exhaust. A wire-tube dielectric barrier discharge (DBD) AC plasma reactor was used at atmospheric pressure and room temperature. The catalyst was made of nano-TiO₂ and ceramic raschig rings. Nano-TiO₂ was prepared as an active component by ourselves in the laboratory. Ceramic raschig rings were selected for catalyst support materials. Based on a series of experiments, we draw the following conclusions:

- (1) SSRP increases with external electric field strength increasing. When electric field strength is 12 kV/cm, benzene removal efficiency is up to 99%.
- (2) Ozone is a typical byproduct in the NTP process. SSRP shows inhibitory effects on the generation of ozone.
- (3) C_{CO_2} , C_{CO} , and s_{CO_2} increase with the electric field strength increasing in the products. SSRP shows a good characteristic to improve s_{CO_2} and to promote benzene removal efficiency.

Conflict of Interests

The authors declare that there is no conflict of interests regarding the publication of this paper.

Authors' Contribution

T. Zhu and W. J. Zhang contributed to this work as corresponding authors and they conceived and designed the experiments; W. J. Zhao, X. Ni, and X. Y. Li performed the experiments; T. Zhu and W. J. Zhao analyzed the data; W. J. Zhang contributed reagents/materials/analysis tools; and W. J. Zhao wrote the paper.

Acknowledgments

This work was supported by Special Research Funds for Environmental Protection Public Welfare (no. 201409004), the National Natural Science Foundation of China (no.

51108453), Program for New Century Excellent Talents in University (no. NCET120967), Beijing Outstanding Talent Training Project (no. 2012ZG81), and the Fundamental Research Funds for the Central Universities (no. 2009QH03). Thanks are due to Dr. Annie Zeng in West Virginia University for providing language help and for proofreading the paper.

References

- [1] S. H. Lu, Y. H. Bai, and G. S. Zhang, "Study on characteristics of VOCs source profiles of vehicle exhaust and gasoline emission," *Acta Scientiarum Naturalium Universitatis Pekinensis*, vol. 39, pp. 507–511, 2003.
- [2] A. Saha, C. M. Jiang, and A. A. Martí, "Carbon nanotube networks on different platforms," *Carbon*, vol. 79, no. 1, pp. 1–18, 2014.
- [3] A. M. Vandembroucke, M. Mora, C. Jiménez-Sanchidrián et al., "TCE abatement with a plasma-catalytic combined system using MnO₂ as catalyst," *Applied Catalysis B: Environmental*, vol. 156–157, pp. 94–100, 2014.
- [4] T. Zhu, R. Chen, N. Xia et al., "Volatile organic compounds emission control in industrial pollution source using plasma technology coupled with F-TiO₂/γ-Al₂O₃," *Environmental Technology*, vol. 36, pp. 1405–1413, 2015.
- [5] F. Rahmani, M. Haghghi, and P. Estifae, "Synthesis and characterization of Pt/Al₂O₃-CeO₂ nanocatalyst used for toluene abatement from waste gas streams at low temperature: conventional vs. plasma-ultrasound hybrid synthesis methods," *Microporous and Mesoporous Materials*, vol. 185, pp. 213–223, 2014.
- [6] T. Zhu, J. Li, W. Liang, and Y. Jin, "Synergistic effect of catalyst for oxidation removal of toluene," *Journal of Hazardous Materials*, vol. 165, no. 1–3, pp. 1258–1260, 2009.
- [7] T. Zhu, D. Y. Xu, X. W. He et al., "Decomposition of benzene in dry air by super-imposed barrier discharge nonthermal plasma-photocatalytic system," *Fresenius Environmental Bulletin*, vol. 19, no. 7, pp. 1275–1282, 2010.
- [8] H. B. Zhang, K. Li, T. H. Sun, J. Jia, Z. Lou, and L. Feng, "Removal of styrene using dielectric barrier discharge plasmas combined with sol-gel prepared TiO₂ coated γ-Al₂O₃," *Chemical Engineering Journal*, vol. 241, pp. 92–102, 2014.
- [9] T. Zhu, L. Lu, Y. Dai et al., "Preparation for nano-titania catalyst and its application for benzene decomposition," *Nature Environment and Pollution Technology*, vol. 12, no. 4, pp. 675–678, 2013.
- [10] K. Zhang, X. F. Du, M. B. Katz et al., "Creating high quality Ca:TiO₂-B (CaTi₅O₁₁) and TiO₂-B epitaxial thin films by pulsed laser deposition," *Chemical Communications*, vol. 51, no. 41, pp. 8584–8587, 2015.
- [11] A. A. Assadi, J. Palau, A. Bouzaza, J. Peña-Roja, V. Martínez-Soriac, and D. Wolbert, "Abatement of 3-methylbutanal and trimethylamine with combined plasma and photocatalysis in a continuous planar reactor," *Journal of Photochemistry and Photobiology A: Chemistry*, vol. 282, pp. 1–8, 2014.
- [12] J. Palau, A. A. Assadi, J. M. Peña-Roja, A. Bouzaza, D. Wolbert, and V. Martínez-Soria, "Isovaleraldehyde degradation using UV photocatalytic and dielectric barrier discharge reactors, and their combinations," *Journal of Photochemistry and Photobiology A: Chemistry*, vol. 299, pp. 110–117, 2015.

- [13] D. Lopatik, D. Marinov, O. Guaitella, A. Rousseau, and J. Röpcke, "On the reactivity of plasma-treated photo-catalytic TiO_2 surfaces for oxidation of C_2H_2 and CO ," *Journal of Physics D: Applied Physics*, vol. 46, no. 25, pp. 203–208, 2013.
- [14] B. Dou, F. Bin, C. Wang, Q. Jia, and J. Li, "Discharge characteristics and abatement of volatile organic compounds using plasma reactor packed with ceramic Raschig rings," *Journal of Electrostatics*, vol. 71, no. 5, pp. 939–944, 2013.
- [15] A. A. Assadi, A. Bouzaza, C. Vallet, and D. Wolbert, "Use of DBD plasma, photocatalysis, and combined DBD plasma/ photocatalysis in a continuous annular reactor for isovaleraldehyde elimination—synergetic effect and byproducts identification," *Chemical Engineering Journal*, vol. 254, pp. 124–132, 2014.

Research Article

Experimental Study on the Deactivating Effect of KNO_3 , KCl , and K_2SO_4 on Nanosized Ceria/Titania SCR Catalyst

Xiongbo Chen,^{1,2} Ping Fang,^{1,2} Wenhao Zeng,^{1,2} Kunyuan Liu,³
Zhixiong Tang,^{1,2} and Chaoping Cen^{1,2}

¹South China Institute of Environmental Sciences, The Ministry of Environmental Protection of PRC, No. 7 West Street, Yuancun, Guangzhou 510655, China

²The Key Laboratory of Water and Air Pollution Control of Guangdong Province, No. 7 West Street, Yuancun, Guangzhou 510655, China

³School of Chemical Engineering and Technology, Tianjin University, Tianjin Weijin Road, No. 92, Nankai District 300072, China

Correspondence should be addressed to Chaoping Cen; cenchaoping@scies.org

Received 29 June 2015; Revised 24 August 2015; Accepted 25 August 2015

Academic Editor: Bao Yu Xia

Copyright © 2015 Xiongbo Chen et al. This is an open access article distributed under the Creative Commons Attribution License, which permits unrestricted use, distribution, and reproduction in any medium, provided the original work is properly cited.

Nanosized Ce/TiO_2 is effective in selective catalytic reduction of NO with NH_3 . The NO conversion of Ce/TiO_2 is 93% at 370°C . However, addition of potassium using KNO_3 , KCl , or K_2SO_4 as precursors effectively deactivates Ce/TiO_2 . NO conversion at 370°C is reduced to 45%, 24%, and 16% after addition of KNO_3 , KCl , and K_2SO_4 , respectively, with a controlled K/Ce molar ratio at 0.25. The deactivation may be attributed to the changes in the structural and chemical state of ceria and the degradation of surface acidity. The transformation of amorphous ceria into ceria crystals after potassium addition, together with the decrease of surface defects, is also determined. Oxygen diffusion in the process of ceria reduction is slow, and the redox cycle is slowed down. Moreover, the surface acid sites are markedly destroyed, leading to the reduced capacity of ammonia adsorption. These results may provide useful information for the application and life management of $\text{CeO}_2/\text{TiO}_2$ in potassium-rich environments such as biofuel-fired boilers.

1. Introduction

Selective catalytic reduction (SCR) of NO with ammonia is the most efficient and reliable technology to remove NO_x from stationary sources. $\text{V}_2\text{O}_5(\text{WO}_3)/\text{TiO}_2$ or $\text{V}_2\text{O}_5(\text{MoO}_3)/\text{TiO}_2$ catalysts are widely used in the SCR process. These vanadium-based catalysts are highly efficient. However, V_2O_5 is an ecotoxic material that is harmful to the environment [1]. To replace vanadium-based catalysts, environment-friendly, nonvanadium catalysts such as Ce/TiO_2 , $\text{Mn}_2\text{Nb}_1\text{O}_x$, MnO_x - CeO_y , Fe-ZSM-5, Cu-ZSM-5, and FeTiO_x have been developed in the past years [2–8].

Recently, Ce/TiO_2 catalyst has gained recognition because of its excellent activity and selectivity. Xu et al. reported that Ce/TiO_2 catalyst is highly efficient at 275 – 400°C , and the undesired by-product, N_2O , could be hardly detected [3]. Gao et al. compared three preparation methods, namely, single step sol-gel method, impregnation method,

and coprecipitation method, and found that the Ce/TiO_2 catalysts prepared using the single step sol-gel method had the best SCR activity and SO_2 resistance. Liu et al. demonstrated the feasibility of a supercritical water synthesis route in the syntheses of Ce/TiO_2 catalysts by a strong metal-support interaction [9]. Chen et al. found that tungsten modification could further improve the activity of Ce/TiO_2 [10], and Liu et al. used MoO_3 modification to enhance this activity. Chen et al. investigated a series of ceria catalysts supported on titanates with various morphologies and structures, including nanoparticle, nanotube, fragment, nanowire, and nanorod; the investigation revealed a good SCR performance of the former three catalysts. Moreover, Ce/TiO_2 -based catalysts have been commercially produced in rare earth-rich regions such as Shandong, China, and utilized in de NO_x facilities in power plants.

While nonvanadium SCR catalysts were developed, the deactivation of SCR catalysts by alkali metals and alkaline

earth metals has gained popularity. This problem has been proven to be more serious in biofuel boilers because alkali metal content is higher in biofuels than in coal. For vanadium-based catalysts, many studies in literature noted the decrease of surface acidity by potassium, sodium, and calcium compounds, and a few works found the interaction between poison and vanadium sites [11, 12]. Moreover, Strege et al. proposed that the blocking of surface pores is an important reason for this observation. As for Fe-ZSM-5, Kern et al. attributed alkali deactivation to the decreased capability of ammonia adsorption [13]. Similar results of Fe- and Cu-based catalysts supported on TiO₂ or ZrO₂ were reported by Kustov et al. [14]. With respect to CeO₂/TiO₂ catalysts, Wang et al. investigated the significant deactivation by sodium and calcium salts and proposed a deactivation mechanism based on the change of the ceria state [15]. Some other catalysts, such as Cu-SAPO-34 and MnO_x/TiO₂, also encountered a similar deactivation [16, 17]. Considering the extensive knowledge of alkali deactivation of various catalysts, the application of SCR technology to the purification of biofuel flue gas is questionable.

In this paper, we investigated the poisoning effect of various potassium compounds on nanosized Ce/TiO₂ catalysts in the SCR application. KCl and K₂SO₄ were selected as the precursors of potassium because the potassium content is very high in the flue gas of boilers firing biofuels, and Cl and S elements always coexist [18, 19]. KNO₃ was selected as the precursors of potassium oxide. Fresh and K-poisoned Ce/TiO₂ catalysts were subjected to a range of characterizations (e.g., XRD, XPS, NH₃-TPD, and H₂-TPR), and the deactivation mechanism was discussed.

2. Experimental

2.1. Preparation of Ce/TiO₂ Catalyst. Commercially produced P25 TiO₂ (Degussa, Germany) was used as the catalyst support. Cerous nitrate (AR, Ce(NO₃)₃·6H₂O) was used as the precursor of ceria. Ceria was loaded on P25 TiO₂ using the wet-impregnation method with a controlled Ce/Ti molar ratio of 1:19. In summary, P25 was impregnated in a cerous nitrate solution, and the mixture was stirred for 4 h, dried at 80°C for 12 h, and calcined at 450°C for 3 h.

2.2. Addition of Potassium Compounds. As described in previous reports, adding potassium in various concentrations was always conducted by the wet-impregnation method to simulate the poisoning mechanism of potassium in real flue gas at laboratory [16, 20]. In this paper, KNO₃, KCl, and K₂SO₄ were dissolved in distilled water and impregnated with Ce/TiO₂ catalysts. The mixture was stirred vigorously for 4 h, dried at 80°C for 12 h, and calcined at 450°C for 3 h. The K/Ce molar ratio was controlled at 0.25, 0.5, 1, and 2. The prepared catalysts were denoted as Ce/TiO₂-*x*-*y*, where *x* are the precursors (KNO₃, KCl, and K₂SO₄) and *y* is the K/Ce molar ratios (0.25, 0.5, 1, and 2).

2.3. SCR Activity Evaluation. SCR activities on fresh and K-poisoned Ce/TiO₂ catalysts were tested in a fixed-bed reactor. The typical reactant gas composition was as follows: 750 ppm

NO, 750 ppm NH₃, 1.5% H₂O, 3.5% O₂, and balanced N₂. The catalyst dosage was 0.5 g. The gas hourly space velocity (GHSV) was approximately 100,000 h⁻¹. NO, NO₂, and O₂ concentrations were monitored by a flue gas analyzer (KM9106, Quintox Kane International Limited). N₂O was detected by a FT-IR gas analyzer (Madur Photon Portable IR Gas Analysers, Madur Ltd., Austria).

2.4. Characterization Methods. XRD analysis was performed using X-ray diffraction with Cu Kα radiation (model D/max RA, Rigaku Co., Japan). The data were collected for scattering angles (2θ) ranging between 5° and 80° with a step size of 0.02°. X-ray photoelectron spectroscopy with Al Kα X-ray (hν = 1486.6 eV) radiation operated at 150 W (XPS: Thermo ESCALAB 250, USA) was used to investigate the surface properties and probe the electronic state of the elements. The microstructures were observed using a scanning electron micrograph (SEM) in a Phillips XL-30-ESEM system with a voltage of 15 kV. Nitrogen adsorption-desorption isotherms were obtained using a nitrogen adsorption apparatus (ASAP 2020, USA). All the samples were degassed at 200°C prior to measuring. The Brunauer-Emmett-Teller (BET) specific surface area (SBET) was determined by a multipoint BET method using the adsorption data in the relative pressure (*P*/*P*₀) range from 0.05 to 0.30. Temperature programmed desorption with ammonia (NH₃-TPD) and temperature programmed reduction with hydrogen (H₂-TPR) experiments were carried out using a TP-5080 instrument (Tianjin Xianquan Industry and Trade Development Co. Ltd., China). Prior to the NH₃-TPD experiments, 100 mg samples were pretreated in pure N₂ at 350°C for 1 h and then saturated with anhydrous NH₃ (4% in N₂) at room temperature. Desorption was carried out by heating the samples in N₂ (30 mL/min) from 70°C to 800°C with a heating rate of 10°C/min. Before raising the temperature, a preheat treatment at 70°C for 1 h was conducted. For the TPR experiments, 50 mg samples were pretreated in pure N₂ at 350°C for 1 h and cooled to 70°C. The H₂-TPR runs were carried out with a linear heating rate of 10°C/min from 70°C to 800°C in H₂ (4% in N₂).

3. Results and Discussion

3.1. SCR Performance. Figures 1–3 show NO conversions as a function of the reaction temperature over catalysts with different loading amounts of KNO₃, KCl, and K₂SO₄, respectively. The fresh Ce/TiO₂ catalyst shows good catalytic activity in the temperature range of 285°C to 460°C. The NO conversion reaches up to 93% at 370°C. However, the NO conversion rapidly decreases after adding potassium. When the K/Ce molar ration exceeds 0.25, NO conversion becomes negligible in the entire temperature range regardless of the precursors. Relatively, the addition of KCl or K₂SO₄ is more harmful to the SCR activity of Ce/TiO₂ than that of KNO₃. The NO conversion at 370°C in Ce/TiO₂-KNO₃-0.25 is consistent at 45%, but it is kept at 16% and 24% in Ce/TiO₂-K₂SO₄-0.25 and Ce/TiO₂-KCl-0.25, respectively.

To find the internal reasons for the deactivation by potassium salts, Ce/TiO₂, Ce/TiO₂-KNO₃-0.25, Ce/TiO₂-K₂SO₄-0.25, and Ce/TiO₂-KCl-0.25 were subjected to a range

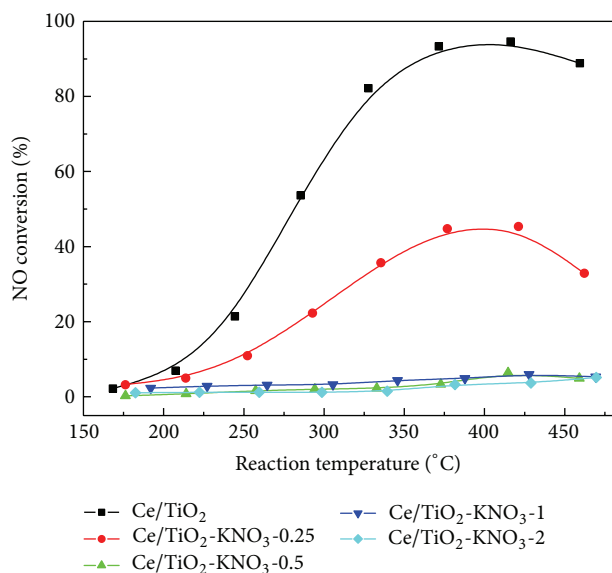


FIGURE 1: Variation of NO conversion with reaction temperature of catalysts with different KNO_3 loading.

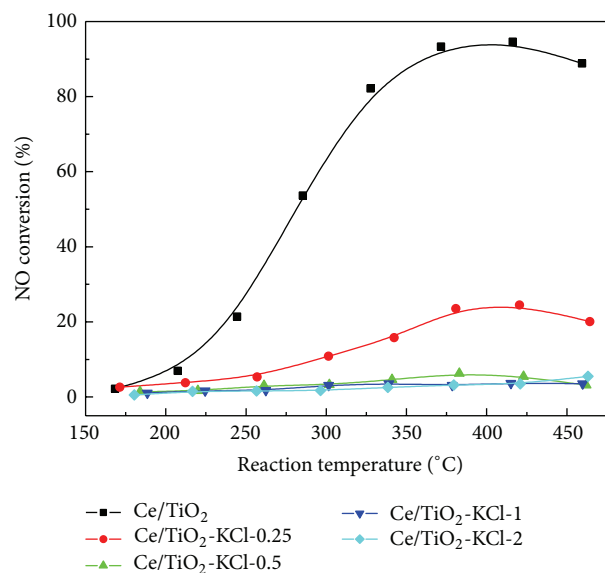


FIGURE 3: Variation of NO conversion with reaction temperature of catalysts with different KCl loading.

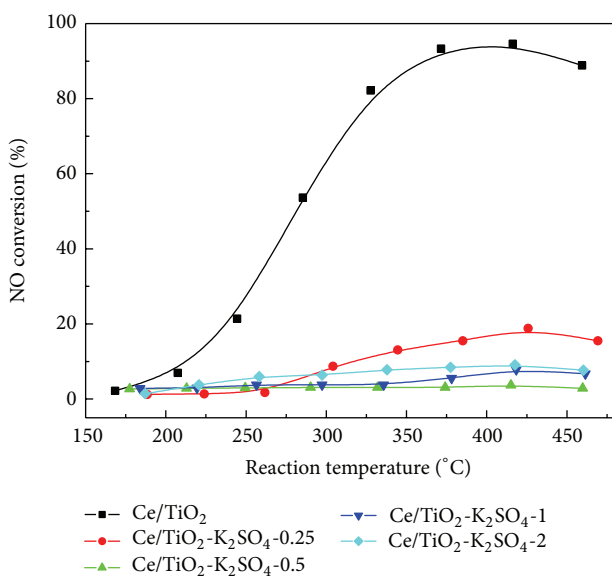
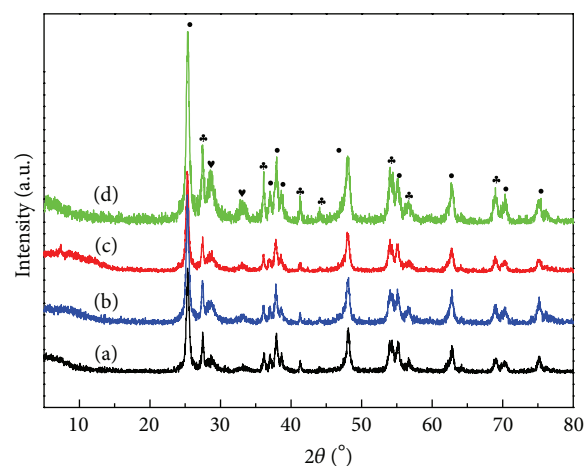


FIGURE 2: Variation of NO conversion with reaction temperature of catalysts with different K_2SO_4 loading.



(d) $\text{Ce/TiO}_2\text{-KCl-0.25}$ • Anatase
(c) $\text{Ce/TiO}_2\text{-KNO}_3\text{-0.25}$ * Rutile
(b) $\text{Ce/TiO}_2\text{-K}_2\text{SO}_4\text{-0.25}$ ▼ CeO_2
(a) Ce/TiO_2

FIGURE 4: Powder XRD patterns of fresh and K-poisoned Ce/TiO_2 catalysts.

of characterizations including XRD, BET-BJH, XPS, NH_3 -TPD, and H_2 -TPR.

3.2. Crystal Structure and Morphology. The powder XRD patterns of fresh and K-poisoned Ce/TiO_2 catalysts are shown in Figure 4. Characterization peaks in the anatase phase (PDF-number 21-1272, $2\theta = 25.28^\circ, 37.80^\circ, 48.05^\circ, 53.89^\circ, 55.06^\circ,$ and 62.69°) and rutile phase (PDF-number 21-1276, $2\theta = 27.45^\circ, 36.09^\circ,$ and 54.32°) appear in all the four catalysts. The characterization peaks of ceria (PDF-number 43-1002, $2\theta = 28.55^\circ, 33.08^\circ, 47.48^\circ,$ and 56.33°) are not noticeable in Ce/TiO_2 but become clear after adding potassium. As described in

Experimental, the Ce/Ti molar ratio was designed at 1:19; hence the weight percentage of ceria in the Ce/TiO_2 catalyst is approximately 10% which is above the detection limit of XRD. As such, the changes of ceria peaks suggest that highly dispersing amorphous ceria as very small nanoparticles is the dominant structure of ceria in the fresh Ce/TiO_2 catalyst but transforms into ceria crystals in the K-poisoned catalysts. The particle size of ceria, which is calculated by plane [111] using the Scherrer Equation, grows to 7.6–7.9 nm in the three K-poisoned catalysts. Notably, the intensity of ceria peaks follows the following sequence: $\text{Ce/TiO}_2\text{-KCl-0.25} > \text{Ce/TiO}_2\text{-K}_2\text{SO}_4\text{-0.25} > \text{Ce/TiO}_2\text{-KNO}_3\text{-0.25}$, indicating that

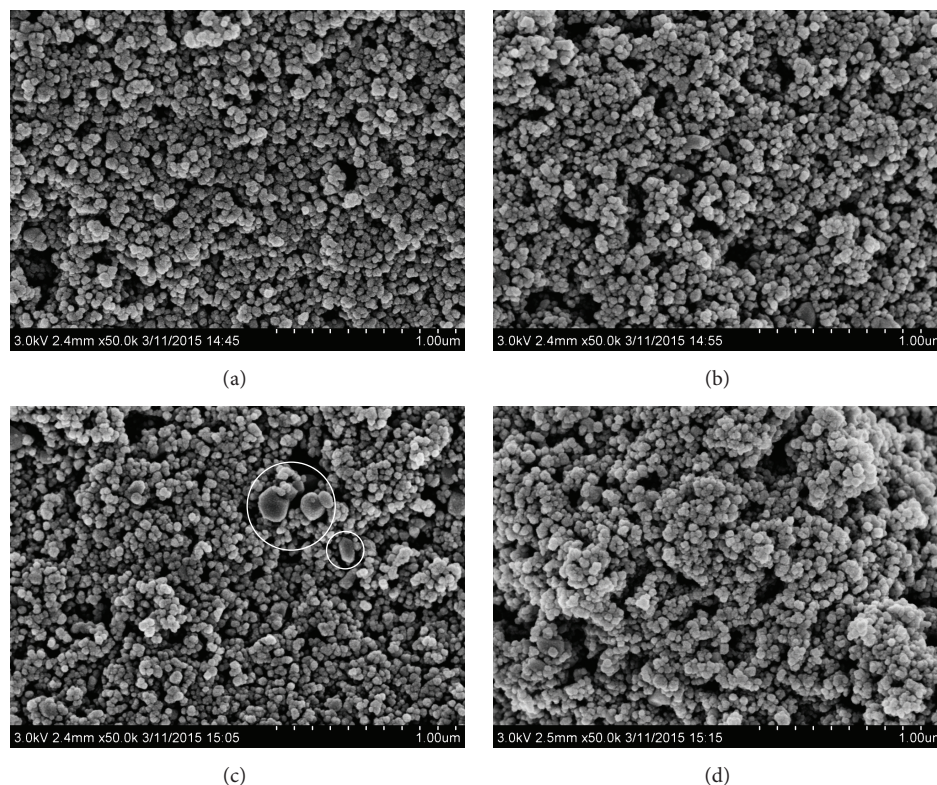


FIGURE 5: SEM images of Ce/TiO₂ (a), Ce/TiO₂-KNO₃-0.25 (b), Ce/TiO₂-KCl-0.25 (c), and Ce/TiO₂-K₂SO₄-0.25 (d).

the crystallinity of ceria in the three catalysts may also follow the same order.

Microstructures of the fresh and K-poisoned Ce/TiO₂ catalysts observed by SEM are shown in Figure 5. The surface of fresh Ce/TiO₂ catalyst is smooth when viewed through SEM (Figure 5(a)). The aggregation of particles cannot be observed. However, different degrees of aggregation can be observed in K-poisoned catalysts. Interstices between particles are enlarged. Variant large particles appear in the SEM image of Ce/TiO₂-KCl-0.25. Considering the highest intensities of ceria and titania XRD peaks in Ce/TiO₂-KCl-0.25, the destructive effect of KCl may have possibly occurred on ceria and titania particles. High-grade aggregation was observed in Ce/TiO₂-K₂SO₄-0.25, and the surface becomes bumpy like heaped-up hills. Microstructures indicate that the dispersion of constituent particles worsened in K-poisoned catalysts, especially in KCl- and K₂SO₄-poisoned catalysts.

Morphology, structure, and particle size of the fresh and K-poisoned Ce/TiO₂ catalysts further observed by TEM are shown in Figure 6. Aggregation can also be observed in K-poisoned catalysts like SEM images. Some ceria particles are circled in red. A small number of ceria particles can be observed in the fresh Ce/TiO₂ catalyst. However, in K-poisoned catalysts, the number of ceria particles increases significantly, and overgrowth of ceria particles occurs in Ce/TiO₂-KCl-0.25 and Ce/TiO₂-K₂SO₄-0.25. The obvious difference in the number of ceria particles between fresh and K-poisoned Ce/TiO₂ catalysts further confirms the increasing crystallization of ceria after K-loading. The TEM

results are in good agreement with the XRD and SEM discussions. Therefore, the transformation of highly dispersing amorphous ceria to worse dispersing ceria crystals is certain.

3.3. Physical Characterizations. Table 1 shows the physical characterizations including BET surface area, pore volume, and average pore diameter. Compared with the BET surface area, pore volume, and average pore diameter of Ce/TiO₂, those of Ce/TiO₂-K₂SO₄-0.25 reduced slightly, indicating that part of the K₂SO₄ may deposit on the catalyst surface and cover a few pores. For Ce/TiO₂-KCl-0.25 and Ce/TiO₂-KNO₃-0.25, the BET surface areas are reduced further, pore volumes are not reduced, and average pore diameters slightly increased, suggesting that a few pores agglomerate and enlarge along with the growth of ceria crystals. All the changes mentioned in the physical characterizations accorded well with the microstructures showed by SEM. Notably, the changes in physical characterizations were slight. Hence adding potassium has very limited effect on the physical characterizations of Ce/TiO₂. The changes in physical characterizations are not the primary reason for deactivation.

3.4. Surface Species. The surface atomic concentrations of Ce, Ti, O, K, Cl, and S acquired with XPS are shown in Table 2. As revealed by XRD, highly dispersed amorphous ceria transforms into ceria crystals after adding potassium. Generally, amorphous ceria interacts closely with the TiO₂ support; however ceria crystals are more independent and tend to agglomerate. Hence the surface atomic concentrations

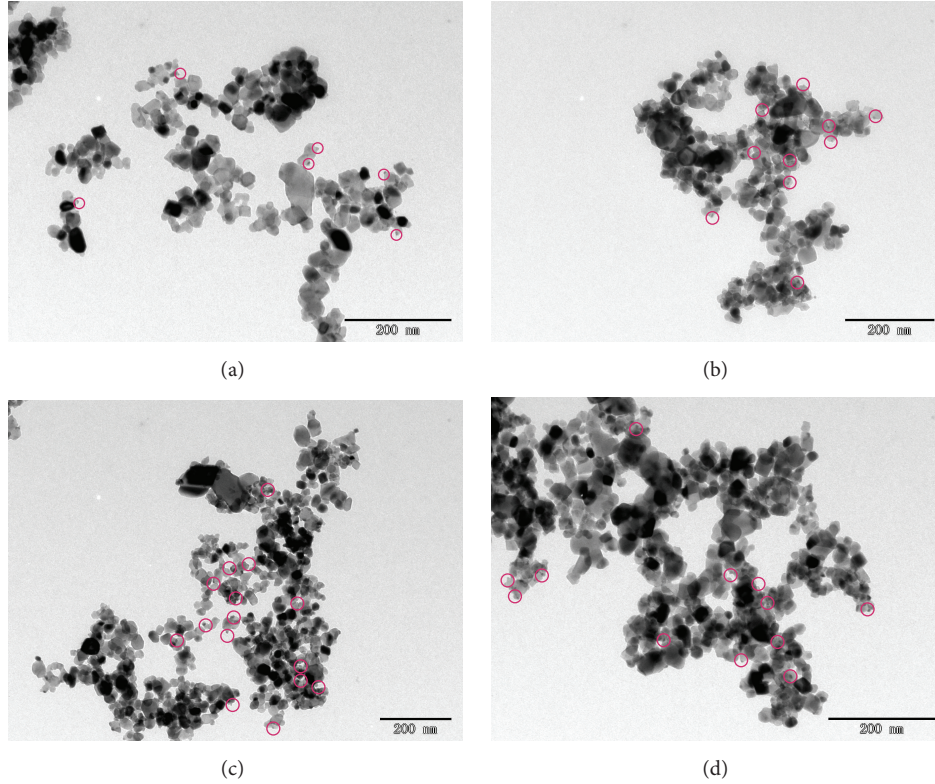


FIGURE 6: TEM images of Ce/TiO_2 (a), $\text{Ce}/\text{TiO}_2\text{-KNO}_3\text{-0.25}$ (b), $\text{Ce}/\text{TiO}_2\text{-KCl-0.25}$ (c), and $\text{Ce}/\text{TiO}_2\text{-K}_2\text{SO}_4\text{-0.25}$ (d).

TABLE 1: BET surface area, pore volume, and average pore diameter.

Sample	BET surface area (m^2/g)	Pore volume (cm^3/g)	Average pore diameter (nm)
Ce/TiO_2	45.9	0.40	28.55
$\text{Ce}/\text{TiO}_2\text{-KNO}_3\text{-0.25}$	42.8	0.40	30.57
$\text{Ce}/\text{TiO}_2\text{-K}_2\text{SO}_4\text{-0.25}$	45.0	0.39	28.03
$\text{Ce}/\text{TiO}_2\text{-KCl-0.25}$	41.7	0.41	31.59

TABLE 2: Surface atomic concentrations of various elements acquired with XPS.

Sample	Ce	Ti	O	K	Cl	S
Ce/TiO_2	1.86	31.60	66.54	—	—	—
$\text{Ce}/\text{TiO}_2\text{-KNO}_3\text{-0.25}$	2.01	32.22	65.00	0.76	—	—
$\text{Ce}/\text{TiO}_2\text{-KCl-0.25}$	2.13	31.49	64.92	0.99	0.47	—
$\text{Ce}/\text{TiO}_2\text{-K}_2\text{SO}_4\text{-0.25}$	2.29	30.41	64.43	1.76	—	1.11

of Ce increase after adding potassium. The atomic concentrations of K, Cl, N, and S gave some evidence of the final form of potassium poisons. N atoms are hardly detected in $\text{Ce}/\text{TiO}_2\text{-KNO}_3\text{-0.25}$, indicating that KNO_3 has decomposed into K_2O . The atomic concentration of the K surface is higher in $\text{Ce}/\text{TiO}_2\text{-K}_2\text{SO}_4\text{-0.25}$ than in $\text{Ce}/\text{TiO}_2\text{-KCl-0.25}$ and $\text{Ce}/\text{TiO}_2\text{-KNO}_3\text{-0.25}$ which may be attributed to the deposition of K_2SO_4 on the surface of $\text{Ce}/\text{TiO}_2\text{-K}_2\text{SO}_4\text{-0.25}$. The atomic concentration of K in $\text{Ce}/\text{TiO}_2\text{-KCl-0.25}$ is more

than twice that of Cl, suggesting that Cl can enter into the catalyst bulk.

The XPS spectra of Ce 3d are shown in Figure 7, where peaks labeled as u, u2, u3, v, v2, and v3 represent the $3d^{10}4f^0$ state of Ce^{4+} species, and those labeled as u1 and v1 represent the $3d^{10}4f^1$ initial electronic state corresponding to Ce^{3+} species [21, 22]. Generally, Ce^{4+} is dominant in fine ceria crystals, and Ce^{3+} accompanied with ceria defects is abundant in small ceria particles such as amorphous ceria. The intensity of Ce^{4+} is always measured in terms of peak area proportion of u3 in the whole spectrum. As shown in Table 3, the peak area proportion of u3 increases after adding potassium. This finding reveals that the concentration of ceria defects is reduced and the XRD results have confirmed the transformation of amorphous ceria into ceria crystals.

The fitted XPS spectra of O 1s are shown in Figure 8. The O 1s peaks mainly contain two different species: crystal lattice oxygen (O_α) and chemisorbed oxygen (O_β) [21, 23, 24]. The O_α peak is located at 529.92 eV in the spectrum of Ce/TiO_2

TABLE 3: Peak areas of the fitted O 1s and Ce 3d XPS spectra.

Sample	Peak area of O 1s			Peak area of Ce 3d		
	O _α	O _β	Proportion of O _β	u3	Whole spectrum	Proportion of u3
Ce/TiO ₂	130585	19085	12.75%	5283	77795	6.79
Ce/TiO ₂ -KNO ₃ -0.25	135300	17500	11.45%	6186	73603	8.40
Ce/TiO ₂ -KCl-0.25	128985	14285	9.97%	6783	80462	8.43
Ce/TiO ₂ -K ₂ SO ₄ -0.25	146085	21501	12.83%	9547	89451	10.67

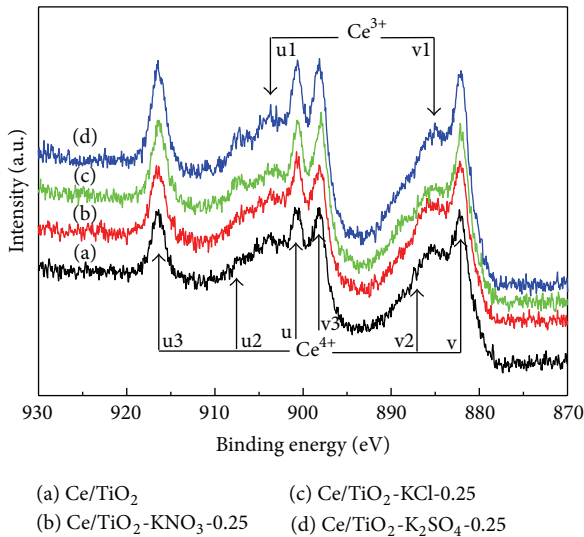


FIGURE 7: XPS spectra of Ce 3d.

but shifts to a lower binding energy in the spectra of K-poisoned catalysts. This shift can often be observed during the transformation of Ce³⁺ into Ce⁴⁺ [21, 23, 24]. Chemisorbed oxygen has been proven to be active in oxidation reactions and will take part in the oxidation of Ce³⁺ to Ce⁴⁺. The concentration of chemisorbed oxygen is assumed to be positively related with the ceria defects. As a result, the concentration of chemisorbed oxygen should decrease after adding potassium addition (see Table 3). The concentrations of chemisorbed oxygen in Ce/TiO₂-KCl-0.25 and Ce/TiO₂-KNO₃-0.25 are lower than that of Ce/TiO₂, as expected. However, the chemisorbed oxygen concentration in Ce/TiO₂-K₂SO₄-0.25 is slightly higher and may be contributed by the SO₄²⁻ groups. As reported by Gao et al., sulfurization treatment could provide new chemisorbed oxygen in the form of -OH or H₂O groups [25].

3.5. Surface Acidity and Reducibility. According to the widely accepted Eley-Rideal and Langmuir-Hinshelwood mechanism of SCR reaction [26, 27], the adsorption of NH₃ on the catalyst surface is considered a prerequisite. The NH₃-TPD profiles of the four catalysts are shown in Figure 9, where the decreased NH₃-desorption can be observed in the K-poisoned samples. The total amount of desorbed ammonia is calculated at 209 μmol/g, 141 μmol/g, 119 μmol/g, and 157 μmol/g over Ce/TiO₂, Ce/TiO₂-KNO₃-0.25, Ce/TiO₂-KCl-0.25, and Ce/TiO₂-K₂SO₄-0.25, respectively, showing a

noticeable decrease. The desorbed ammonia corresponds to the ammonia adsorbed on the Lewis and Brønsted acid sites. Hence these acid sites were partly destroyed by potassium after addition.

It is widely accepted that the reduction of ceria can be divided into two processes: the initial reduction of surface ceria species at low temperature and the further reduction of bulk ceria at high temperature. Considering the XRD and XPS results, we can deduce that amorphous ceria with abundant defects in Ce/TiO₂ tends to be reduced at low temperatures, whereas ceria crystals in K-poisoned catalysts reduce at high temperatures [28, 29]. As depicted in Figure 10, the reduction of ceria starts at 261°C in Ce/TiO₂, and the reduction maximum appears at 487°C. However, the starting temperature shifts to the right at 444°C, 457°C, and 377°C in the profiles of Ce/TiO₂-KNO₃-0.25, Ce/TiO₂-KCl-0.25, and Ce/TiO₂-K₂SO₄-0.25, respectively. This finding demonstrates that the addition of potassium leads to the passivating of ceria, similar to the transformation of amorphous ceria into ceria crystals. Moreover, there are sharp reduction peaks centering at 718°C and 652°C in the H₂-TPR profiles of Ce/TiO₂-KCl-0.25 and Ce/TiO₂-K₂SO₄-0.25, respectively. Similar peaks are not found in the H₂-TPR profile of Ce/TiO₂-KNO₃-0.25, demonstrating that the crystallinity of ceria in Ce/TiO₂-KCl-0.25 and Ce/TiO₂-K₂SO₄-0.25 is higher.

3.6. Deactivation Mechanism. Based on the analysis above, the changes that take place after adding potassium are summarized in Table 4. We can find two main reasons for the deactivation of Ce/TiO₂ catalyst by potassium: the structural and chemical state changes of ceria and the degradation of surface acidity.

In terms of ceria catalysts, good redox behavior in catalysis reactions involves high-speed Ce⁴⁺/Ce³⁺ redox cycles. Previous researches on the redox behavior of ceria have shown that the oxidation of Ce³⁺ to Ce⁴⁺ is very fast, whereas the reduction of Ce⁴⁺ to Ce³⁺ is slow in most cases [30]. Oxygen diffusion that depends on the type, size, and concentration of oxygen vacancies is proposed to be the rate-controlling step of ceria reduction [30–32]. Therefore, the nature of oxygen vacancy highly affects the redox behavior of ceria. It is known that once Ce³⁺ appears, oxygen vacancies will be generated to maintain electrostatic balance [32, 33]. Consequently, ceria defects on the catalyst surface are the most active species with fast Ce⁴⁺/Ce³⁺ redox cycle. For the Ce/TiO₂ catalyst, ceria mainly exists in a highly dispersed amorphous form with surface having abundant defects; hence

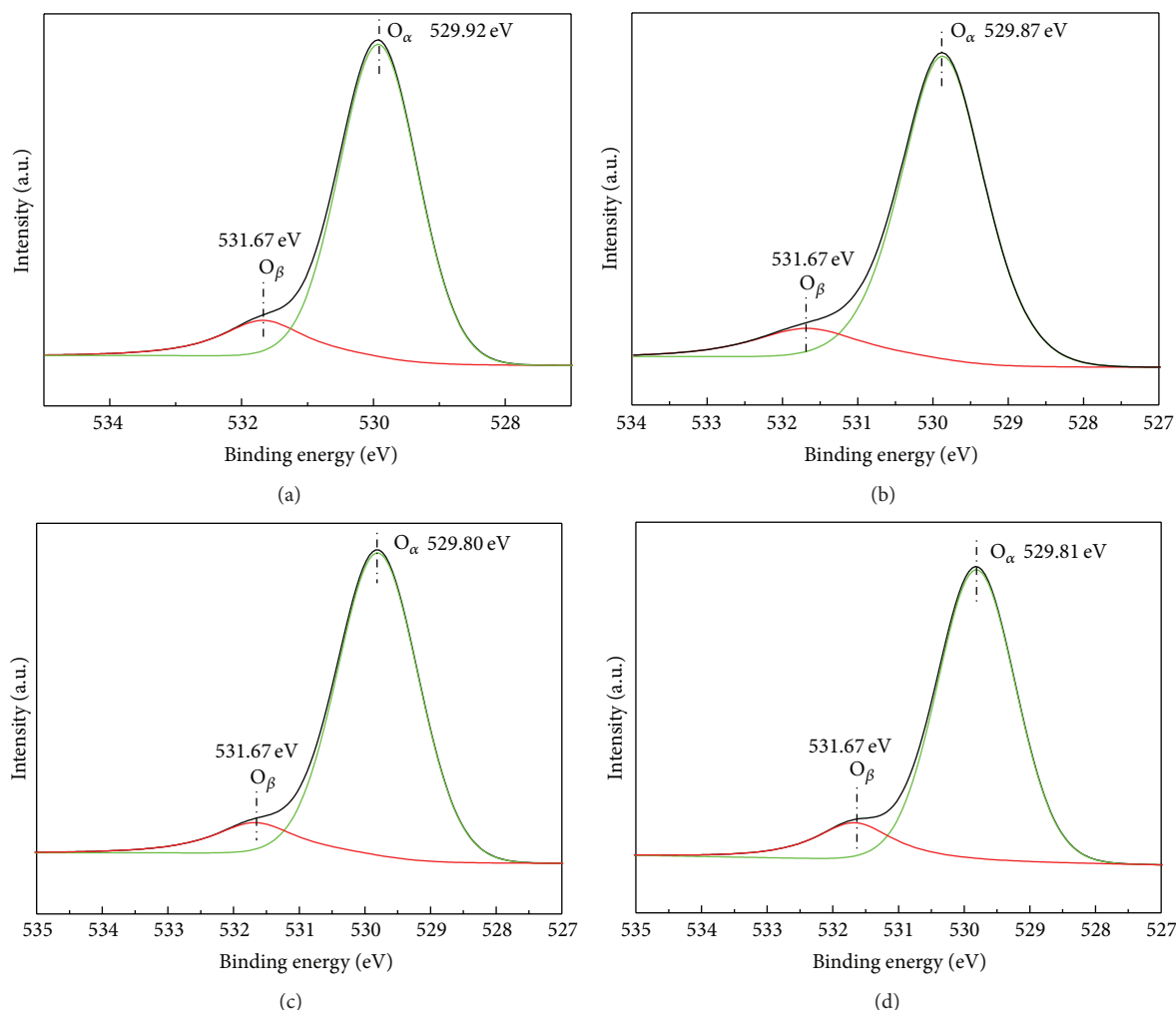


FIGURE 8: XPS spectra of O 1s: (a) Ce/TiO₂, (b) Ce/TiO₂-KNO₃-0.25, (c) Ce/TiO₂-KCl-0.25, and (d) Ce/TiO₂-K₂SO₄-0.25.

TABLE 4: Sum of the property changes after potassium addition.

Sample	Crystal structure of ceria	Microstructure	Chemical state of cerium	Ammonia adsorption	Reducibility of ceria	SCR performance
Ce/TiO ₂ -KNO ₃ -0.25	Amorphous to crystal	Enlarged interstices	Decrease of Ce ³⁺	Reduced NH ₃ adsorption	Passivating of ceria	Deactivation
Ce/TiO ₂ -KCl-0.25	Highest crystallinity	Variant particles	Decreased of Ce ³⁺	Largest decrease of NH ₃ adsorption	Serious passivating of ceria	Serious deactivation
Ce/TiO ₂ -K ₂ SO ₄ -0.25	High crystallinity	High aggregation	Largest decrease of Ce ³⁺	Reduced NH ₃ adsorption	Serious passivating of ceria	Serious deactivation

the reduction of ceria can start at very low temperature (261°C), and the Ce/TiO₂ shows good SCR performance. For K-poisoned catalysts, amorphous ceria transforms into ceria crystals, and the size of ceria particles enlarges. As a result, the amount of surface defects, as well as oxygen vacancies, is reduced which hinders the reduction of ceria in the redox cycle. The reduction of ceria only occurred at higher temperatures. The K-doped catalysts showed the worst

SCR performance. Notably, a more complete transformation of the structural and chemical state of ceria can be observed after adding KCl and K₂SO₄; hence the deactivation by the addition of KCl and K₂SO₄ is more significant than adding KNO₃.

The degradation of the surface acidity is considered a common reason for all the SCR catalysts that underwent alkali deactivation. It is widely accepted that the acid sites on

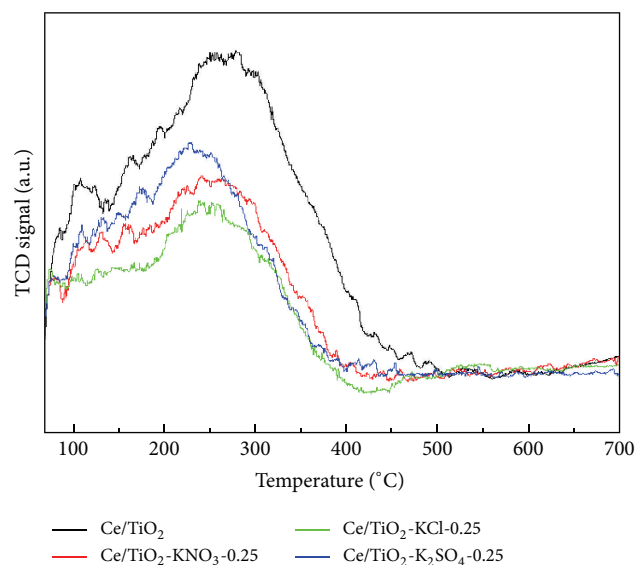


FIGURE 9: NH_3 -TPD profiles of Ce/TiO_2 , $\text{Ce}/\text{TiO}_2\text{-KNO}_3\text{-0.25}$, $\text{Ce}/\text{TiO}_2\text{-KCl-0.25}$, and $\text{Ce}/\text{TiO}_2\text{-K}_2\text{SO}_4\text{-0.25}$.

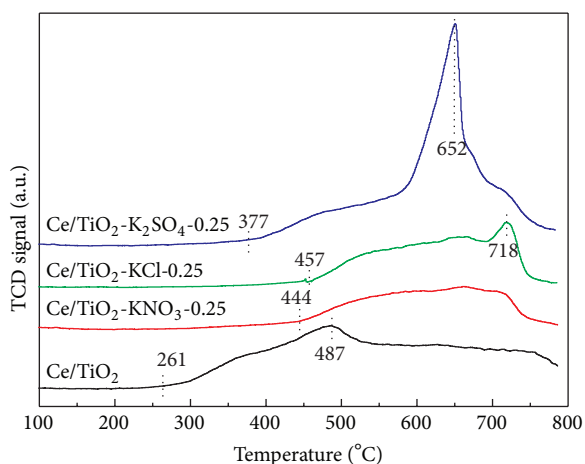


FIGURE 10: H_2 -TPR profiles of Ce/TiO_2 , $\text{Ce}/\text{TiO}_2\text{-KNO}_3\text{-0.25}$, $\text{Ce}/\text{TiO}_2\text{-KCl-0.25}$, and $\text{Ce}/\text{TiO}_2\text{-K}_2\text{SO}_4\text{-0.25}$.

the catalyst surface can be easily destroyed by alkaline species. Hence the decreasing capacity of ammonia adsorption by potassium has always been observed in V-, Fe-, Cu-, and zeolite-based catalysts [11–14, 16, 17]. For the Ce/TiO_2 catalyst, we have found apparent degradation of the surface acidity regardless of the difference of the potassium precursor.

It is interesting to note that the Cl^- and SO_4^{2-} anions have additional poisoning effects. Lisi et al. have reported that acidic HCl can promote the formation of new acid sites on the vanadium-based catalysts [34], indicating that Cl^- may be beneficial to surface acidity. However, this positive effect of Cl^- is not found on KCl-doped $\text{CeO}_2/\text{TiO}_2$ catalyst. In the three catalysts, the largest decrease of NH_3 adsorption is observed in the KCl-doped catalyst. The extra decrease may be associated with Cl^- . From XPS results, we have deduced that Cl^- can enter freely into the catalyst bulk. Cl^- may

combine with Ce to form cerium chloride and destroy the Ce-centered Lewis acid sites. High-grade aggregation of the whole catalyst sample is observed in K_2SO_4 -doped catalysts. The aggregation that attributed to the deposition of K_2SO_4 on catalyst surface will reduce the exposure of active sites for the SCR reaction.

4. Conclusions

The addition of KNO_3 , KCl, and K_2SO_4 could deactivate the Ce/TiO_2 catalyst in a SCR reaction. After adding KNO_3 , KCl, or K_2SO_4 with a K/Ce molar ratio of 0.25, the NO conversion at 370°C dropped sharply from 93% to 45%, 24%, and 16%. Further increase in the amount of potassium led to complete deactivation. Changes in the structural and chemical state of ceria and the degradation of surface acidity were the primary reasons for the deactivation. Ceria particles grew and amorphous ceria transformed into ceria crystals after adding potassium. As a result, the amount of ceria defects as well as oxygen vacancies was reduced which ultimately lowered the rate of ceria reduction and redox cycle. KCl and K_2SO_4 showed greater effect on the changes of ceria state than KNO_3 . Potassium could destroy the acid sites, leading to the decline of ammonia adsorption capability. The introduction of Cl^- from KCl could be combined with Ce to form cerium chloride; hence Ce-centered Lewis acid sites were destroyed by Cl^- . The deposition of K_2SO_4 on catalyst surface will reduce the exposure of active sites for the SCR reaction. Cl and S have always coexisted with K biofuels and their concentrations are always high; thus the deactivation of Ce/TiO_2 utilized in biofuel boilers will be more significant than that in coal-fired boilers.

Conflict of Interests

The authors declare that there is no conflict of interests regarding the publication of this paper.

Acknowledgments

This research is financially supported by the National Natural Science Foundation of China (NSFC-51306068), the Project of the Science and Technology Program of Guangdong Province (2014A020216015), the Special Fund for Environmental Scientific Research in the Public Interest (201509013), the Key Laboratory for Water and Air Pollution Control, Guangdong Province (no. 2011A060901002), and the Central-Level Non-profit Scientific Institutes for Basic R&D Operations.

References

- [1] F. Liu, Y. Yu, and H. He, "Environmentally-benign catalysts for the selective catalytic reduction of NO_x from diesel engines: structure-activity relationship and reaction mechanism aspects," *Chemical Communications*, vol. 50, no. 62, pp. 8445–8463, 2014.
- [2] R. Q. Long and R. T. Yang, "Superior Fe-ZSM-5 catalyst for selective catalytic reduction of nitric oxide by ammonia," *Journal of the American Chemical Society*, vol. 121, no. 23, pp. 5595–5596, 1999.

- [3] W. Xu, Y. Yu, C. Zhang, and H. He, "Selective catalytic reduction of NO by NH₃ over a Ce/TiO₂ catalyst," *Catalysis Communications*, vol. 9, no. 6, pp. 1453–1457, 2008.
- [4] F. Liu, H. He, and C. Zhang, "Novel iron titanate catalyst for the selective catalytic reduction of NO with NH₃ in the medium temperature range," *Chemical Communications*, no. 17, pp. 2043–2045, 2008.
- [5] Z. Lian, F. Liu, H. He, X. Shi, J. Mo, and Z. Wu, "Manganese-niobium mixed oxide catalyst for the selective catalytic reduction of NO_x with NH₃ at low temperatures," *Chemical Engineering Journal*, vol. 250, pp. 390–398, 2014.
- [6] B. Dou, G. Lv, C. Wang, Q. Hao, and K. Hui, "Cerium doped copper/ZSM-5 catalysts used for the selective catalytic reduction of nitrogen oxide with ammonia," *Chemical Engineering Journal*, vol. 270, pp. 549–556, 2015.
- [7] L. Qu, C. Li, G. Zeng et al., "Support modification for improving the performance of MnO_x-CeO_y/γ-Al₂O₃ in selective catalytic reduction of NO by NH₃," *Chemical Engineering Journal*, vol. 242, pp. 76–85, 2014.
- [8] X. Chen, C. Cen, Z. Tang et al., "The key role of pH value in the synthesis of titanate nanotubes-loaded manganese oxides as a superior catalyst for the selective catalytic reduction of NO with NH₃," *Journal of Nanomaterials*, vol. 2013, Article ID 871528, 7 pages, 2013.
- [9] Y. Liu, W. Yao, X. Cao et al., "Supercritical water syntheses of Ce_xTiO₂ nano-catalysts with a strong metal-support interaction for selective catalytic reduction of NO with NH₃," *Applied Catalysis B: Environmental*, vol. 160–161, no. 1, pp. 684–691, 2014.
- [10] L. Chen, J. Li, M. Ge, and R. Zhu, "Enhanced activity of tungsten modified CeO₂/TiO₂ for selective catalytic reduction of NO_x with ammonia," *Catalysis Today*, vol. 153, no. 3–4, pp. 77–83, 2010.
- [11] Y. Zheng, A. D. Jensen, J. E. Johnsson, and J. R. Thøgersen, "Deactivation of V₂O₅-WO₃-TiO₂ SCR catalyst at biomass fired power plants: elucidation of mechanisms by lab- and pilot-scale experiments," *Applied Catalysis B: Environmental*, vol. 83, no. 3–4, pp. 186–194, 2008.
- [12] D. Nicosia, I. Czekaj, and O. Kröcher, "Chemical deactivation of V₂O₅/WO₃-TiO₂ SCR catalysts by additives and impurities from fuels, lubrication oils and urea solution: part II. Characterization study of the effect of alkali and alkaline earth metals," *Applied Catalysis B: Environmental*, vol. 77, no. 3–4, pp. 228–236, 2008.
- [13] P. Kern, M. Klimczak, T. Heinzelmann, M. Lucas, and P. Claus, "High-throughput study of the effects of inorganic additives and poisons on NH₃-SCR catalysts. Part II: Fe-zeolite catalysts," *Applied Catalysis B: Environmental*, vol. 95, no. 1–2, pp. 48–56, 2010.
- [14] A. L. Kustov, S. B. Rasmussen, R. Fehrmann, and P. Simonsen, "Activity and deactivation of sulphated TiO₂- and ZrO₂-based V, Cu, and Fe oxide catalysts for NO abatement in alkali containing flue gases," *Applied Catalysis B: Environmental*, vol. 76, no. 1–2, pp. 9–14, 2007.
- [15] H. Wang, X. Chen, S. Gao, Z. Wu, Y. Liu, and X. Weng, "Deactivation mechanism of Ce/TiO₂ selective catalytic reduction catalysts by the loading of sodium and calcium salts," *Catalysis Science & Technology*, vol. 3, no. 3, pp. 715–722, 2013.
- [16] J. Ma, Z. Si, D. Weng, X. Wu, and Y. Ma, "Potassium poisoning on Cu-SAPO-34 catalyst for selective catalytic reduction of NO_x with ammonia," *Chemical Engineering Journal*, vol. 267, pp. 191–200, 2015.
- [17] Y. Peng, J. Li, W. Si et al., "Ceria promotion on the potassium resistance of MnO_x/TiO₂ SCR catalysts: an experimental and DFT study," *Chemical Engineering Journal*, vol. 269, pp. 44–50, 2015.
- [18] Å. Kling, C. Andersson, Å. Myringer, D. Eskilsson, and S. G. Järås, "Alkali deactivation of high-dust SCR catalysts used for NO_x reduction exposed to flue gas from 100 MW-scale biofuel and peat fired boilers: influence of flue gas composition," *Applied Catalysis B: Environmental*, vol. 69, no. 3–4, pp. 240–251, 2007.
- [19] Y. P. Li, T. J. Wang, C. Z. Wu et al., "Effect of alkali vapor exposure on Ni-MgO/γ-Al₂O₃/cordierite monolithic catalyst for biomass fuel gas reforming," *Industrial & Engineering Chemistry Research*, vol. 49, no. 7, pp. 3176–3183, 2010.
- [20] F. Tang, B. Xu, H. Shi, J. Qiu, and Y. Fan, "The poisoning effect of Na⁺ and Ca²⁺ ions doped on the V₂O₅/TiO₂ catalysts for selective catalytic reduction of NO by NH₃," *Applied Catalysis B: Environmental*, vol. 94, no. 1–2, pp. 71–76, 2010.
- [21] F. Larachi, J. Pierre, A. Adnot, and A. Bernis, "Ce 3d XPS study of composite Ce_xMn_{1-x}O_{2-y} wet oxidation catalysts," *Applied Surface Science*, vol. 195, no. 1–4, pp. 236–250, 2002.
- [22] E. Beche, P. Charvin, D. Perarnau, S. Abanades, and G. Flamant, "Ce 3d XPS investigation of cerium oxides and mixed cerium oxide (Ce_xTi_yO_z)," *Surface and Interface Analysis*, vol. 40, no. 3–4, pp. 264–267, 2008.
- [23] S. Yang, Y. Feng, J. Wan, W. Zhu, and Z. Jiang, "Effect of CeO₂ addition on the structure and activity of RuO₂/γ-Al₂O₃ catalyst," *Applied Surface Science*, vol. 246, no. 1–3, pp. 222–228, 2005.
- [24] S. Yang, W. Zhu, Z. Jiang, Z. Chen, and J. Wang, "The surface properties and the activities in catalytic wet air oxidation over CeO₂-TiO₂ catalysts," *Applied Surface Science*, vol. 252, no. 24, pp. 8499–8505, 2006.
- [25] S. Gao, X. Chen, H. Wang et al., "Ceria supported on sulfated zirconia as a superacid catalyst for selective catalytic reduction of NO with NH₃," *Journal of Colloid and Interface Science*, vol. 394, pp. 515–521, 2013.
- [26] G. Busca, L. Lietti, G. Ramis, and F. Berti, "Chemical and mechanistic aspects of the selective catalytic reduction of NO_x by ammonia over oxide catalysts: a review," *Applied Catalysis B: Environmental*, vol. 18, no. 1–2, pp. 1–36, 1998.
- [27] J. Li, H. Chang, L. Ma, J. Hao, and R. T. Yang, "Low-temperature selective catalytic reduction of NO_x with NH₃ over metal oxide and zeolite catalysts—a review," *Catalysis Today*, vol. 175, no. 1, pp. 147–156, 2011.
- [28] L. Xue, C. Zhang, H. He, and Y. Teraoka, "Catalytic decomposition of N₂O over CeO₂ promoted Co₃O₄ spinel catalyst," *Applied Catalysis B: Environmental*, vol. 75, no. 3–4, pp. 167–174, 2007.
- [29] S. Damyanova, C. A. Perez, M. Schmal, and J. M. C. Bueno, "Characterization of ceria-coated alumina carrier," *Applied Catalysis A: General*, vol. 234, no. 1–2, pp. 271–282, 2002.
- [30] X. Liu, K. Zhou, L. Wang, B. Wang, and Y. Li, "Oxygen vacancy clusters promoting reducibility and activity of ceria nanorods," *Journal of the American Chemical Society*, vol. 131, no. 9, pp. 3140–3141, 2009.
- [31] C. T. Campbell and C. H. F. Peden, "Oxygen vacancies and catalysis on ceria surfaces," *Science*, vol. 309, no. 5735, pp. 713–714, 2005.
- [32] F. Esch, S. Fabris, L. Zhou et al., "Electron localization determines defect formation on ceria substrates," *Science*, vol. 309, no. 5735, pp. 752–755, 2005.

- [33] P. Dutta, S. Pal, M. S. Seehra, Y. Shi, E. M. Eyring, and R. D. Ernst, "Concentration of Ce^{3+} and oxygen vacancies in cerium oxide nanoparticles," *Chemistry of Materials*, vol. 18, no. 21, pp. 5144–5146, 2006.
- [34] L. Lisi, G. Lasorella, S. Malloggi, and G. Russo, "Single and combined deactivating effect of alkali metals and HCl on commercial SCR catalysts," *Applied Catalysis B: Environmental*, vol. 50, no. 4, pp. 251–258, 2004.

Research Article

Influence of Anodic Oxidation Parameters of TiO₂ Nanotube Arrays on Morphology and Photocatalytic Performance

Xiaoyu Zhao, Yuxiang Zhu, Yanfei Wang, Liang Zhu, Libin Yang, and Zuoliang Sha

Tianjin Key Laboratory of Marine Resources and Chemistry, College of Chemical Engineering and Materials Science, Tianjin University of Science and Technology, No. 29, 13th Avenue, TEDA, Tianjin 300457, China

Correspondence should be addressed to Xiaoyu Zhao; xyz@tust.edu.cn and Zuoliang Sha; zsha@tust.edu.cn

Received 18 June 2015; Accepted 9 August 2015

Academic Editor: Cunming Liu

Copyright © 2015 Xiaoyu Zhao et al. This is an open access article distributed under the Creative Commons Attribution License, which permits unrestricted use, distribution, and reproduction in any medium, provided the original work is properly cited.

Titanium dioxide nanotube arrays (TNTAs) were fabricated by electrochemical anodization of Ti foils. The effects of electrolyte, applied voltage, duration of anodic oxidation to morphology, and photocatalytic performance of TNTAs were investigated. TNTAs formed in electrolyte of glycol and DMSO tend to grow along radial direction with flimsy tube wall and weak adhesion on Ti substrate. Those in glycerol, however, easily achieve balance between growth rate and corrosion rate, form orderly arranged array of nanotubes with uniform diameter, moderate length, and strong adhesiveness with substrates then. Although the photocatalytic activity of Rh B degradation on TNTAs prepared in glycol and DMSO is higher than those prepared in glycerol, their convenience of recycling and recovery shows the opposite. The optimality condition of anodic oxidation for TNTAs with good morphology and photocatalytic performance was present, which may have potential application in the synthesis of composite nanoarrays.

1. Introduction

Ever since carbon nanotubes were discovered by Iijima, nanomaterials with tube structure have attracted widespread attention from different research area due to its unique geometric structure and advanced physicochemical properties. As one of those nanotube materials, titanium dioxide nanotube arrays (TNTAs) have been applied to many fields, such as photocatalytic hydrogen generation, photovoltaic cells, degradation of organic contaminants, and gas sensor, because of their excellent specific surface area, high adsorption capacity, and less agglomeration [1–13]. Recently, multiple methods of preparation on TNTAs have been proposed: hydrothermal synthesis method, template method, and electrochemical anodic oxidation [14–16]. TNTAs prepared by the first two approaches are dispersed powders, which cannot adhere to the substrate firmly and are hard to be recycled. On the other hand, TNTAs prepared by electrochemical anodic oxidation adhered to the Ti substrate firmly with highly ordered array structures. Furthermore, the morphology of TNTAs can be controlled by adjusting experimental parameters.

Large-scale TNTAs composed of many single and well-arranged TiO₂ nanotubes were prepared by potentiostatic anodic oxidation of Ti foils with 0.5 wt% HF electrolyte, as Gong et al. reported at 2001 [17]. After that, the anodic oxidation method of preparing TNTAs has been studied by many researchers; it can be divided into three stages according to length of nanotube or electrolyte composition. The first TNTA generation is produced in strong acid electrolyte containing HF with pH lower than 3; its length is 500 nm below the general length [18]. The second TNTA generation is prepared at weak acid fluoride aqueous electrolyte with pH between 3 and 6; its length can reach 6.4 μm [14]. The last TNTAs generation, revolutionarily, uses organic instead of aqueous solvent as electrolyte [14, 16, 19–21]. Macak et al. prepared TNTAs by anodic oxidation and used glycol containing 0.5 wt% NH₄F as electrolyte firstly, whose length reaches 7 μm. However, the disadvantages are so fateful that they cannot be ignored: the length of tubes and specific surface area of TNTAs are distributed inhomogeneously. Besides, those tubes hardly adhere on substrates firmly [22–26]. Since then, scientists tried to design and achieve various geometrical

structures, such as stacking-type tube, chain-type tube, Bamboo-type tube, branched-type tube, and 3D complicated structure, by controlling the potential and electrolyte of anodic oxidation [27–31]. Nevertheless, to capitalize on TNTAs as photocatalysts is still a major challenge; that is, efficiencies of photoinduced processes are very low. This occurs because photocatalytic reaction rates are not fast enough to compete with the charge-recombination (electron-hole recombination). To address these problems, scientists focus on decorating TNTAs with noble metals or other nanomaterials with synergistic effect [14, 32–37]. As the starting point, the optimum condition of suitable TNTAs for decorating with materials should be investigated.

In this paper, by employing glycol, DMSO, glycerol, and $(\text{NH}_4)_2\text{SO}_4$ as main electrolytes, respectively, the effects of electrolyte and applied electric potentials on morphology of TNTAs were explored. Furthermore, photocatalytic degradation of Rhodamine B (Rh B) on TNTAs prepared from different electrolytes was compared under UV irradiation. In addition, the optimum condition TNTAs fabrication for nanoparticle deposition was discussed.

2. Experimental

2.1. Chemicals. Water used was ion-exchanged at first, distilled, and then ion-exchanged again by ultrapure water system. The purified water exhibited the ionic resistivity of $18 \text{ M}\Omega \text{ cm}$ in the water system. Other chemicals were of analytical grade and were used as received.

2.2. Preparation of TNTAs. Well-ordered TNTAs were fabricated by electrochemical anodization in a two-electrode cell which consisted of Ti foils as working electrode and a Pt foil as counter electrode. Prior to the anodization, Ti foils ($2.0 \times 5.0 \text{ cm}^2$) were ultrasonically cleaned in acetone, methanol, and ethanol for 10 min followed, respectively, by deionized water rinse.

All electrolytes were prepared as a certain proportion, stirred by magnetic stirring until complete dissolve is achieved. In this study, four typical electrolytes were employed: 0.1 M NH_4F and 0.5 M $(\text{NH}_4)_2\text{SO}_4$ mixture solution; mixture solution composed of 98% dimethyl sulfoxide (DMSO) and 2% HF in volume; NH_4F with concentration of 0.075 M dissolved in mixture solvent which is composed of H_2O (3%, v/v) and glycol (97%, v/v); NH_4F with concentration of 0.27 M dissolve in mixture solvent composed of water and glycerol with ratio of 1 : 1 by volume.

The equipment of anodic oxidation is illuminated as Figure 1; the anode and cathode electrodes were pretreated titanium foil and Pt, respectively. The distance between two electrodes was 2 cm. Applied voltage started from 0 V to a certain voltage with rate of 250 mV/s and then maintained a certain time.

The Ti foil was drawn out from electrolyte after the anodic oxidation process and then washed by deionized water in order to remove adsorbed electrolyte on the surface, followed by six times of ultrasonic cleaning every 10 seconds. Then the resulting TNTAs were dried under room temperature before next process.

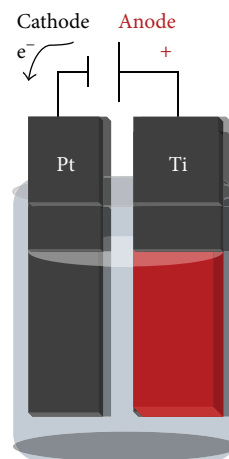


FIGURE 1: Schematic illustration of an electrochemical anodic oxidation cell.

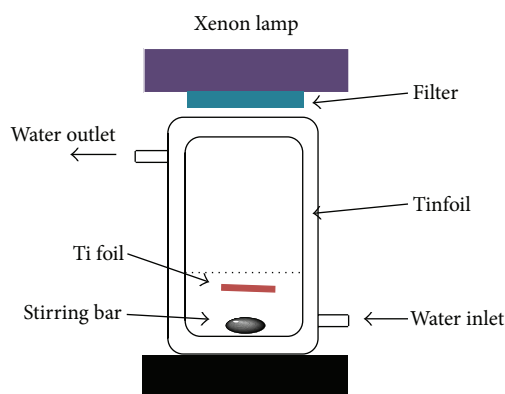


FIGURE 2: Schematic illustration of the photocatalytic reactor.

The dried TNTAs were put into muffle furnace which was firstly heated up to 200°C with $3^\circ\text{C}/\text{min}$ and kept for 30 min, then was heated up to 450°C with $2^\circ\text{C}/\text{min}$ and kept for 3 h, and was naturally cooled to room temperature at last.

2.3. Characterization. XRD patterns were acquired on a Bruker Axs D2 PHASER diffractometer with a $\text{Cu K}\alpha$ X-ray source. Scan range located from 21° to 80° . The morphology of the obtained samples was characterized by a field emission scanning electron microscope (FESEM, Hitachi S-4800). The ultraviolet-visible (UV-Vis) spectra analysis was also performed on a Shimadzu UV-3600 spectrophotometer equipped with an integrating sphere using BaSO_4 as the reference.

2.4. Photocatalytic Activity. As shown in Figure 2, the photocatalytic activities were evaluated based upon the removal of Rh B solution with an initial concentration of $5 \text{ mg}\cdot\text{L}^{-1}$ in a glass reactor with a water jacket to control the reaction temperature. For comparison, the photocatalytic activities of TNTAs obtained from different electrolytes were also studied. A 300 W xenon lamp with a 365 nm filter was employed as the simulated ultraviolet source. The distance between the xenon

lamp and the TNTAs film was 13 cm. Prior to photocatalytic degradation, the samples were immersed in 20 mL Rh B aqueous solution with magnetic stirring in the dark for 1 h to establish an adsorption-desorption equilibrium at constant room temperature. After UV irradiation started, the solution periodically taken from the reactor was analyzed with a UV-Vis spectrophotometer. The analytical wavelength selected for optical absorbance measurement was 560 nm.

Based on Lambert-Beer law, there is a proportional relationship between concentration of absorbing material and absorbance, as shown in the following equation:

$$A = \lg\left(\frac{1}{T}\right) = Kbc, \quad (1)$$

in which A indicates absorbance; T indicates transmittance; K indicates characteristic constant; b indicates thickness of absorption layer with unit of cm; c indicates concentration of absorbance with unit of $\text{mg}\cdot\text{L}^{-1}$. Therefore, change of absorbance reflects change of concentration of Rh B solution. Normalized concentration ratio of Rh B solution is close to normalized maximum absorbance ratio (A/A_0); as a result, C/C_0 can be replaced by value of A/A_0 .

3. Results and Discussion

3.1. Morphology of TNTAs. We present the SEM results of TNTAs obtained from four different electrolytes. Figures 3(a) and 3(b) show TNTAs prepared by anodic oxidation employing NH_4F and $(\text{NH}_4)_2\text{SO}_4$ mixed aqueous solution as electrolyte under constant applied voltage of 20 V for 2 h. Those nanotubes show irregular arrangement with nonuniform diameter of about 80 nm.

Figures 3(c) and 3(d) show top and cross-sectional views of TNTAs prepared by anodic oxidation with DMSO and HF mixed solution as electrolyte under constant applied voltage of 35 V for 2 h. Although the length of tubes reached $4\ \mu\text{m}$, it is clear that the tube entrance collapses seriously, coupled with broken surface which may be caused by relatively high voltage.

Figures 3(e)–3(h) show top, bottom, cross-sectional, and truncation views of TNTAs prepared by anodic oxidation employing NH_4F and glycol mixed aqueous solution as electrolyte under constant applied voltage of 20 V for 2 h. Nanotubes obtained under this condition are more complicated. Their surface shows weed-like features and bottom shows typical hexagon, while the walls are so smooth. The cross-link between those walls obviously decreased when compared to other TNTAs. Those nanotubes easily fall off from Ti substrate although the length of them reaches about $33\ \mu\text{m}$. Nanotube entrance collapse and broken surface may be attributed to the inhomogeneity of the tube structure. Fast growth rate along the tube leads to thinness of tube walls. As a result, those tubes cannot sustain the weight and thermal stress of themselves during the drying process.

Figures 3(i) and 3(j) show top and cross-sectional views of TNTAs prepared by anodic oxidation by employing NH_4F and glycerol mixed aqueous solution as electrolyte under applied constant voltage of 20 V for 2 h. The diameter of these tubes is uniform with 100 nm for inner and 117 nm for

outer. The length is about $1\ \mu\text{m}$. Ripples on the tube walls can be seen, which indicates that the participation of water into electrolyte is necessary for oxidation corrosion of Ti foils. The corrosion rate of Ti foils and growth rate of TiO_2 are affected by the content of water. The formation of nanotubes with corrugated tube wall needs relative high content of water. These tubes adhere on the substrate firmly, which performs good stability of geometric structure and conveniences of recycling.

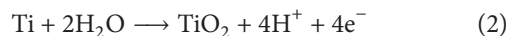
Then it can be concluded that NH_4F and glycerol mixed aqueous solution is the preferential electrolyte among those four kinds of electrolytes in this study. Therefore, based on this electrolyte system, other operating parameters including applied voltage and duration of anodic oxidation have been studied.

Figure 4 shows top view of TNTAs prepared at condition of (a) (20 V, 2 h), (b) (20 V, 6 h), (c) (25 V, 2 h), (d) (25 V, 6 h), (e) (30 V, 2 h), and (f) (30 V, 6 h), respectively. With the increase of applied voltage from 20 V, the diameter of nanotubes remains unaffected; however, the tube entrance becomes uniform and arrangement of nanotubes decreases seriously. Also the shape of tubes and thinness of tube walls tend to be inhomogeneous with increase of voltage.

As is seen in Figure 4, with the duration of anodic oxidation from 2 h to 6 h, tubular structure is severely damaged. The possible explanation might be that two dynamic processes contributed to the growth of tube on radial direction: anodic oxidation of Ti substrate to form fresh TNTAs and dissolution of tubes on the top part. There is an optimum duration of oxidation which is defined to be the equilibrium of those two dynamic processes. Longer time may unbalance the equilibrium, which forces the growth of tubes to be affected by diffusion, gravity, viscosity, and so forth.

3.2. Growth Mechanism of TNTAs. The key process of electrochemical oxidation can be explained as follows: firstly, oxides were formed on metal surface under the influence of interaction of oxygen ions or hydroxide ions. After that, those anions cross through oxidation layer and migrate to metal/oxide interface to react with metal. Secondly, under the effects of external electric field, tetravalent titanium ion (Ti^{4+}) migrates from metal/oxide surface to oxide/electrolyte surface. Electric field assisted dissolve will be the third step: under effect of external electric field, Ti–O bond undergoes polarization and is weakened, accelerating the dissolution of the metal cations. After Ti^{4+} dissolved into electrolyte, free oxygen anions migrate to metal/oxide intersurface and then interact with metal as mentioned at the first step. Lastly, chemical dissolve of metal or oxide occurs in acidic electrolyte. Chemical dissolve of TiO_2 in fluoride ion electrolyte plays a crucial role on formation process of nanotubes. Schematic diagram of ions migration was shown in Figure 5.

At the beginning of anodic oxidation, the initial oxidation layer was formed by interaction of Ti^{4+} ions on surface and O^{2-} ions in electrolyte, which can also be seen as distributed homogeneously on the surface. The anodic oxidation of metal to form hydrogen ions and electrons is shown in



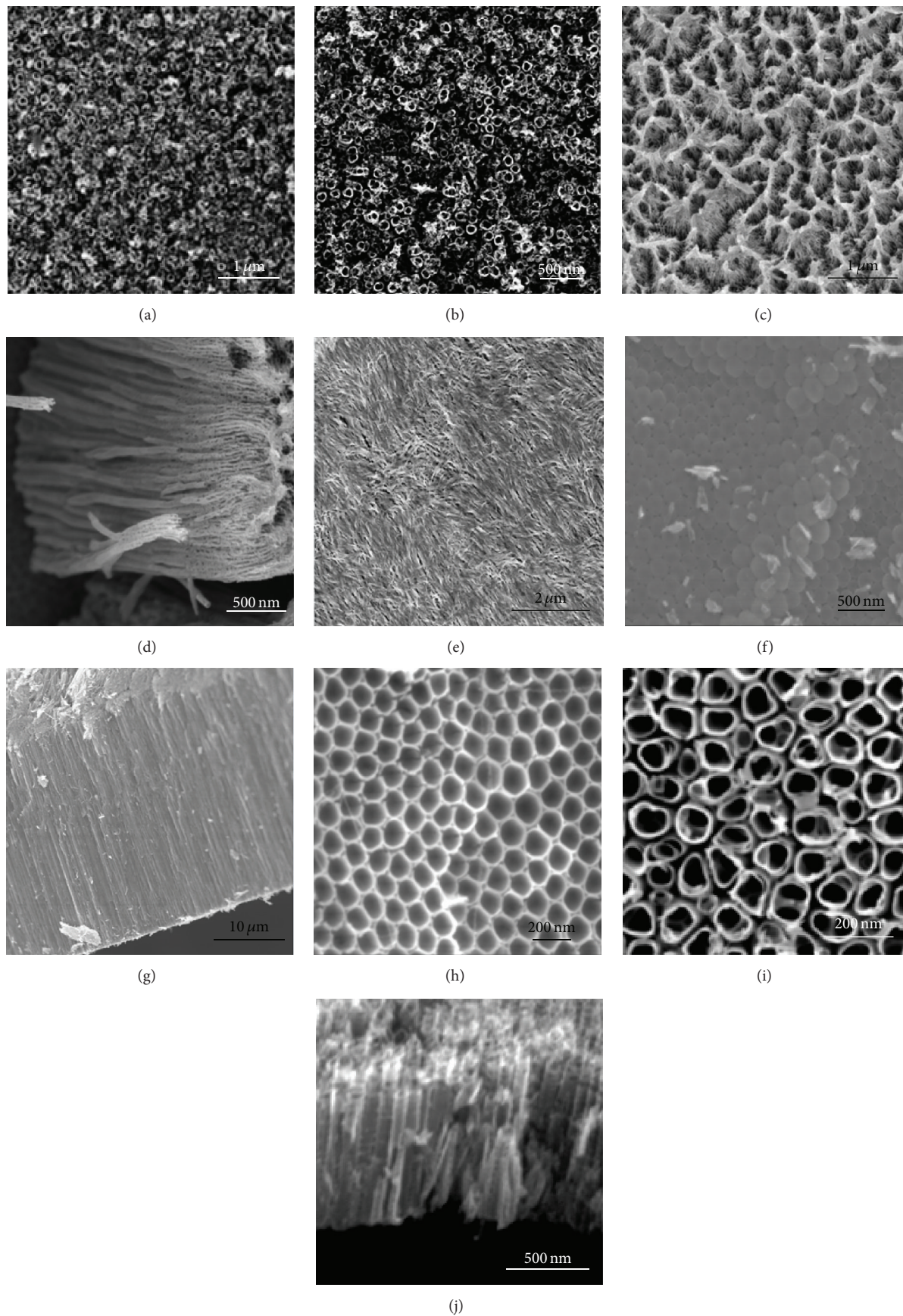


FIGURE 3: FE-SEM images of TNTAs fabricated by different solutions.

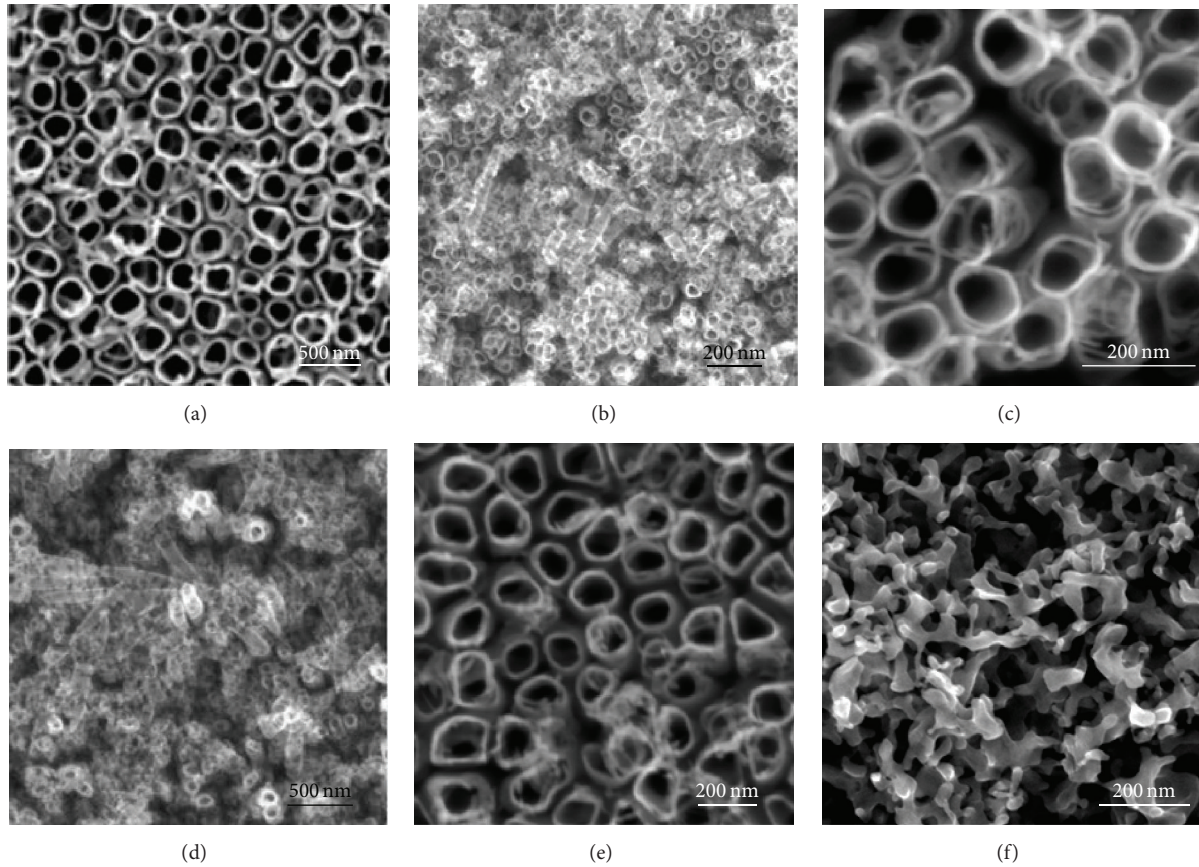


FIGURE 4: FE-SEM images of TNTAs fabricated by glycerol based solutions under different voltage and anodic oxidation time.

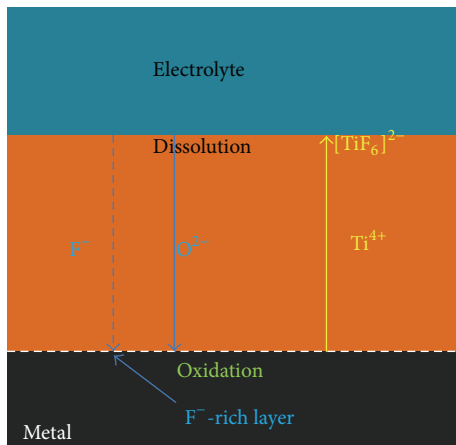
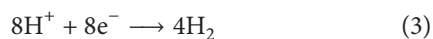
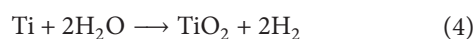


FIGURE 5: Schematic drawing showing field-aided transport of mobile ions through the oxide layers in the presence of fluoride ions.

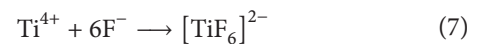
Hydrogen generated at cathode is as follows:



The total oxidation process can be given by



Fluorine ions may attack water molecule and oxidation layer; in other words, ions migrating on anode layer under external electric field could react with Ti^{4+} anions:



As shown in Figure 6(a), a thin layer formed on the titanium surface with start of anodic oxidation. Since partial dissolve of oxide may make the barrier layer at the bottom of concave thin, as can be seen in Figure 6(b), the electric field intensity at those remaining barrier layers increased resulting in further growth of pore. As shown in Figure 6(c), pores of tube appear relatively narrow since the field associated dissolve has no influence on formation of pores. However, the electric field distribution at bottom surface of the pore may broaden diameter of tubes as well as deepen cracks, which causes pores of nanotubes formed like a scallop shape. Since the bond energy of Ti–O is rather high, for TiO_2 , it can be predicted reasonably that pores only can be formed on those thin walls, which can be contributed by relatively low ionic mobility and rather high chemical solubility of oxide in electrolyte. The electric field intensity at protruding metal area will increase with the growth of pores, which may enhance

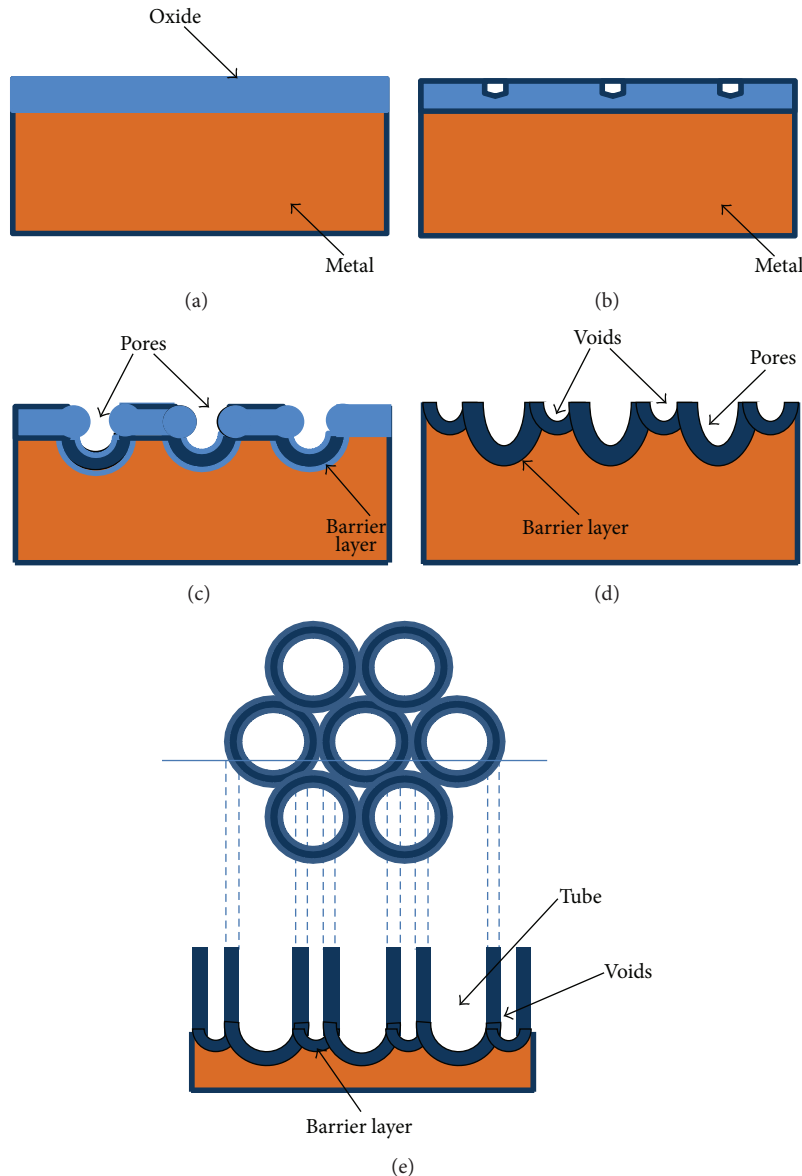


FIGURE 6: Schematic diagram of nanotube evolution at constant anodization voltage: (a) oxide layer formation, (b) pit formation on the oxide layer, (c) growth of the pit into scallop shaped pores, (d) the metallic region between the pores undergoing oxidation and field assisted dissolution, and (e) fully developed nanotubes with a corresponding top view.

the field associated growth of oxide and dissolution of oxide. Meanwhile, uniformly distributed pores and voids between pores formed in Figure 6(d). Subsequently, voids and pores grow together under equilibrium condition. The length will increase until the balance is achieved between electrochemical corrosion rate and chemical dissolution rate on the top surface of nanotubes. Thereafter, the length of nanotubes is finally achieved by given anodic oxidation time, concentration of electrolyte, and anodic oxidation voltage.

3.3. XRD Characterization. As seen in Figure 7, XRD characterization of TNTAs obtained in four different electrolytes has been presented. Five diffraction peaks at 25.2° , 37.8° , 48.1° , 53.9° , and 55.1° indicate crystal phase of anatase at

(101), (004), (200), (105), and (211), respectively, according to JCPDS number 21-1272. It is obvious that anatase TNTAs can be obtained by annealing at 450°C . Peak intensities of crystal plane (101) for TNTAs prepared at glycerol aqueous electrolyte and NH_4F and $(\text{NH}_4)_2\text{SO}_4$ mixed aqueous electrolyte appear lower than those prepared at glycol electrolyte and DMSO electrolyte. This can be explained by the fact that ratio of TiO_2 is deeply influenced by length of nanotube, which is in accordance with SEM results. Besides, XRD characterization of Ti substrate and TNTAs fabricated in NH_4F and glycerol mixed aqueous solution were presented, respectively, before and after TNTAs are annealed (Figure 8). It can be seen that after anodization process TNTAs are amorphous and upon annealing they become anatase.

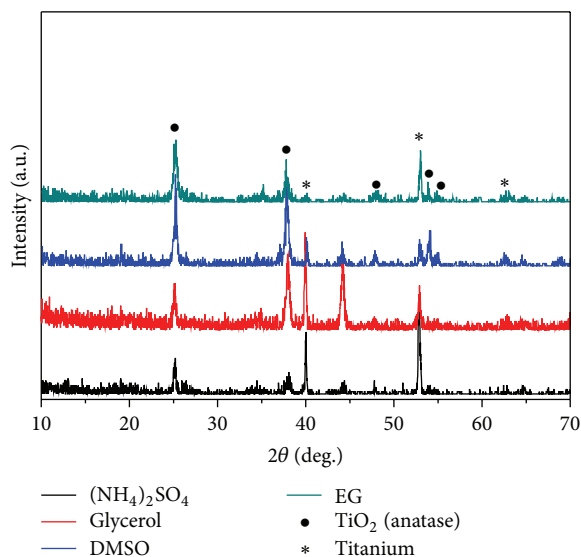


FIGURE 7: XRD patterns of TNTAs fabricated by different solutions.

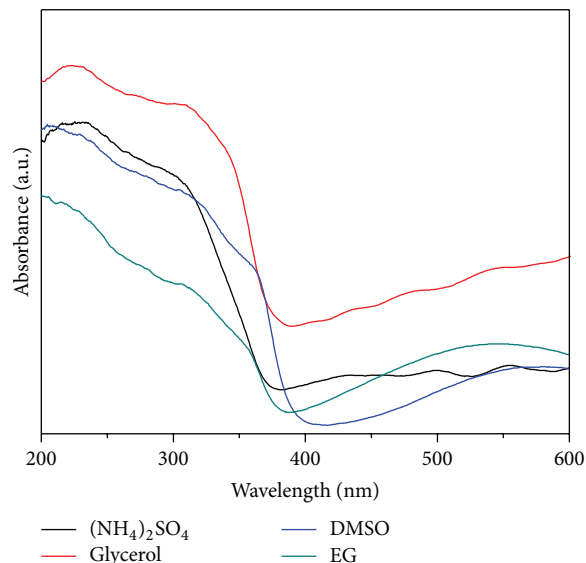
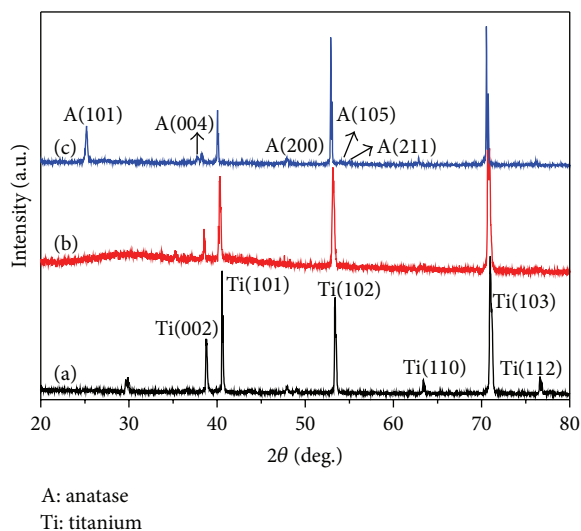


FIGURE 9: UV-Vis spectra TNTAs made in different solutions.

FIGURE 8: XRD patterns of TNTAs fabricated in NH_4F and glycerol mixed aqueous solution ((a) Ti substrate; (b) before annealing; (c) after annealing).

3.4. UV-Vis Diffuse Reflection Spectroscopy. The optical properties of TNTAs prepared at different electrolytes were studied by UV-Vis diffuse reflection spectroscopy, as shown in Figure 9. Light response range of all TNTAs reported here is localized in ultraviolet range. However, TNTAs prepared by glycerol electrolyte, in spite of its disadvantage at length of nanotube, show highest intensity of light adsorption at tail. This may benefit from the uniformity of nanotube arrangement and less collapse on nanotube entrance. For those TNTAs obtained by other electrolytes, although length of nanotube may have its edge, collapse on nanotube entrance or structures with weed-like features and disordered orientation result in the fact that the obstacle of incident light could not pass into passageway of nanotubes, eventually.

3.5. Photocatalytic Activity on Degradation of Rh B. TNTAs are one of the most active materials for degradation of contaminants especially for organic pollutants. This may be contributed by the proximity between conduction band edge of TNTAs and redox potentials of the surroundings such as water. Rh B, as one of the most water pollutants, is stable and carcinogenic [38]. The photocatalytic activities of TNTAs fabricated in four different electrolytes were investigated by degrading Rh B.

The variation of C/C_0 with illumination time is shown in Figure 10(a), in which C_0 indicates the initial concentration after the adsorption equilibrium is established, while C indicates concentration of reaction solution extracted out every 30 minutes. It can be seen from blank curve of Figure 10(a) that the Rh B molecule is extremely stable under UV irradiation without the presence of catalysts. Also, after irradiation of 210 minutes by UV, Rh B shows no evidence of decomposition, which indicates impossibility of self-degradation. The degradation efficiencies of TNTAs prepared in electrolytes of glycol, DMSO, glycerol, and $(\text{NH}_4)_2\text{SO}_4$ are 75.14%, 49.82%, 34.26%, and 25.82%, respectively. The kinetics equation of catalytic reaction on these TNTAs photocatalysts has been studied by using first-order kinetics equation $\ln(C/C_0) = -kt$, in which k indicates the first kinetics equation constant. As shown in Figure 10(b), the catalytic rate constant in electrolyte of glycol, DMSO, glycerol, and $(\text{NH}_4)_2\text{SO}_4$ is 6.45×10^{-3} , 3.37×10^{-3} , 2.03×10^{-3} , and $1.42 \times 10^{-3} \text{ min}^{-1}$, respectively. The order of catalytic rate constant is in accordance with the order of the length of nanotubes. For photocatalytic degradation on TiO_2 nanotube arrays, it is common sense that the amount of TiO_2 crystals will increase with increase of length of nanotube, which would exhibit better photocatalytic activity.

In order to further more effective composites by loading nanoparticles, however, those nanotubes prepared in electrolyte of glycol, DMSO shows their disadvantage of poor

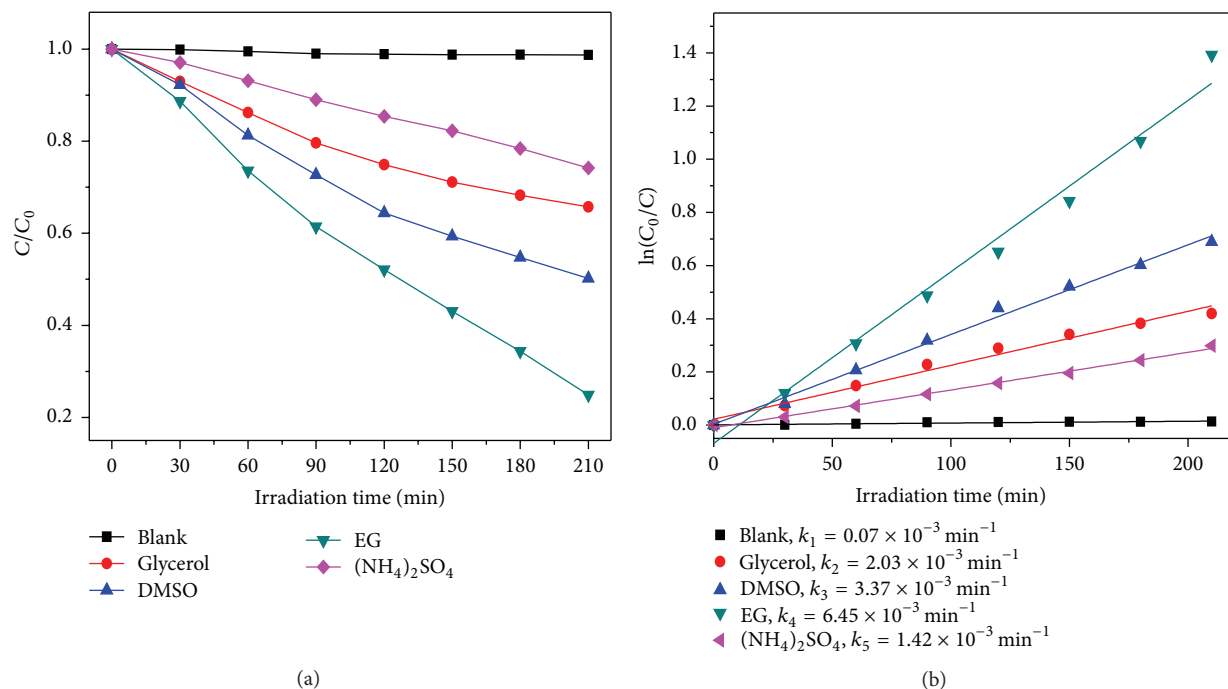


FIGURE 10: (a) Photocatalytic degradation of Rh B under UV light irradiation on various catalysts and (b) first-order kinetics data for the photodegradation of Rh B on various catalysts and the inset is the value of the rate constant k .

recycling efficiency. Firstly, the entrance of these tubes tends to collapse and snarls, which brings a great difficulty to decorate other nanoparticles on more widespread surface of TNTAs. Secondly, the overlong nanotubes increased the burden of Ti substrates, which makes nanotubes vulnerable and easier to fall off from substrates, when compared with other nanotubes having moderate length. And this will go against recycling and recovery of effective part of photocatalyst. To make composites by depositing nanoparticles on TNTAs, TNTAs prepared in glycerol under voltage of 20 V for 2 h are the best loading substrate, contributing by their uniform diameter, moderate length, and close adhesiveness with Ti foils.

4. Conclusions

The formation process of TNTAs strongly depends on the electrolytes. TNTAs formed in the electrolytes of glycol and DMSO grow along radial direction with flimsy tube wall and weak adhesion on Ti substrate. These TNTAs are not appropriate to assemble composite photocatalyst with other nanomaterials, although they show, respectively, higher catalytic activities. Those made in glycerol, however, easily achieve balance between growth rate and corrosion rate and form orderly arranged array of nanotubes with homogenous diameter, moderate length, and strong adhesiveness with substrates.

In addition, applied voltage and anodic oxidation duration crucially affect nanotube formation. Generally, longer time and higher voltage of oxidation will enhance length of nanotubes. However, the oxidation rate of Ti substrate and

dissolve rate of nanotubes will be well balanced at condition of 20 V for 2 h. Consequently, TNTAs prepared in this condition will be the most appropriate loading substrates to further assemble functional composite nanomaterials.

Conflict of Interests

The authors declare that there is no conflict of interests regarding the publication of this paper.

Acknowledgments

This work is financially supported by the National Natural Science Foundation of China (NSFC Grant no. 21503146), International S&T Cooperation Program of China (no. 2013-DFG52490), The Training Program for Changjiang Scholars and Innovative Research Team in University ([2013]373), The Innovative Research Team of Tianjin Municipal Education Commission (TD125004), Scientific Research Foundation for the Introduction of Talent of Tianjin University of Science and Technology (no. 118510240), and Research Fund for the Doctoral Program of Higher Education of China (no. 20121208120001).

References

- [1] M. Ye, D. Zheng, M. Lv, C. Chen, C. Lin, and Z. Lin, "Hierarchically structured nanotubes for highly efficient dye-sensitized solar cells," *Advanced Materials*, vol. 25, no. 22, pp. 3039–3044, 2013.
- [2] S. Banerjee, S. K. Mohapatra, M. Misra, and I. B. Mishra, "The detection of improvised nonmilitary peroxide based explosives using a titania nanotube array sensor," *Nanotechnology*, vol. 20, no. 7, Article ID 075502, 2009.

- [3] Y.-Y. Song and P. Schmuki, "Modulated TiO₂ nanotube stacks and their use in interference sensors," *Electrochemistry Communications*, vol. 12, no. 4, pp. 579–582, 2010.
- [4] Y. Hou, X. Li, Q. Zhao, G. Chen, and C. L. Raston, "Role of hydroxyl radicals and mechanism of *Escherichia coli* inactivation on Ag/AgBr/TiO₂ nanotube array electrode under visible light irradiation," *Environmental Science and Technology*, vol. 46, no. 7, pp. 4042–4050, 2012.
- [5] X. Wang, Y. Zhang, I. Baturin, and T. Liang, "Blocking effect of crystal-glass interface in lanthanum doped barium strontium titanate glass-ceramics," *Materials Research Bulletin*, vol. 48, no. 10, pp. 3817–3821, 2013.
- [6] Q. Wang, J. Li, Y. Bai et al., "Photodegradation of textile dye Rhodamine B over a novel biopolymer-metal complex wool-Pd/CdS photocatalysts under visible light irradiation," *Journal of Photochemistry and Photobiology B: Biology*, vol. 126, pp. 47–54, 2013.
- [7] W. Wilson, A. Manivannan, and V. R. Subramanian, "Heterogeneous photocatalytic degradation of recalcitrant pollutants over CdS—TiO₂ nanotubes: boosting effect of TiO₂ nanoparticles at nanotube—CdS interface," *Applied Catalysis A: General*, vol. 441–442, pp. 1–9, 2012.
- [8] Q. Wang, X. Yang, D. Liu, and J. Zhao, "Fabrication, characterization and photocatalytic properties of Ag nanoparticles modified TiO₂NTs," *Electrochimica Acta*, vol. 83, p. 140, 2012.
- [9] C. Chen, W. Ma, and J. Zhao, "Semiconductor-mediated photodegradation of pollutants under visible-light irradiation," *Chemical Society Reviews*, vol. 39, no. 11, pp. 4206–4219, 2010.
- [10] X. Cheng, G. Pan, X. Yu, and T. Zheng, "Preparation of CdS NCs decorated TiO₂ nano-tubes arrays photoelectrode and its enhanced photoelectrocatalytic performance and mechanism," *Electrochimica Acta*, vol. 105, pp. 535–541, 2013.
- [11] Y. Lai, J. Gong, and C. Lin, "Self-organized TiO₂ nanotube arrays with uniform platinum nanoparticles for highly efficient water splitting," *International Journal of Hydrogen Energy*, vol. 37, no. 8, pp. 6438–6446, 2012.
- [12] Y. Yu, J. Ren, and M. Meng, "Photocatalytic hydrogen evolution on graphene quantum dots anchored TiO₂ nanotubes-array," *International Journal of Hydrogen Energy*, vol. 38, no. 28, pp. 12266–12272, 2013.
- [13] J. Ran, J. Zhang, J. Yu, M. Jaroniec, and S. Z. Qiao, "Earth-abundant cocatalysts for semiconductor-based photocatalytic water splitting," *Chemical Society Reviews*, vol. 43, no. 22, pp. 7787–7812, 2014.
- [14] P. Roy, S. Berger, and P. Schmuki, "TiO₂ nanotubes: synthesis and applications," *Angewandte Chemie—International Edition*, vol. 50, no. 13, pp. 2904–2939, 2011.
- [15] M. Ni, M. K. H. Leung, D. Y. C. Leung, and K. Sumathy, "A review and recent developments in photocatalytic water-splitting using TiO₂ for hydrogen production," *Renewable and Sustainable Energy Reviews*, vol. 11, no. 3, pp. 401–425, 2007.
- [16] X. Zhao, K. J. Aoki, J. Chen, and T. Nishiumi, "Examination of the Gouy-Chapman theory for double layer capacitance in deionized latex suspensions," *RSC Advances*, vol. 4, no. 108, pp. 63171–63181, 2014.
- [17] D. Gong, C. A. Grimes, O. K. Varghese et al., "Titanium oxide nanotube arrays prepared by anodic oxidation," *Journal of Materials Research*, vol. 16, no. 12, pp. 3331–3334, 2001.
- [18] S. Bauer, S. Kleber, and P. Schmuki, "TiO₂ nanotubes: tailoring the geometry in H₃PO₄/HF electrolytes," *Electrochemistry Communications*, vol. 8, no. 8, pp. 1321–1325, 2006.
- [19] Y. Zhu, Z. Chen, T. Gao et al., "Construction of hybrid Z-scheme Pt/CdS-TNTAs with enhanced visible-light photocatalytic performance," *Applied Catalysis B: Environmental*, vol. 163, pp. 16–22, 2015.
- [20] K. J. Aoki, X. Zhao, J. Chen, and T. Nishiumi, "Voltammetry in low concentration of electrolyte supported by ionic latex suspensions," *Journal of Electroanalytical Chemistry*, vol. 697, pp. 5–9, 2013.
- [21] S. P. Albu, D. Kim, and P. Schmuki, "Growth of aligned TiO₂ bamboo-type nanotubes and highly ordered nanolace," *Angewandte Chemie—International Edition*, vol. 47, no. 10, pp. 1916–1919, 2008.
- [22] J. M. Macak, H. Tsuchiya, A. Ghicov et al., "TiO₂ nanotubes: self-organized electrochemical formation, properties and applications," *Current Opinion in Solid State and Materials Science*, vol. 11, no. 1–2, pp. 3–18, 2007.
- [23] J. M. Macak, H. Hildebrand, U. Marten-Jahns, and P. Schmuki, "Mechanistic aspects and growth of large diameter self-organized TiO₂ nanotubes," *Journal of Electroanalytical Chemistry*, vol. 621, no. 2, pp. 254–266, 2008.
- [24] S. P. Albu, A. Ghicov, and P. Schmuki, "Erratum efficient solar energy conversion of TiO₂ nanotubes produced by rapid breakdown anodization—a comparison," *Rapid Research Letters (RRL)*, vol. 3, p. 64, 2009.
- [25] Y.-Y. Song, R. Lynch, D. Kim, P. Roy, and P. Schmuki, "TiO₂ nanotubes: efficient suppression of top etching during anodic growth: key to improved high aspect ratio geometries," *Electrochemical and Solid-State Letters*, vol. 12, no. 7, pp. C17–C20, 2009.
- [26] S. P. Albu and P. Schmuki, "Highly defined and ordered top-openings in TiO₂ nanotube arrays," *Physica Status Solidi (RRL)—Rapid Research Letters*, vol. 4, no. 7, pp. 151–153, 2010.
- [27] J. Liao, S. Lin, L. Zhang, N. Pan, X. Cao, and J. Li, "Photocatalytic degradation of methyl orange using a TiO₂/Ti mesh electrode with 3D nanotube arrays," *ACS Applied Materials and Interfaces*, vol. 4, no. 1, pp. 171–177, 2012.
- [28] X. Luan, D. Guan, and Y. Wang, "Facile synthesis and morphology control of bamboo-type TiO₂ nanotube arrays for high-efficiency dye-sensitized solar cells," *The Journal of Physical Chemistry C*, vol. 116, no. 27, pp. 14257–14263, 2012.
- [29] X. Zhao, K. J. Aoki, J. Chen, and T. Nishiumi, "Which controls conductivity of sulfonic latex suspension, hydrogen ion or latex core?" *International Journal of Electrochemical Science*, vol. 9, no. 5, pp. 2649–2661, 2014.
- [30] X. Zhang, F. Han, B. Shi, S. Farsinezhad, G. P. Dechaine, and K. Shankar, "Photocatalytic conversion of diluted CO₂ into light hydrocarbons using periodically modulated multiwalled nanotube arrays," *Angewandte Chemie—International Edition*, vol. 51, no. 51, pp. 12732–12735, 2012.
- [31] H. Li, J.-W. Cheng, S. Shu et al., "Selective removal of the outer shells of anodic TiO₂ nanotubes," *Small*, vol. 9, no. 1, pp. 37–44, 2013.
- [32] H. Cao, Z. Wang, G. Hou, and G. Zheng, "TiO₂ nanotube-supported amorphous Ni-B electrode for electrocatalytic oxidation of methanol," *Surface and Coatings Technology*, vol. 205, no. 3, pp. 885–889, 2010.
- [33] Q. Kang, Q. Z. Lu, S. H. Liu et al., "A ternary hybrid CdS/Pt-TiO₂ nanotube structure for photoelectrocatalytic bactericidal effects on *Escherichia coli*," *Biomaterials*, vol. 31, no. 12, pp. 3317–3326, 2010.

- [34] Q. Z. Xu, X. Y. Wang, X. L. Dong, C. Ma, X. F. Zhang, and H. C. Ma, "Improved visible light photocatalytic activity for TiO_2 nanomaterials by codoping with zinc and sulfur," *Journal of Nanomaterials*, vol. 2015, Article ID 157383, 8 pages, 2015.
- [35] W. Guan, F. Y. Ji, Z. G. Xie, R. A. Li, and N. Mei, "Preparation and photocatalytic performance of nano- TiO_2 codoped with iron III and lanthanum III," *Journal of Nanomaterials*, vol. 2015, Article ID 869821, 13 pages, 2015.
- [36] M. Fujita, N. Idota, K. Matsukawa, and Y. Sugahara, "Preparation of oleyl phosphate-modified TiO_2 /poly(methyl methacrylate) hybrid thin films for investigation of their optical properties," *Journal of Nanomaterials*, vol. 2015, Article ID 297197, 7 pages, 2015.
- [37] D. Yu, B. Bo, and Y. He, "Fabrication of TiO_2 @yeast-carbon hybrid composites with the raspberry-like structure and their synergistic adsorption-photocatalysis performance," *Journal of Nanomaterials*, vol. 2013, Article ID 851417, 8 pages, 2013.
- [38] Q. Wang, J. Li, Y. Bai et al., "Photodegradation of textile dye Rhodamine B over a novel biopolymer-metal complex wool-Pd/CdS photocatalysts under visible light irradiation," *Journal of Photochemistry and Photobiology B: Biology*, vol. 126, pp. 47–54, 2013.